博士論文

INITIATION MECHANISM OF HEAVY RAINFALL-INDUCED SHALLOW LANDSLIDES ON STEEP SLOPES WITH IMPERMEABLE BEDROCK

YANG HUFENG

平成23年度入学

島根大学大学院総合理工学研究科博士後期課程

マテリアル創成工学専攻

主指導教員：汪 発武

平成 27 年 7 月 21 日受理

ABSTRACT

Global warming increases precipitation in wet climate regions, especially in East Asia. Heavy rainfall frequently occurs in Japan, especially during the summer monsoon season, causing geoenvironmental disasters such as shallow landslides and debris flows. This research aims to understand the initiation mechanism of heavy rainfall-induced shallow landslides on steep slopes with impermeable bedrock and propose a method for time prediction.

Three events of heavy rainfall-induced shallow landslides at Aso caldera, Izu Oshima Island and Hiroshima in Japan were selected as the study sites for this research. These study sites present two types of widespread landslide-forming materials in Japan. One type material is pyroclastic-fall deposits. The other type material is the residual soil from weathered granite. These shallow landslides were triggered on steep slopes with impermeable bedrock by heavy rainfall related to typhoons or low-pressure troughs. This research is specifically focused on examining the soil behavior in response to pore-water pressure increase in two kinds of landslide-forming materials by conducting pore-water pressure controlled triaxial tests. The pore-water pressure controlled triaxial tests simulate the behavior of soils under pore-water pressure increase in slope due to rainfall infiltration during heavy rainfall. Meanwhile, the results describe the initiation mechanism of these two kinds of heavy rainfall induced-shallow landslides on the steep slopes with impermeable bedrock. For the pyroclastic-fall deposits, the axial strain increased rapidly when the pore-water pressure reached to a relatively high value. Then, excess pore-water pressure increased rapidly with the increase in axial strain. This resulted in the obvious decrease in effective stress of the soil. Finally, static liquefaction occurred, leading to the generation of shallow landslides on the steep slopes. For the residual soil from weathered granite, the increase of axial strain started at low pore-water pressure. With the increase in pore-water pressure, the axial strain increase

gradually. However, no pore-water pressure buildup was recorded in the residual soil from weathered granite in contrast to the pyroclastic-fall deposits. The soil behavior with the increase in pore-water pressure provides the possibility of failure prediction through the monitoring or simulation of groundwater level in slopes during heavy rainfall.

A method for time prediction of rainfall-induced shallow landslides on steep slopes with impermeable bedrock is developed based on the study on the initiation mechanism of heavy rainfall-induced shallow landslides. Based on field investigations on slopes and laboratory experiments on soil samples, a database can be built for the target area. The relationship between slope stability and pore-water pressure can be obtained through slope stability analysis based on the slope features and soil properties. The simulation tests can also be used to understand how subsurface-water dynamics influence landslide initiation. Pore-water pressure controlled triaxial test is a recommended method for this simulation test. Because the pore-water pressure controlled triaxial test can simulate field condition to determine the soil behavior in response to the increase in pore-water pressure, the critical pore-water pressure can be obtained based on the analysis of the effect of pore-water pressure on slope stability. During heavy rainfall, realtime rainfall data is inputted into the groundwater model to simulate the generation of groundwater level in the soil layer. For a special area, piezometers can be installed in the soil layer to monitor the pore-water pressure during heavy rainfall. If the pore-water pressure, which is obtained by groundwater simulation or field monitoring, is higher than the critical pore-water pressure, the slope will be in critical state and shallow landslide could probably occur. Through the method application on the rainfall-induced shallow landslides in northeastern Shikoku, Japan, in 2004, it can be observed that this method is feasible for time prediction of rainfall-induced shallow landslides during heavy rainfall.

ACKNOWLEDGEMENTS

The thesis entitled “Initiation mechanism of heavy rainfall-induced shallow landslides on steep slopes with impermeable bedrock” is written in order to fulfill the partial requirement for doctoral degree in Department of Geoscience, Interdisciplinary Graduate School of Science and Engineering, Shimane University, Japan.

I would like to thank the China Scholarship Council (CSC) of the Ministry of Education of the P. R. China for awarding me the scholarship to study in Japan. The investigation works in this research were supported by JSPS KANKENI Grant Number A-2424106 and a fund for exploratory research from Shimane University. These financial supports are gratefully acknowledged.

I wish to express my deepest appreciation to my supervisor, Professor Fawu Wang, for his continued guidance and encouragement throughout my studies in Japan. His ideas, suggestions and supports during field and laboratory investigations were invaluable.

I would like to thank all the professors and staff of the Department of Geoscience, Shimane University, for their academic support. I am very grateful to Dr. Barry Roser for his help in checking the manuscripts and Mr. Nakamura for his technical support in laboratory.

I would like to express my appreciation to Professor Wenxing Jian (my Master degree supervisor), Professor Kunlong Yin, Professor Yiping Wu and Ms. Shuangmei Mao who fully supported me to study oversea.

I would like to thank all members of my dissertation committee for their time on the review and evaluation during the application.

I sincerely thank to all my colleagues in Professor Wang’s laboratory. Especially, I would like to thank Messrs. Hatanaka and Mitani who were my tutors at the beginning time of my new life in Japan. Thank Messrs. Sonoyama, Honda and Kuwada for their

time and organization during laboratory events, conference participation and field investigation. Thank Dr. Wu, Mr. Austin, and Miss. Chien for their comments and suggestion on my research during the discussion in seminar. I really appreciate Dr. Fikri Faris and Mr. Đỗ Ngọc Hà for their moral and academic support.

Also I would like to thank my dear friends, who I met in Japan, especially Mr. Nuwan. We have shared so many memorable time and stories.

My special thanks go to my parents, brother and sister in law, and sister who always give me full support to follow my heart.

This thesis is dedicated to my beloved wife, Tianlin Guo, for her endless love, encouragement and patience during my study in Japan.

TABLE OF CONTENTS

LIST OF TABLES

LIST OF FIGURES

LIST OF NOTATIONS

The following symbols have been used in the thesis. A dash indicates no unit or dimensionless.

Symbol	Description	Unit
B	Skempton's pore pressure coefficient, $\Delta u/\Delta\sigma_3$	—
c	Apparent cohesion	kPa
c'	Effective cohesion	kPa
C_c	Coefficient of curvature	—
CSL	Critical state line	—
CU	Consolidated-undrained triaxial compression test	—
C_u	Coefficient of uniformity	—
D	Diameter of pipe	m
D_{10}	Effective grain size	mm
D_{50}	Mean grain size	mm
e	Void ratio	—
F_S	Factor of safety	—
FSP	Field stress path	—
g	Gravitational acceleration	m/s^2
G_S	Specific gravity	—
h	Height of groundwater level	m
H	Thickness of soil layer	m
k	Hydraulic conductivity	m/s
L	Depth of borehole	m
L	Horizontal distance of slope	m
LL	Liquid limit	%
n	Porosity	—
n	Spatial identifier	—

PPC	Pore-water pressure controlled triaxial test	—
PI	Plasticity index	%
PL	Plastic limit	%
R	Net rate of recharge of infiltrated rainfall	mm/s
S	Degree of saturation	%
S	Shear force	N
S	Specific yield	—
t	Time identifier	sec
u, u_w	Pore-water pressure	kPa
u_a	Pore-air pressure	kPa
u_c	Critical pore-water pressure	kPa
USCS	Unified soil classification system	—
w	Water content	%
α	Slope angle	°
γ	Unit weight	kN/m^3
γ'	Effective unit weight	kN/m^3
γ_d	Dry unit weight	kN/m^3
γ_{sat}	Saturated unit weight	kN/m^3
γ_w	Unit weight of water	kN/m^3
Δt	Time interval	sec
ε	Axial strain	%
η	Kinematic viscosity of water	m^2/s
θ	Volumetric water content	%
θ_r	Residual water content	%
θ_s	Saturated water content	%
μ	Coefficient related to susceptibility	—
ρ	Bulk density	kg/m^3
ρ_d	Dry density	kg/m^3

σ	Total normal stress	kPa
σ'	Effective normal stress	kPa
σ_1	Major principal stress	kPa
σ_1'	Effective major principal stress	kPa
σ_3	Minor principal stress	kPa
σ_3'	Effective minor principal stress	kPa
τ	Shear stress	kPa
τ_f	Shear resistance	kPa
ϕ'	Effective frictional angle	°
ϕ^b	An angle indicating the rate of increase in shear strength with respect to changes in u_a-u_w	°
χ	Effective stress parameter	—

CHAPTER 1

INTRODUCTION

1.1 Rainfall-induced shallow landslides in Japan

Global warming increases precipitation in wet climate regions, especially in East Asia (IPCC, 2013). Shallow landslides triggered by heavy rainfall in highly developed mountainous terrains result in tremendous losses (Ho et al., 2012). Generally, the damages directly caused by shallow landslides are rarely reported. The significance of shallow landslides is emphasized because the sliding mass easily transforms into rapidly debris flows during heavy rainfall, especially in the mountain areas with steep terrain. The high-speed debris flows often cause considerable damage to the residence at the toe of hillside areas (Saito et al., 2010). The losses continue to grow as human development expands into unstable hillside areas. The one of the nations most severely affected by landsides is Japan, which suffers estimated total (direct plus indirect) landslide losses of 4 billion USD annually (Turner and Schuster, 1996).

Japan is located at the East Asian monsoon region. Heavy rainfall frequently occurs in Japan, especially during the summer monsoon season (Matsumoto, 1989, 1993; Matsumoto and Takahashi, 1999; Oguchi et al., 2001). Satio et al. (2010) used Radar-Raingauge Analyzed Precipitation data to illustrate the distribution of mean annual precipitation (MAP) in Japan during 2006-2008 (Fig. 1.1). They also indicated that the MAP in 2006-2008 was closed to the average condition of the past 20 years. The distribution of MAP shows that the southern part of Honshu, Shikoku, and Kyushu

frequently suffer heavy rainfall during summer monsoon season. Matsumoto (1993) found that most of the Japanese Islands had experienced a daily precipitation of more than 300 mm at least once science the beginning of modern metrological observations. In addition, Japan is characterized by its high topographic relief and complex geological conditions (Katsube and Oguchi, 1999; Kawabata et al., 2001; Oguchi et al., 2001; Saito et al., 2009). The combination of heavy rainfall and steep topography in Japan results in widespread landslides and debris flows (Oguchi et al., 2001; Japan Sabo Association, 2001). Compering with distribution of 1174 rainfall-induced shallow landslide events the occurred during 2006-2008 (Fig. 1.2), it is observed that the occurrence of shallow landslides corresponds to heavy rainfall events in Japan (Saito et al., 2010).

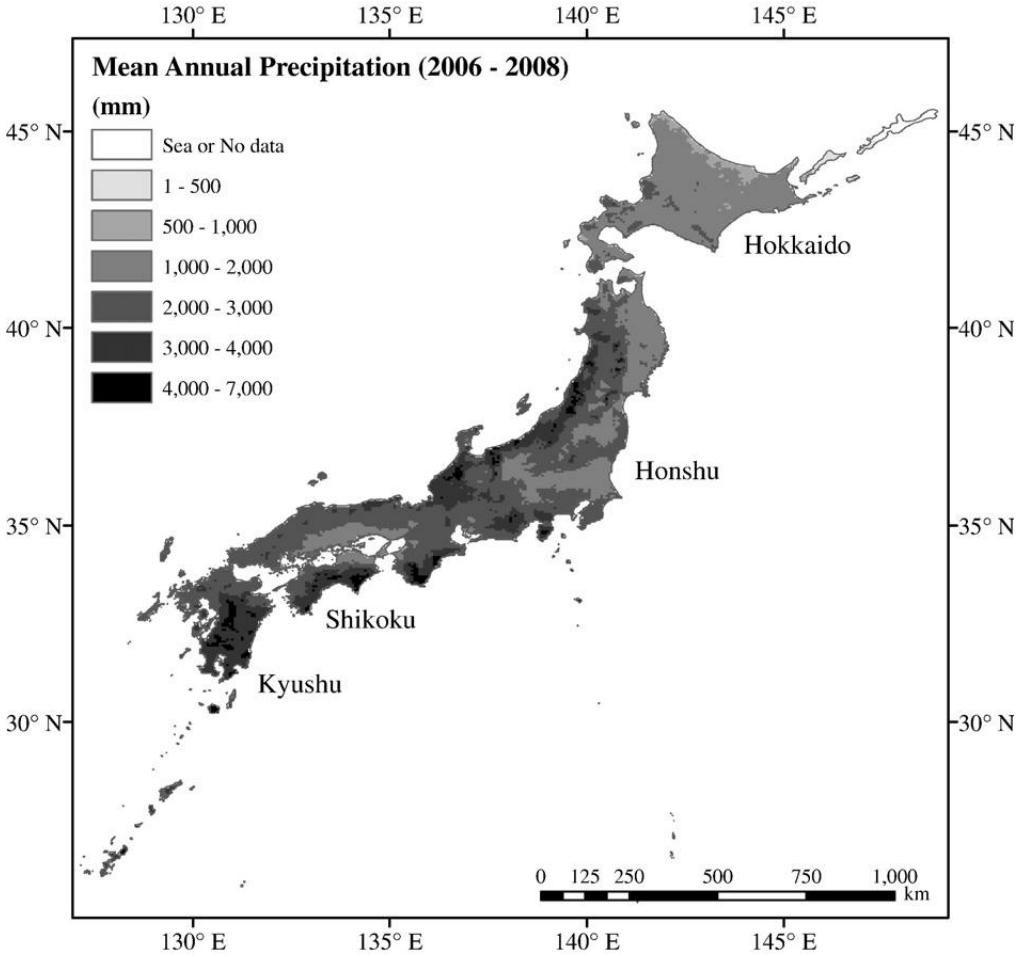

Fig. 1.1 Distribution of mean annual precipitation (MAP) in Japan during 2006–2008 (Saito et al., 2010)

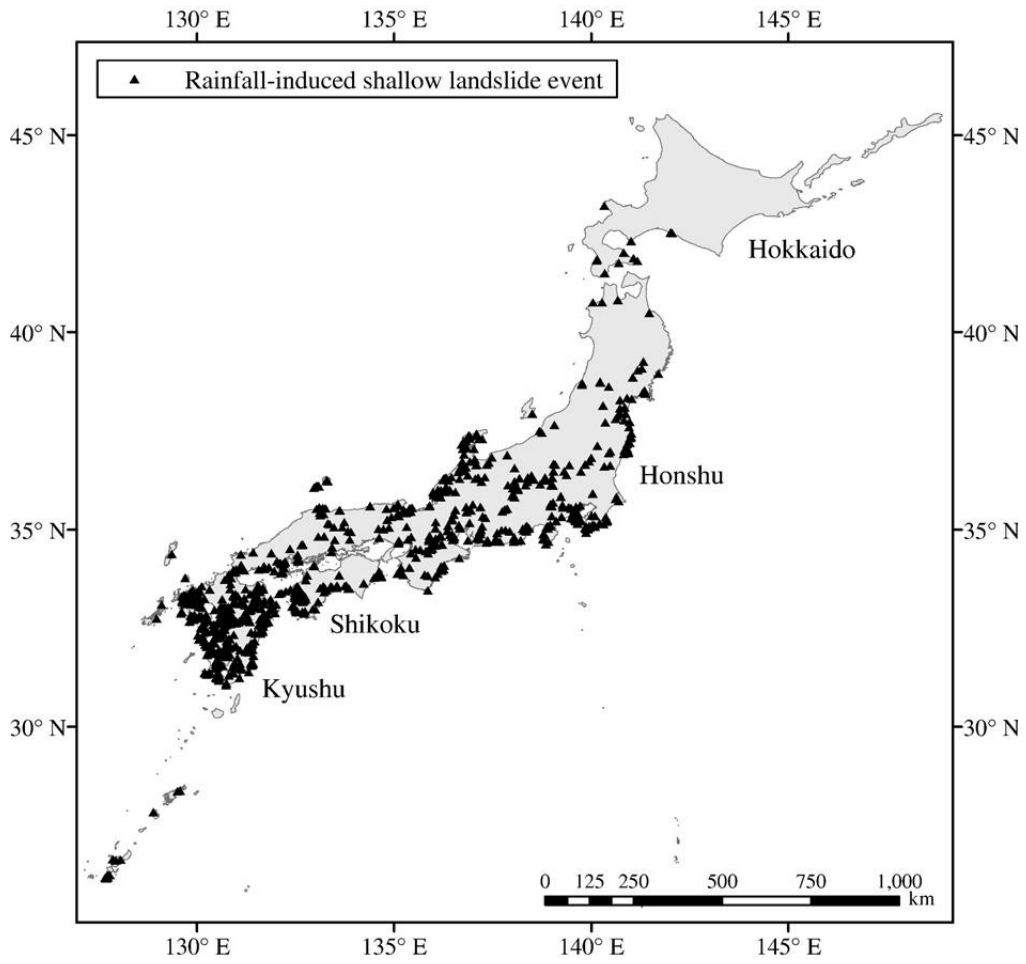

Fig. 1.2 Distribution of 1174 rainfall-induced shallow landslide events in Japan during 2006–2008 (Saito et al., 2010)

Therefore, the time prediction of heavy rainfall-induced shallow landslides in Japan is significant for geo-disaster prevention to reduce the losses of human life and property. More studies and a deep understanding on the initiation mechanism of heavy rainfall-induced shallow landslide are necessary for this challenging target.

1.2 Objectives and scope of study

This research aims to understand the initiation mechanism of heavy rainfall-induced shallow landslides on steep slopes with impermeable bedrock.

The major objectives of the research projective are as follows:

1) To conducted field investigation and soil sampling on heavy rainfall-induced shallow landslides;
2) To determine the physical properties of soil samples from different shallow landslides;
3) To evaluate the effective shear strength of soil sample using consolidated-undrained triaxial compression tests;
4) To examine the soil behavior response to the increase in pore-water pressure using pore-water pressure controlled triaxial tests;
5) To simulate the groundwater level in the soil layer on steep slope with impermeable bedrock;
6) To propose a method for time prediction of shallow landslide during heavy rainfall.

The initiation mechanism of heavy rainfall-induced shallow landslides is investigated which directly leads to above research objectives. The post-failure and landside re-activation mechanism are not within the scope this study.

Three landslide events at Aso caldera in 2012, Izu Oshima Island in 2013 and Hiroshima in 2014 in Japan are selected as the case studies for this research. These study sites present two kinds of widespread landslide-forming materials in Japan. One kind of them is pyroclastic deposits. The other kind of them is the residual soil from weathered granite. These shallow landslides were triggered on steep slopes with impermeable bedrock by heavy rainfall related to typhoons or low-pressure troughs. This research is specifically focused on examining the soil behavior response to the increasing pore-water pressure in two kinds of landslide-forming materials through pore-water pressure controlled triaxial tests.

1.3 Structure of the thesis

The thesis is focused on the theme of understanding the initiation mechanisms of heavy rainfall-induced shallow landslides on steep slopes with impermeable bedrock.

Chapter 2 reviews previous research works on the shallow landslide triggered by heavy rainfall.

Chapter 3 explains the methods used in the field investigation, laboratory experiment, slope stability analysis, and groundwater simulation.

Chapters 4, 5 and 6 describe three case studies, which represent the heavy rainfall-induced shallow landslides on the steep slopes with impermeable bedrock, including slope structure, geology, heavy rainfall and landslides investigation. These chapters present the results of laboratory experiments including physical property tests, consolidated-undrained triaxial tests, and the pore-water pressure controlled triaxial tests.

Chapter 7 introduces a method for time predication of shallow landslides during heavy rainfall. One shallow landslide event was applied to evaluate the feasibility of this method.

Chapter 8 concludes the thesis by highlighting the principal findings.

CHAPTER 2

LITERATURE REVIEW

2.1 Shallow landslide

The system of landslide classification developed by Varnes is the most widely accepted and utilized classification system in the research field of landslide (Varnes, 1954, 1978; Cruden and Varnes, 1996). The Varnes landslide classification presents 29 types of landslides based on the type of movement and type of material (Table 2.1). However, in Varnes's classification system, there is no clear description on shallow landslide. Hungr et al. (2014) revised server aspects of the well-known Varnes classification of landslides. The modified Varnes classification of landslides has 32 landslides types (Table 2.2). The formal definition of gravel/sand/debris slide descried the feature of shallow landslides.

> *"Gravel/sand/debris slide: Sliding of a mass of granular material on a shallow, planar surface parallel with the ground. Usually, the sliding mass is a veneer of colluvium, weathered soil, or pyroclastic deposits sliding over a stronger substrate. Many debris slides become flow-like after moving a short distance and transform into extremely rapid debris avalanches" (Hungr et al., 2014).*

Table 2.1 Varnes's classification of landslide types (Varnes, 1978)

Type of movement		Type of material		
		Bedrock	Engineering soils	
			Predominantly coarse	Predominantly fine
Falls		Rock fall	Debris fall	Earth fall
Topples		Rock topple	Debris topple	Earth topple
Slides	**Rotational**	Rock slide	Debris slide	Earth slide
	Translational			
Lateral spreads		Rock spread	Debris spread	Earth spread
Flow		Rock flow (deep creep)	Debris flow	Earth flow (soil creep)
Complex	Combination of two or more principal types of movement			

Table 2.2 Summary of the proposed new version of the Varnes classification system (Hungr et al., 2014)

Type of movement	Rock	Soil
Fall	1. Rock/ice fall	2. Boulder/debris/silt fall
Topple	3. Rock block topple	5. Gravel/sand/silt topple
	4. Rock flexural topple	
Slide	6. Rock rotational slide	11. Clay/silt rotational slide
	7. Rock planar slide	12. Clay/silt planar slide
	8. Rock wedge slide	13. Gravel/sand/debris slide
	9. Rock compound slide	14. Clay/silt compound slide
	10. Rock irregular slide	
Spread	15. Rock slope spread	16. Sand/silt liquefaction spread
		17. Sensitive clay spread
Flow	18. Rock/ice avalanche	19. Sand/silt/debris dry flow
		20. Sand/silt/debris flowslide
		21. Sensitive clay flowslide
		22. Debris flow
		23. Mud flow
		24. Debris flood
		25. Debris avalanche
		26. Earthflow
		27. Peat flow
Slope deformation	28. Mountain slope deformation	30. Soil slope deformation
	29. Rock slope deformation	31. Soil creep
		32. Solifluction

Milledge (2008) defined that the shallow landslides are always shallow features and have essentially planar slide surface, which usually develop along a boundary between soil materials of different density or permeability. Depth to the failure plane is usually in the range 1 to 4 m and the length of the slide is commonly large compared with its depth. If the shallow landslide occurred during heavy rainfall, it will transform into extremely rapid debris flow.

2.2 Shallow landslide-forming materials

Soil material is one of the most important factors influencing the behavior of landslides. Hungr et al. (2014) consider that geotechnical material terminology is most useful, as it relates best to the mechanical behavior of the landslide. To describe materials modified by geomorphic processes, including landsliding itself, it is necessary to supplement the geotechnical terms by names of mixed materials, namely “debris” and “mud”. Therefore, Hungr et al. (2014) proposed the list of material types, compiled by means of a simplification of existing soil and rock description systems summarized in Table 2.3.

From Table 2.3, it can be observed that landslide can occur in a wide range of geotechnical material. From strong rock to soft clay, from big-size boulder to fine-size silt and from dry soil to saturated soil, all the material can be landslide-forming material. However, for the shallow landslide, loose and granular soil is close to an ideal frictional medium and tends to fail as a thin layer of instability. The most typical shallow landslide-forming materials are colluvial and residual soils, overlying denser and stronger soil deposits, or bedrock, which is very common in all mountainous and hilly regions of the world (Hungr et al., 2014). In regions close to centers of explosive volcanism, an unstable surficial soil layer is formed of pyroclastic deposits over steep bedrock slopes (Guadagno et al., 2005; Picarelli et al., 2008). For example, in the Aso caldera, which is one of the biggest caldera in the world, shallow landslides and debris flows are commonly triggered around the rim during heavy rainfall (Paudel et al., 2003,

2008; Miyabuchi et al., 2004, 2007; Miyabuchi and Sugiyama, 2011; Miyase, 2012; Matsushi et al., 2013). In Hong Kong, numbers of shallow landslide occurred in the volcanic soils which are derived from Meszoic rhyolite lava and tuff and Mesozoic crystalline tuff (Au, 1998; Dai et al., 1999a, 1999b; Ng and Chiu, 2001; Dai and Lee, 2002; Ng, 2007). In Japan, many researchers discussed the relationship between the weathered granite and the occurrence of shallow landslides, and pointed out that shallow landslides occur distinctively in the weathered granitic areas (Oyagi, 1968; Hasegawa and Saito, 1991; Onda, 1992; Chigira and Ito, 1999; Chigira, 2001; Dahal et al., 2009). For example, Oyagi (1968) reported that numerous shallow landslides occurred in the areas of weathered granite after a rainstorm in Shimane Prefecture, western Japan, in 1964. Hasegawa and Saito (1991) found that most of the slides were shallow and translational in nature, with the failure surface located along the contact between relatively less weathered granite. Onda (1992) studied weathering profiles of granite underlying Obara village, Aichi Prefecture, central Japan. Chigira and Ito (1999) and Chigira (2001) described that the fast weathering phenomena and repeated failure mechanism on granitic terrain in Hiroshima Prefecture. Recently, Dahal et al. (2009) also report that the occurrence of shallow landslides in the granitic terrain of northeast Shikoku Island, Japan, along with rainfall and failure relationships during Typhoon 0423 (Tokage) of 2004. Not only in Japan but also in other granitic terrain regions, the occurrence of shallow landslides in weathered granite also is common, such as in the granite areas of Rio de Janeiro (Durgin, 1977), Southern Italy (Calcaterra et al., 1996), Hong Kong (Irfan, 1998; Dai et al., 1999a, 1999b; Dai and Lee, 2002), Korean peninsula (Kim et al., 2004) and Malaysia (Chigira, 2011).

Hungr et al. (2014) summarized that such soil materials are highly susceptible to shallow landslides for several reasons: (1) The soil in upper layers are much weaker than the underlying material and are able to persist on steep slopes only by virtue of cementing, negative pore-pressures due to incomplete saturation, or vegetation root reinforcement. (2) In many cases, the interface between the soil layer and the substrate

is smooth and therefore weaker than the soil itself. (3) The contrasting permeability of the soil layer and substrate may promote rapidly recharging perched water tables and slope-parallel flow, or destabilizing upward seepage.

Table 2.3 Landsliding-forming material types (Hungr et al., 2014)

Material name	**Character descriptors (if important)**	**Simplified field description for the purposes of classification**	**Corresponding unified soil classes**	**Laboratory indices (if available)**
Rock	Strong	Strong—broken with a hammer		UCS > 25 MPa
	Weak	Weak—peeled with a knife		2 < UCS < 25 MPa
Clay	Stiff	Plastic, can be molded into standard thread when moist, has dry strength	GC, SC, CL, MH, CH, OL, and OH	$I_P > 5$
	Soft			
	Sensitive			
Mud	Liquid	Plastic, unsorted remolded, and close to Liquid Limit	CL, CH, and CM	$I_P > 5$ and $I_L > 50$
Silt, sand, gravel, and boulders	Dry	Nonplastic (or very low plasticity), granular, sorted. Silt particles cannot be seen by eye	ML	$I_P < 5$
	Saturated		SW, SP, and SM	
	Partly saturated		GW, GP, and GM	
Debris	Dry	Low plasticity, unsorted and mixed	SW-GW	$I_P < 5$
	Saturated		SM-GM	
	Partly saturated		CL, CH, and CM	
Peat	Organic			
Ice	Glacier			

2.3 Rainfall-induced shallow landslide

The slope, on which shallow landslides frequently occurred, can be assumed as an infinite slope due to $H << L$, where H is the prospective slip surface depth and L is the prospective length or width of shallow soil layer. The sliding is assumed to occur along a plane slip surface parallel to the surface of the slope (Taylor, 1948). Generally, one-dimensional infinite-slope stability analysis, which neglects all forces not resolvable on planes that parallel the ground surface, is used to evaluate the potential for slope failure at diverse locations within a landscape (Montgomery and Dietrich, 1994;

Wu and Sidle, 1995; Borga et al., 1998; Iverson, 2000; Morrissey et al., 2001; Crosta and Frattini, 2003; Collins and Znidarcic, 2004; Duncan and Wright, 2005; Tsai and Yang, 2006; Tsai, 2008; Tsai et al., 2008; Tsai and Wang, 2011). Duncan and Wright (2005) gave a detailed description on the equilibrium equations which are derived by considering a rectangular block (AA'B'B) like the one shown in Fig. 2.1. Summing forces in directions perpendicular and parallel to the slip plane gives the following expressions for the shear force, *S*, and normal force, *N*, on the plane:

$$S = \gamma l H \cos\alpha \sin\alpha \tag{2.1}$$

$$N = \gamma l H \cos^2\alpha \tag{2.2}$$

where, α is the angle of inclination of the slope and slip plane. γ is the total unit weight of the soil. l is the distance between the two ends of the block, measured parallel to the slope. H is the vertical depth to the shear plane.

The shear and normal stresses on the shear plane are constant for an infinite slope and are obtained by dividing Eqs. (2.1) and (2.2) by the area of the plane ($l \cdot 1$), to give

$$\tau = \gamma H \cos\alpha \sin\alpha \tag{2.3}$$

$$\sigma = \gamma H \cos^2\alpha \tag{2.4}$$

The shear resistance of soil material can be expressed by the Mohr-Coulomb equation as Eq. (2.5).

$$\tau_f = c + \sigma \tan\phi \tag{2.5}$$

where, c and ϕ are the cohesion and friction angle for the soil.

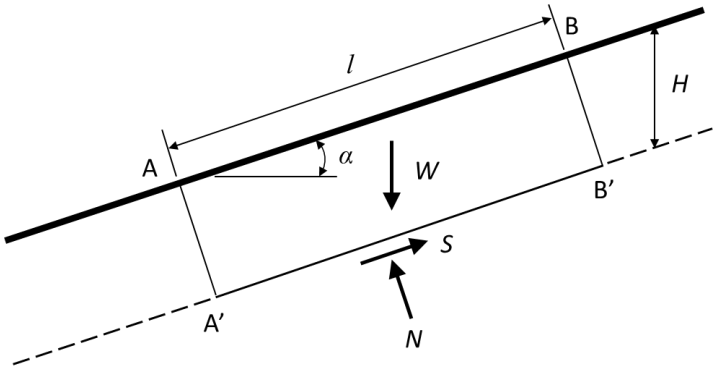

Fig. 2.1 Infinite slope and plane slip surface (modified from Duncan and Wright, 2005)

Incipient failure of infinite slopes is described by an equation that balances the downslope component of gravitational driving stress against the resisting stress (Iverson, 2000). Their relative relationship is expressed as a ratio of shear resistance to shear stress, known as the factor of safety, F_S:

$$F_S = \frac{\text{Shear resistance } (\tau_f)}{\text{Shear stress } (\tau)} \tag{2.6}$$

On a natural slope with shallow soil layer during rainfall, the shear stress is approximately constant due to gravity. However, the shear resistance (τ_f) will have a significant change. Therefore, most of studies on the initiation mechanism of rainfall-induced shallow landslide focus on the effect of rainfall on the shear resistance (τ_f).

For the rainfall-induced shallow landslide on the slopes in an unsaturated condition, i.e., the rainfall is not heavy or rainfall infiltration is limited, most studies were focused on the decrease of cohesion and mastic suction due to wetting or saturation process in soil layer.

By definition, cohesion is the stress of sticking together. In engineering mechanics, particularly in soil mechanics, cohesion refers to shear strength under zero normal stress, or the intercept of a material's failure envelope with shear stress axis in the shear stress-normal stress space (Lu and Likos, 2013). Cohesion under saturated drained

conditions is called drained cohesion and under variably saturated conditions is called apparent cohesion (Lu and Likos, 2013). For the at the potential slid plane under unsaturated condition, the apparent cohesion decreases with increasing soil moisture (Fredlund et al., 1978; Escario and Sáez, 1986; Gan et al., 1988; Vanapalli et al., 1996; Miao et al., 2002; Lee et al., 2003; Matsushi and Matsukura, 2006, 2007; Matsushi, 2007). The cohesive strength of an unsaturated soil plays an important role in the stability of soil slope. Reduction of the soil cohesion due to wetting can cause shear deformation of the slopes at a previously unsaturated shallow soil layer. The cohesive of soil will decrease with increasing moisture content and approach a minimum value at saturated condition (Matsushi, 2007). Matsushi and Matsukura (2006) observed that the reduction characteristics of the soil shear strength suggest: (1) the angle of shearing resistance takes a constant value independent of volumetric water content of the soil; (2) the soil cohesion is an exponential function of volumetric water content. There presumptions lead to formulation of the decrease in soil shear strength:

$$\tau = ce^{-\mu\theta} + \sigma' \tan \phi' \tag{2.7}$$

where, c is the apparent soil cohesion at dry condition. μ is the coefficient related to susceptibility of strength reduction ($\mu > 0$). σ' is the effective normal stress. ϕ' is the effective angle of shearing resistance. θ is the volumetric water content. Note that c is a hypothetical ultimate value when $\theta = 0$; an increase in μ cause a significant reduction of cohesive.

The shear strength of soil with matric suction (i.e. negative pore-water pressure) also plays an important role in the stability of a slope, particularly when the slip surfaces are shallow (Krakn et al., 1989). For prediction of the shear strength of an unsaturated soil, two approaches had been proposed by Bishop (1959) (effective stress approach) and Fredlund et al. (1978) (independent stress variables approach).

Bishop (1959) showed that the shear strength of an unsaturated soil can be

represented by the equation:

$$\tau = c' + [(\sigma - u_a) + \chi(u_a - u_w)] \tan \phi' \quad (2.8)$$

where, c' is the effective cohesion. ϕ' is the effective friction angle. σ is the total normal stress. u_a is the pore-air pressure. u_w is the pore-water pressure. $u_a - u_w$ is the matric suction (i.e. negative pore-water pressure). χ is the effective stress parameter.

There are many experimental evidences showing that the effective stress parameter of unsaturated soil is a highly nonlinear function of the matric suction (Gan et al., 1988; Escario et al., 1989; Vanapalli et al., 1996). A convenient and accurate representation of effective stress parameter (Vanapalli and Fredlund, 2000; Lu and Likos, 2004) was proposed as follows:

$$\chi = \frac{\theta - \theta_r}{\theta_s - \theta_r} \quad (2.9)$$

where, θ_r and θ_s are the residual water content and saturated water content, respectively.

Fredlund et al. (1978) showed that the shear strength of an unsaturated soil can be represented by the equation

$$\tau = c' + (u_a - u_w) \tan \phi^b + (\sigma - u_a) \tan \phi' \quad (2.10)$$

where, c' is the effective cohesion. ϕ' is the effective friction angle. σ is the total normal stress. u_a is the pore-air pressure. u_w is the pore-water pressure. $u_a - u_w$ is the matric suction (i.e. negative pore-water pressure). ϕ^b is an angle indicating the rate of increase in shear strength with respect to changes in $u_a - u_w$.

The strength parameter, ϕ^b, can be measured using triaxial test on unsaturated samples. The test equipment and procedures were developed by Ho and Fredlund

(1982). Field monitoring of in-situ matric suction in slopes had been conducted by a number of researchers (Chipp et al., 1982; Sweeney, 1982; Krahn et al., 1989; Macari et al., 1992; Affendi and Faisal, 1994; Lim et al., 1996). Tensiometers are commonly used in the field instrumentation to measure matric suction in the soil.

When the rainfall is heavy, the obvious groundwater level or seepage will generate in the shallow soil layer. For the steep slope with impermeable bedrock, the groundwater level in the slope parallels to slope surface (Duncan and Wright, 2005). In this condition, the study on initiation mechanism of rainfall-induced shallow landslide is focused on the shear strength of soil with the increase in pore-water pressure.

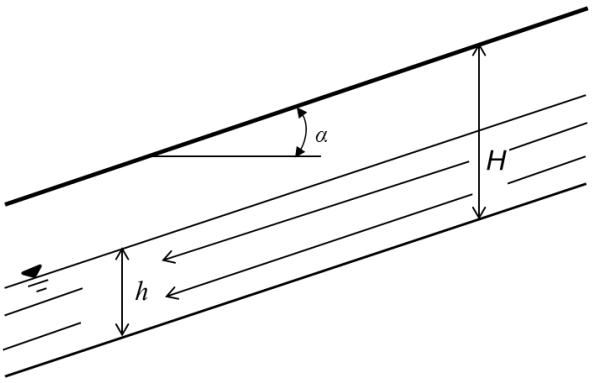

Fig. 2.2 Infinite slope with groundwater level which parallels to slope surface (modified from Duncan and Wright, 2005)

For the effective stresses, ($\sigma - u$) is the effective stress, as defined by Terzaghi (1936), in its original form:

$$\sigma' = \sigma - u \tag{2.11}$$

The factor of safety (F_S) becomes

$$F_S = \frac{c' + (\sigma - u)\tan\phi'}{\gamma H \cos\alpha \sin\alpha} \tag{2.12}$$

or

$$F_S = \frac{c' + (\gamma H \cos^2 \alpha - u) \tan \phi'}{\gamma H \cos \alpha \sin \alpha} \quad (2.13)$$

where, *c'* and ϕ' represent the shear strength parameter in terms of effective stress. *u* is the pore-water pressure.

Based on this equation, the triggering mechanism of rainfall-induced landslides on shallow hillslopes can be attributed to the increase in pore-water pressure. The increase in pore-water pressure as a result of rainfall infiltration progressively reduces the normal effective stress of the slope materials acting on a potential shear surface (Ng, 2007). This has been termed "hydrological triggering" by Terlien (1998).

Recent studies on the initiation failure of slope response to groundwater or pore-water pressure have been undertaken using field monitoring (Simon et al., 1990; Irfan, 1994; Nicholson et al., 1996; Au, 1998; Kwong et al., 1999; Chang et al. 2005; Ng, 2007), physical and numerical modelling (Gasmo et al., 2000; Ng et al., 2001; Wang and Sassa, 2001, 2003; Tsaparas et al., 2002; Wang et al., 2002; Lan et al., 2005; Jiao et al., 2005; Lourenço et al., 2006; Wang and Shibata, 2007; Wu et al., 2015). Most of studies discussed about the process of slope failure during rainfall. However, our understanding on the soil behavior response to the increase in pore-water pressure remains poor. Therefore, more studies are needed to understand how subsurface-water dynamics influence landslide initiation.

CHAPTER 3

METHODOLOGY

3.1 Field investigation

Three sites of shallow landslides events in the past three years were selected for case studies. They are the rainfall-induced shallow landslides in Aso caldera in 2012, Izu Oshima Island in 2013 and Hiroshima in 2014 (Fig. 3.1). All study sits are located in the high precipitation region. During the field investigation, observation of the geological conditions, measurement of the longitudinal and cross-sectional profiles, and the collection of soil samples were the main objectives.

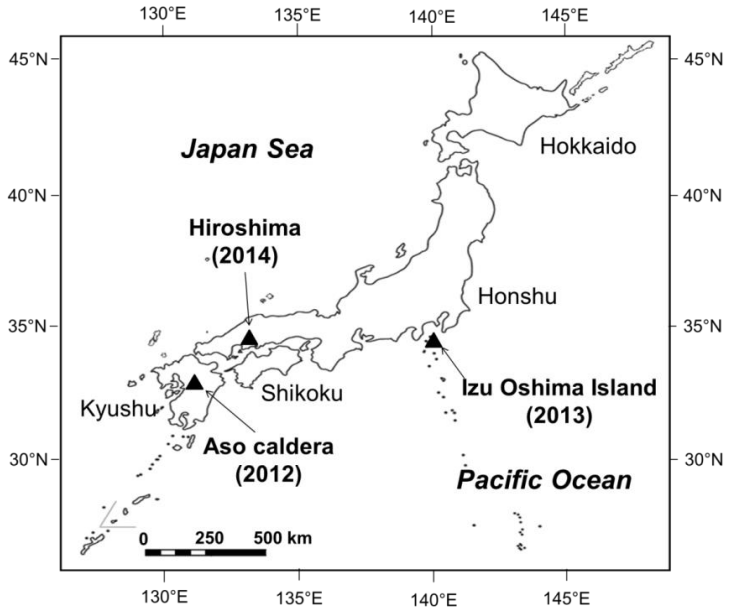

Fig. 3.1 Locations of study sites

3.2 Laboratory experiments

The laboratory experiments involved: (1) Physical property tests, (2) consolidated-undrained triaxial compression tests, and (3) pore-water pressure controlled triaxial tests

3.2.1 Physical property tests

These tests were conducted to determine the physical properties of the soil sample from shallow landslides. Through these parameters, the soil classification can be determined on the soil samples from three study sites. Moreover, these parameters are necessary for specimen preparation of triaxial tests. All tests were performed according to the standards of the Japanese Geotechnical Society (JGS, 2010).

Table 3.1 Physical property tests for soil samples (modified from Ng, 2007)

Test	**Descriptions**
Grain size analysis	Expresses the different size grades of particles in a soil in term of percentages, by weight
Specific gravity	Ratio of soil weight to an equal volume of water
Atterberg limits	Consistency limits describe the three states (solid, plastic, liquid) of cohesive soils depending on their moisture content, while the boundaries between these states are referred to as the plastic limit (*PL*) and the liquid limit (*LL*).
Void ratio	Ratio of volume of voids to volume of solids
In-situ dry density	Mass of the dry soil divided by the total volume
Water content	Ratio of mass of water to mass of solids

3.2.2 Consolidated-undrained (CU) triaxial compression test

3.2.2.1 Test equipment

The principle of triaxial apparatus has been described in detail by Bishop and Henkel (1962). The test specimen is a cylinder shape with an aspect ratio of two (i.e., height and diameter of specimen are 100 and 50 mm, respectively), which is sealed by a rubber membrane attached by rubber O-rings to a base pedestal and top cap. Water pressure inside the cell provides the horizontal principal total stresses, while the vertical pressure at the top cap is produced by the cell pressure and the ram force. The use of an aspect ratio of two ensures that the effects of the radial shear stresses between soil, and top cap and base-pedestal are insignificant at the center of the specimen. The test apparatus (Model: DTC-453), which was used for this study, is produced by the SEIKEN, Inc., Japan.

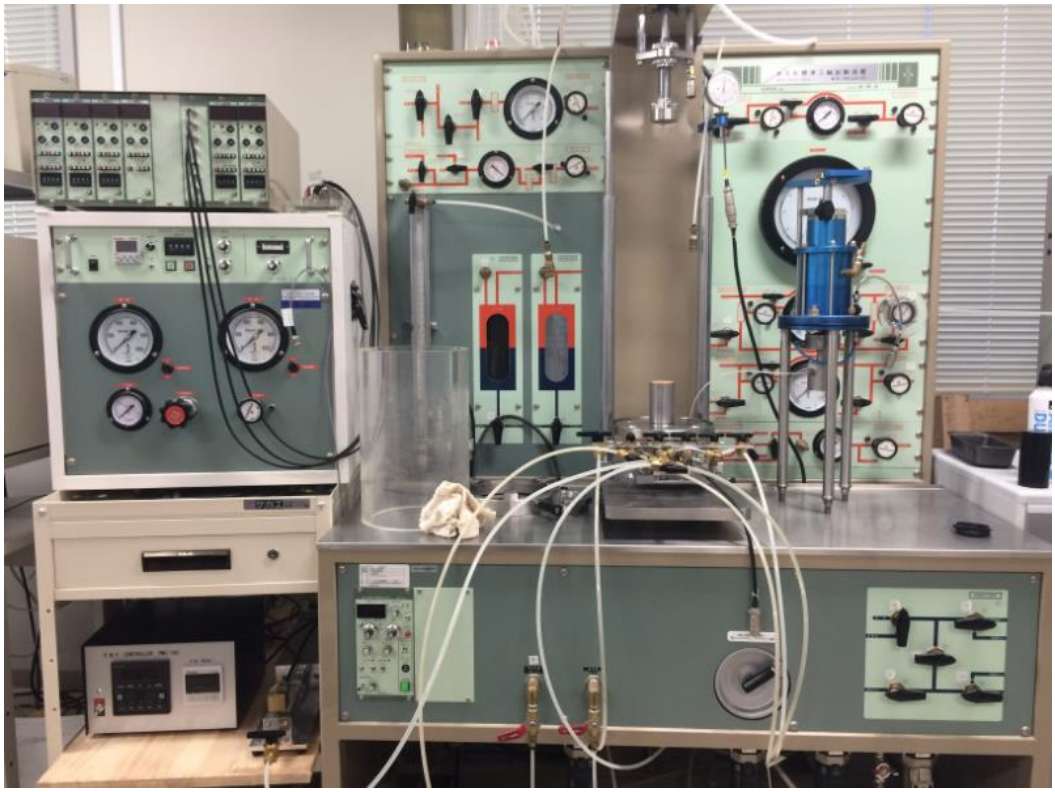

Fig. 3.2 The triaxial test apparatus

3.2.2.2 Specimens preparation

According to the in-situ soil dry density, a given mass of dry soil passing 2 mm

sieving was used to make a cylindrical specimen. In order to get a homogeneous specimen, the dry soil sample was divided into three parts to fill the cylindrical specimen tube with rubber member. After filled the all soil into the specimen tube, the cylindrical surface of each sample was covered by a rubber membrane which is sealed by rubber O-rings on the top and base of the load system. After the specimen preparation, the diameter and the height of the trimmed samples were measured using a caliper.

3.2.2.3 Specimens saturation

The specimens were saturated following the saturation process. Carbon dioxide (CO_2) is slowly supplied from the base of the tube to gradually replace the air within the specimen. De-aired water is then supplied to replace and absorb the CO_2 and achieve a saturated state. If a sample is 100% saturated and no pore water drainage is allowed to occur, an increase in the confining stress (σ_3) on the sample should result in an equivalent change in pore pressure (u). The Skempton's B value, which is called pore pressure coefficients (Skempton, 1954), can be expressed in the non-dimensional form:

$$B = \frac{\Delta u}{\Delta \sigma_3} \tag{3.1}$$

A triaxial test specimen with a B value of 0.95 or greater is usually considered saturated (Head, 1998).

3.2.2.4 Consolidation

The consolidation process was then undertaken on the saturated specimens by the application of isotropic confining pressure ($\sigma_1 = \sigma_3$). Consolidation was completed when there was no further significant volume change and excess pore-water pressure due to the applied stress was dissipated.

3.2.2.5 Undrained compression

After normal consolidation, the specimens were compressed at an axial strain of 1.0% per minute under the undrained condition. Vertical load, pore-water pressure and vertical displacement data was recorded by a data logging system. The shear strength parameters can be obtained from these tests.

3.2.3 Pore-water pressure controlled (PPC) triaxial test

3.2.3.1 Test principle

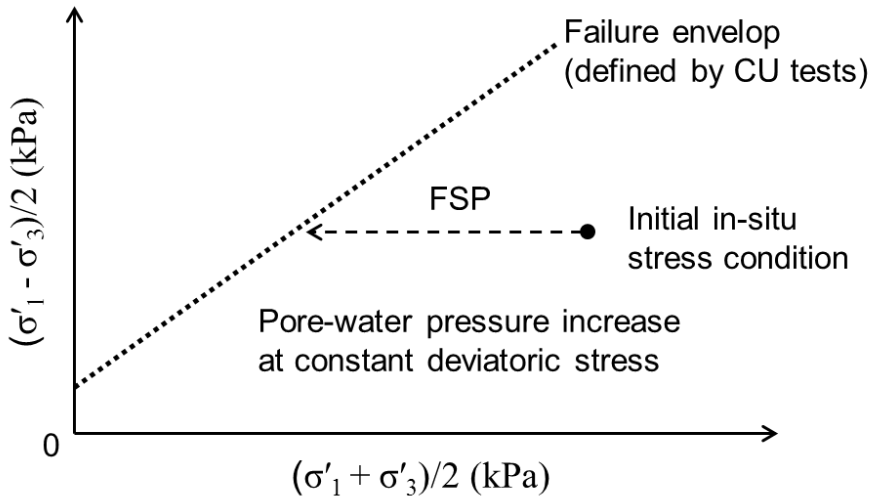

Fig. 3.3 The concept of the pore-water pressure controlled (PPC) triaxial test (modified from Ng, 2007)

The pore-water pressure controlled (PPC) test was designed to simulate the initiation process of the rainfall-induced landslide. The experimental procedures were firstly described by Bishop and Henkel (1962). After that, Brand (1981) developed this method and gave the concept of "field stress path" (FSP) to explain the initiation mechanism of rainfall-triggered landslides (Fig. 3.3). The key features of FSP include (1) increasing pore-pressure at a constant total normal stress (and hence decreasing the effective stress) and (2) constant shear stress (Ng, 2007). The former simulates the main process leading to rainfall-triggered landslides. While, the latter is related to the

approximately constant gravity-induced shear stress on a planer slope and the negligible load of infiltrating rainfall (Zhu and Anderson, 1998). The stress paths obtained from the consolidated-undrained (CU) triaxial compression test are used to determine the shear strength of slope materials. Because the CU tests are conducted with the increasing of axial load at constant displacement, these tests do not represent the field conditions (Gan and Fredlund, 1996). In contrast to the CU tests, the pore-water pressure controlled (PPC) triaxial tests well simulate the field condition and provide a good way to understand the initiation soil behavior within a landslide during heavy rainfall.

Many researchers applied this method for their studies. With different test conditions and purposes, the FSP has been named as the "constant dead load (CDL) test" (Brenner et al., 1985; Chen et al., 2000, 2004), "constant shear drained (CSD) test" (Anderson and Sitar, 1995; Anderson and Riemer, 1995; Santos et al., 1996; Zhu and Anderson, 1998; Chu et al., 2003; Springman et al., 2003; Farooq et al., 2004; Lourenco et al., 2006), "constant deviatoric stress path (CQD)" (Dai et al., 1999b) and "pore pressure reinflation (PPR) test" (Petley et al., 2005; Ng, 2007). Previous tests have used both undisturbed and disturbed samples under saturated and unsaturated conditions. These tests have been mostly undertaken on soil samples at a high mean effective stress (100-1000 kPa) and a low increase rate of pore-water pressure (< 2 kPa/hour). However, for the characteristics of shallow landslide and heavy rainfall, a low mean effective and a high increase rate of pore-water pressure will be better to simulate the field condition of heavy rainfall-induced shallow landslide.

3.2.3.2 Test equipment

In addition to the load system which is same as the CU tests, a pore-water pressure controller system is used for the PPC triaxial test. The pore-water pressure controller system includes two parts (Fig. 3.4). One part is the de-aired water supplier. The de-aired water in the cylinder tank is supplied by the movement of a steel piston. The

other part is the pore-water pressure controller, which is used to control the increase rate of pore-water pressure by controlling the movement rate of the steel piston in de-aired water tank.

Fig. 3.4 Pore-water pressure controller system

3.2.3.3 Test process

The process of specimen preparation and saturation was the same as that for the consolidated-undrained triaxial compression tests. In contrast to the isotropic consolidated-undrained triaxial compression test, the specimen was consolidated under nonisotropic confining stress. The axial and lateral confining stresses can be obtained according to the vertical and lateral earth pressure. Through this step, the initial stress condition of the soil at the potential sliding zone is simulated. After consolidation, de-aired water is supplied to the specimen by a pore-water pressure controller to increase the pore-water pressure. Through this step, the effect of pore-water pressure accumulation on the potential sliding surface is simulated, and the failure process can be observed.

3.3 Slope stability analysis

A simplified infinite slope model for slope stability analysis can be assumed (Fig. 3.5) based on the characteristics of slopes on which shallow landslides occurred.

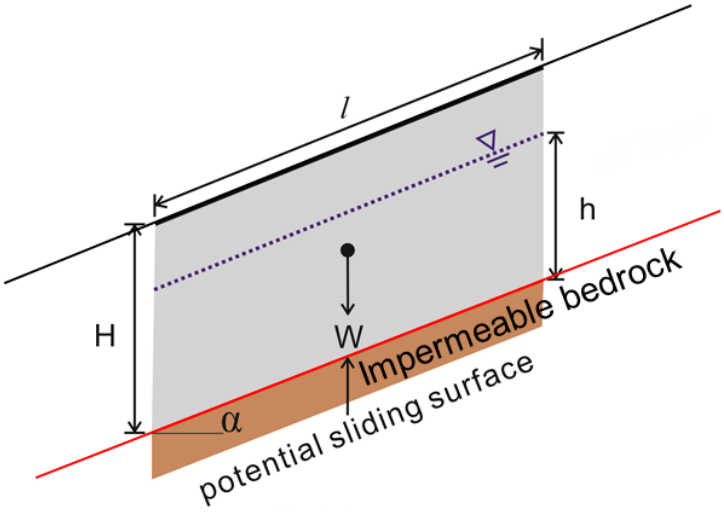

Fig. 3.5 Simplified slope model for stability analysis

The factor of safety (F_S) of the infinite slope can be obtained using Eqs. (3.2) and (3.3).

$$F_S = \frac{c' + (\gamma H \cos^2\alpha - u)\tan\phi'}{\gamma H \sin\alpha \cos\alpha} \tag{3.2}$$

$$u = \gamma_w h \cos^2\alpha \tag{3.3}$$

where,

H is the vertical depth of the soil layer;

h is the height of groundwater level;

α is the slope angle;

γ is the unit weight of soil;

γ_w is the unit weight of water;

c' is the effective cohesion of soil;

ϕ' is the effective friction angle soil.

u is the pore-water pressure on the potential sliding surface.

For the cohesionless soil, Eqs. (3.2) and (3.3) can be simplified as follows:

$$F_S = \left(1 - \frac{\gamma_w}{\gamma} \cdot \frac{h}{H}\right) \frac{\tan \phi'}{\tan \alpha} \tag{3.4}$$

3.4 Groundwater simulation

Based on Bansal's model (Bansal and Das, 2010; Bansal, 2014), Faris and Wang (2014) developed the groundwater model for thin soil layer overlying on steep slopes with impermeable bedrock. This model was used to conduct groundwater simulation in this research. The detail of this model is described by Faris and Wang (2014) as follows.

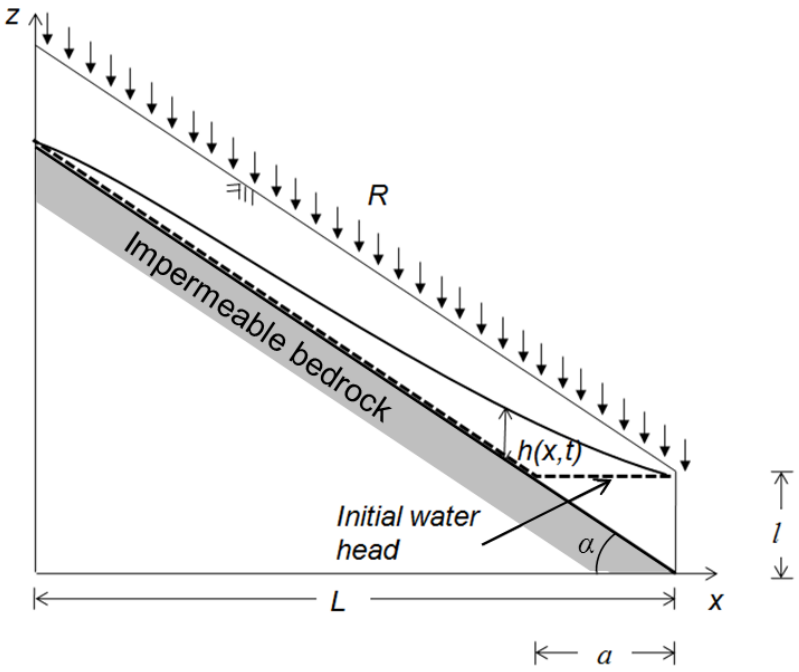

Fig. 3.6 Scheme of groundwater model by rainfall infiltration (Faris and Wang, 2014)

The Boussinesq formula as the governing equation of the model is written as Eq. (3.5) (Bansal, 2014).

$$k\left\{\frac{\partial}{\partial x}\left(h\frac{\partial h}{\partial x}\right)-\tan\alpha\frac{\partial h}{\partial x}\right\}\cos^2\alpha+R=S\frac{\partial h}{\partial t} \tag{3.5}$$

where, h is the height of phreatic surface measured above the impermeable bedrock in the vertical direction. k and S respectively are the hydraulic conductivity and specific yield of the aquifer. R is the net rate of recharge of infiltrated rainfall, and α is the slope angle.

The nonlinear Boussinesq equation can be solved numerically using the Mac Cormack scheme of explicit finite difference method (Bansal, 2014). The Eq. (3.5) can be modified to Eq. (3.6):

$$\frac{\partial h}{\partial t}=C_1\frac{\partial}{\partial x}\left(h\frac{\partial h}{\partial x}\right)-C_2\frac{\partial h}{\partial x}+\frac{R}{S} \tag{3.6}$$

where, $C_1 = (k\cos^2\alpha)/S$ and $C_2 = (k\sin 2\alpha)/2S$. Mac Cormack scheme is an explicit finite difference with predictor-corrector step. The predictor step is applied by replacing the spatial and temporal derivatives by forwards difference to obtain predicted value of h, indicated as h^* in Eq. (3.7).

$$h^*_{n,t+1}=h_{n,t}+C_1\frac{\Delta t}{(\Delta x)^2}\left[h_{n+1,t}\left(h_{n+1,t}-h_{n,t}\right)-h_{n,t}\left(h_{n,t}-h_{n-1,t}\right)\right]-C_2\frac{\Delta t}{\Delta x}\left(h_{n+1,t}-h_{n,t}\right)+\frac{R}{S}\Delta t \tag{3.7}$$

where, subscript n and t are respectively spatial and time identifier. The corrector step is then obtained by replacing the space derivative by rearward difference, while the time derivative is preserved using forward difference approximation. Then Eq. (3.8) can be obtained.

$$h_{n,t+1}^{**} = h_{n,t} + C_1 \frac{\Delta t}{(\Delta x)^2}\left[h_{n,t+1}^{*}\left(h_{n+1,t+1}^{*} - h_{n,t+1}^{*}\right) - h_{n-1,t+1}^{*}\left(h_{n,t+1}^{*} - h_{n-1,t+1}^{*}\right)\right] - C_2 \frac{\Delta t}{\Delta x}\left(h_{n,t+1}^{*} - h_{n-1,t+1}^{*}\right) + \frac{R}{S}\Delta t \quad (3.8)$$

The final value of $h_{n,t+1}$ is simply obtained from arithmetic mean of $h_{n,t+1}^{*}$, and $h_{n,t+1}^{**}$ from Eqs. (3.7) and (3.8), respectively, and the Eq. (3.9) is obtained.

$$h_{n,t+1} = \frac{1}{2}\left\{h_{n,t} + h_{n,t+1}^{*} - C_2 \frac{\Delta t}{\Delta x}\left(h_{n,t+1}^{*} - h_{n-1,t+1}^{*}\right) + C_1 \frac{\Delta t}{(\Delta x)^2}\left[h_{n,t+1}^{*}\left(h_{n+1,t+1}^{*} - h_{n,t+1}^{*}\right) - h_{n-1,t+1}^{*}\left(h_{n,t+1}^{*} - h_{n-1,t+1}^{*}\right)\right]\right\} + \frac{R}{S}\Delta t \quad (3.9)$$

The applied initial condition was used such as to simulate the water level condition in dry condition. Thus, the initial and boundary condition are defined by Eqs. (3.10), (3.11), and (3.12).

$$h(x, t=0) = \begin{cases} 0, & x < L - x_0 \\ z_0 + (x - L)\tan\alpha, & x > L - x_0 \end{cases} \quad (3.10)$$

$$h(0, t) = 0 \quad (3.11)$$

$$h(L, t) = z_0 \quad (3.12)$$

The hydraulic conductivity parameter, *k*, was determined using the Eq. (3.13), which was established by Kozeny-Carman (Odong, 2007).

$$k = \frac{g}{\eta} \times 8.3 \times 10^{-3}\left[\frac{n^3}{(1-n)^2}\right] D_{10}^2 \quad (3.13)$$

where, g is the gravitational acceleration (= 9.8 m/s^2). η is the kinematic viscosity of water at 20°C (10^{-6} m^2/s). n is the effective porosity. D_{10} is the effective grain size in mm.

The specific yield, *S*, was estimated from relation curve provided by Eckis (1934) in Robson (1993). Based on the category of the soil, the specific yield, *S*, can be determined using the Eq. (3.14).

$$S = n - 0.03 \tag{3.14}$$

where, *n* is the effective porosity.

CHAPTER 4

RAINFALL-INDUCED SHALLOW LANDSIDES IN ASO CALDERA, JAPAN, IN 2012

4.1 Introduction

The Northern Kyushu area of Japan experienced high-intensity rainfall from 11 to 14 July, 2012. This heavy rainfall triggered many shallow landslides, especially on the northeastern rim of Aso caldera (Fig. 4.1). These shallow landslides, as the resource for debris flows, occurred on the upper slopes, at the inner rim of caldera. Trees growing along the gullies on the middle slopes were carried away by the debris flows. Many sabo dams (i.e. check dams) in the path of the debris flows were destroyed. The debris flows affected many villages and local settlers. The debris flows claimed 30 lives, with another two people remaining unaccounted for, and 13,263 houses were completely or partially damaged (Fire and Disaster Management Agency, Japan, 2012). Transport routes and large areas of farmland were also affected. The total property loss was estimated to be about 2 billion USD (JSCE, 2013).

Shallow landslides often occur in weathered debris or loose soil materials on steep slopes during heavy rainfall (Maharaj, 1993; Zhu and Anderson, 1998; Dai et al., 1999a, 2004; Dai and Lee, 2002; Capra et al., 2003; Yu et al., 2006, Dahal et al., 2009; Giannecchini et al., 2012; Yang et al., 2015; Wang et al., 2015). Annual rainfall in Kyushu is quite high, due to stagnation of wet fronts in the area during the rainy season, from May to July. Normally, few landslides occur during limited rainfall. However, during heavy rainfall events, shallow landslides and debris flows are commonly

triggered around the rim of Aso caldera (Miyabuchi et al., 2004, 2007; Miyase, 2012; Matsushi et al., 2013). It is obvious that heavy rainfall is the main triggering factor of these geo-disasters. Several studies have been carried out to examine the factors contributing to the occurrence of shallow landslides in Kyushu. Paudel et al. (2003, 2008) and Miyabuchi and Sugiyama (2011) reported that the soils on the slopes consisted of different layers, and the slip surfaces of most landslides formed between upper blackish and lower brownish tephra layers. Paudel et al. (2007) evaluated the spatio-temporal patterns of historical shallow landslides in Aso caldera, based on statistical analysis of shallow landslides that occurred between 1953 and 1998. Kasama et al. (2011) recently tried to clarify the factors which led to these geo-disasters, based on geo-mechanical and hydro-mechanical evaluation.

Fig. 4.1 Shallow landslides on the northeastern rim of Aso caldera (image courtesy of Kokusai Kogyo Co., Ltd, Japan)

One landslide site on Aso caldera was selected for this study to examine the triggering mechanism of the shallow landslides during heavy rainfall. The main objectives of our field investigations were observation of the geological conditions, measurement of the longitudinal profile, and collection of soil samples for laboratory analysis. Laboratory experiments were conducted to determine the physical and

mechanical properties of the soils, and soil behavior in response to increase in pore-water pressure. Based on the results of our field and laboratory investigations, we propose a probable triggering mechanism for the rainfall-induced shallow landslides on the northeastern rim of Aso caldera.

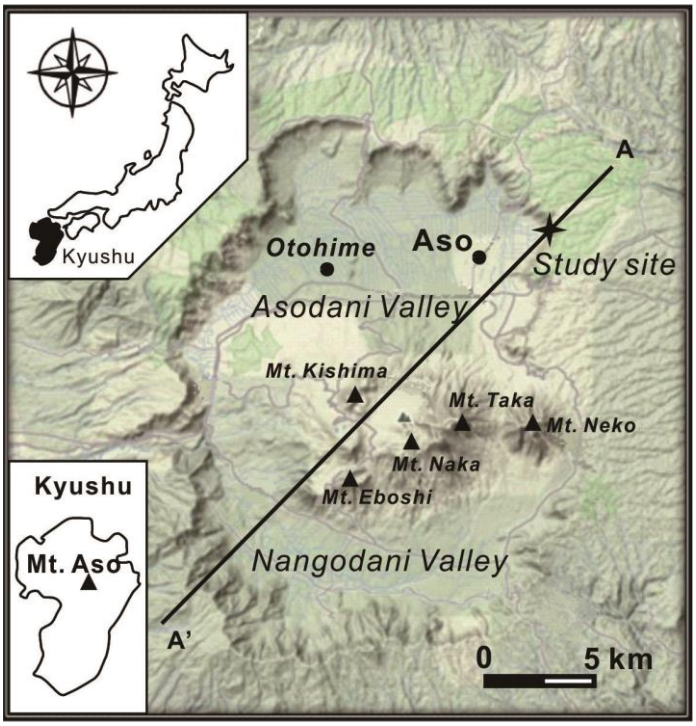

Fig. 4.2 Location map of the study site (modified from Google Earth)

4.2 Geological condition

The study site is located at Ichinomiya (Kumamoto Perfecture) in the northeast of Aso caldera (Fig. 4.2). Aso caldera extends some 17 km from east to west, and 25 km from north to south, with an area of about 350 km^2. The central crater group is referred to as Mt. Aso, and incorporates five peaks (Mt. Taka, Mt. Naka, Mt. Eboshi, Mt. Kishima and Mt. Neko). The caldera was created by four major eruptive events, known as Aso-1, Aso-2, Aso-3 and Aso-4 (Table 4.1). Huge volumes of basaltic to rhyolitic lavas and pyroclastic fall and flow deposits are distributed around the rim of the caldera (Hunter, 1998). The Aso-4 eruption, the latest and largest eruption, produced multiple pyroclastic flows. The pyroclastic flows flowed into valleys and formed pyroclastic-flow plateaus. Eruptions between each of the four major pyroclastic flow

units produced numerous tephra ash-fall layers (Miyabuchi and Sugiyama, 2011). At the study site, the geological units present include pyroclastic flow and ash fall deposits derived from the Aso-1, Aso-2, Aso-3 and Aso-4 eruptions. Gravels, sands and muds were deposited at the toe of the slope. Extensive air-fall volcanic ash covered the top of the slope at the outside rim of Aso caldera (Fig. 4.3).

The cross section of Aso caldera shows that the central cones divide the caldera into the Asodani and Nangodani valleys (Figs. 4.2 and 4.4). The mountain chain and plains surround the outer rim of the caldera, and extend to the outer side into a gentle terrain overlain by pyroclastic deposits. Most of the rainfall-induced shallow landslides generated in July 2012 occurred on the inner slope of the northern caldera wall. The study site is located on the slope of the caldera wall at an elevation of about 700 m a.s.l., and has a slope angle of more than 30° (Fig. 4.4).

Table 4.1 Characteristics of the four major eruptive events (Aso-1, Aso-2, Aso-3 and Aso-4) (Aramaki, 1984; Hunter, 1998)

Unit	Volume (km^3)	Eruptive age (ka)	Source and dominant geological units
Aso-1	>30	370-270	Welded tuff
Aso-2	>25	170	Welded tuff, in part non-welded deposit of scoria
Aso-3	>40	100	Vitric ash, pumice or scoria and welded tuff
Aso-4	>80	80	Non-welded deposit of vitric ash fall and pumice

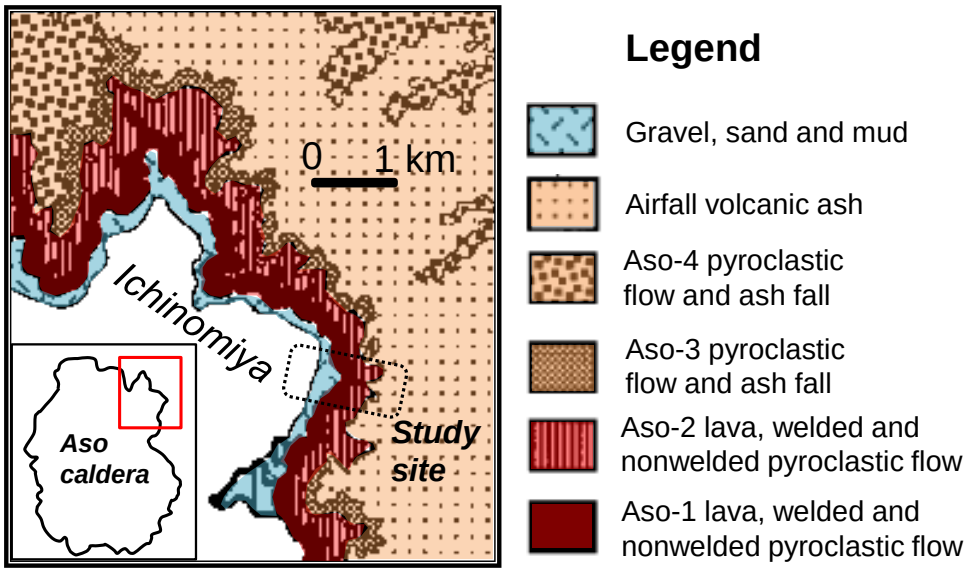

Fig. 4.3 Geological map of the study site (after Hunter, 1998)

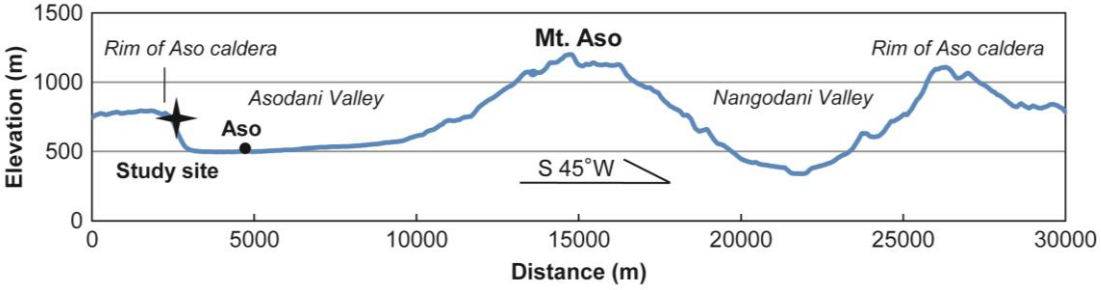

Fig. 4.4 Cross section of Aso caldera

4.3 Heavy rainfall

Due to stagnation of the wet front during the rainy season, torrential rain fell on the northern Kyushu area (Fukuoka, Kumamoto, Oita and Saga Prefectures) from 11 to 14 July, 2012 (Fig. 4.5). This event was officially named the '*Northern Kyushu Heavy Rainfall in July 2012*' by the Japan Meteorological Agency (JMA). Based on hourly rainfall data collected from all meteorological observatories in Northern Kyushu over the last decade, the maximum hourly rainfall recorded at seven observatories in July 2012 was the highest local rainfall ever recorded in the area. Among these observatories, cumulative rainfall recorded over the four-day period exceeded 500 mm at five sites, with totals ranging from 570.5 to 816.5 mm (Table 4.2).

Table 4.2 Daily and cumulative rainfall (more than 500 mm) from 11 to 14 July 2012

Rank	Prefecture	Municipality	Meteorological Observatory	Rainfall (mm)				
				July 11	July 12	July 13	July 14	Total
1	Kumamoto	Aso	Otohime	15.0	493.0	148.0	160.5	816.5
2	Oita	Hita	Tsubakigahana	44.0	99.5	144.5	368.5	656.5
3	Fukuoka	Yame	Kurogi	87.5	27.0	119.5	415.0	649.0
4	Fukuoka	Kurume	Minousan	115.0	23.0	232.0	232.0	602.0
5	Kumamoto	Minamiaso	Asosan	9.5	383.5	93.5	84.0	570.5

Most of the shallow landslides occurred on 11 and 12 July, 2012. In order to understand the rainfall characteristics at study site, hourly and cumulative rainfall data for these days was obtained from the rainfall record at the Otohime Meteorological Observatory. The Otohime Meteorological Observatory is located about 10 km west of the study site (Fig. 4.2), and is the nearest available record. The rainfall data shows that

the maximum hourly rainfall was 108 mm in the early morning of 12 July, and the cumulative rainfall over the two days was 508 mm (Fig. 4.6). This rainfall is the highest recorded at the Otohime Meteorological Observatory over the last decade. Obviously, heavy rainfall was the main triggering factor for this geo-disaster.

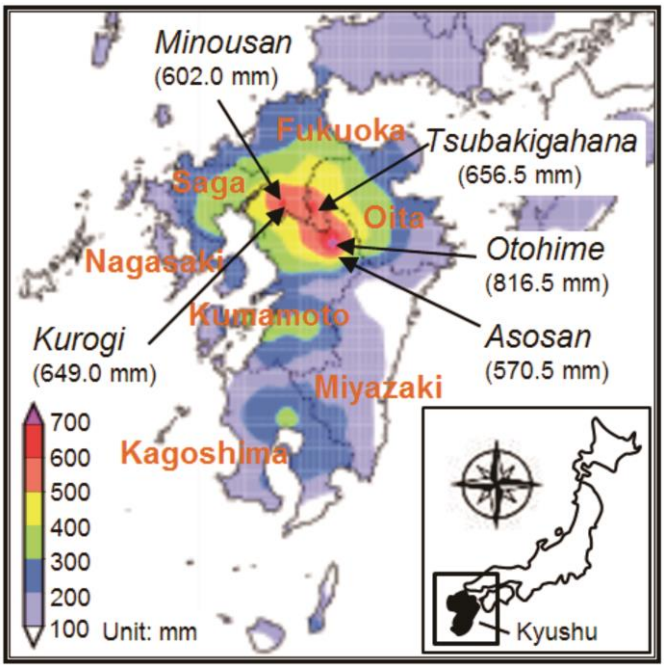

Fig. 4.5 Cumulative rainfall from 11 to 14 July 2012 (modified from JMA)

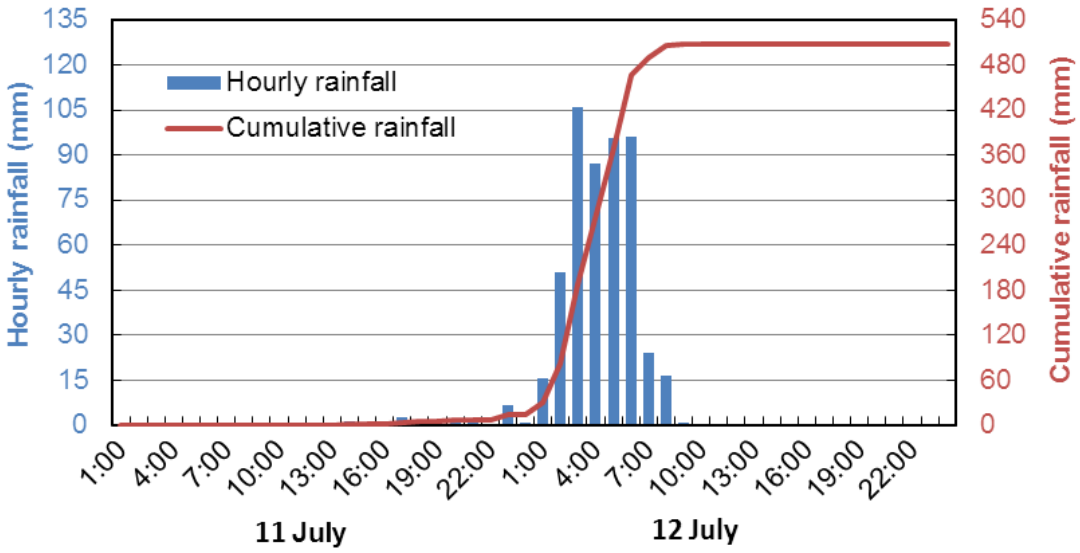

Fig. 4.6 Hourly and cumulative rainfall at study area on 11 and 12 July, 2012

4.4 Field investigation

A representative shallow landslide at Shioi Village in Ichinomiya, Kumamoto Prefecture (Fig. 4.2) was selected to study the triggering mechanism of shallow landslides on the steep slopes during heavy rainfall. Figure 4.7 shows the slope after failure. Several shallow landslides occurred in grassland at the rim of Aso caldera (Fig. 4.8). These shallow landslides were the source of debris flows in the gully. Field investigations were conducted on the shallow landslide shown in Fig. 4.8(b). Longitudinal profiles were measured to illustrate the terrain of the gully and slope. Soil samples were collected from the main scarp of the shallow landslide for laboratory investigations. Three portable dynamic cone penetration tests were conducted to determine the thickness of the soil layer. In order to measure the hydraulic coefficient of the soil, in-situ infiltration tests were conducted in hand-drilled boreholes of varying depth, above the top of the main scarp of the shallow landslide.

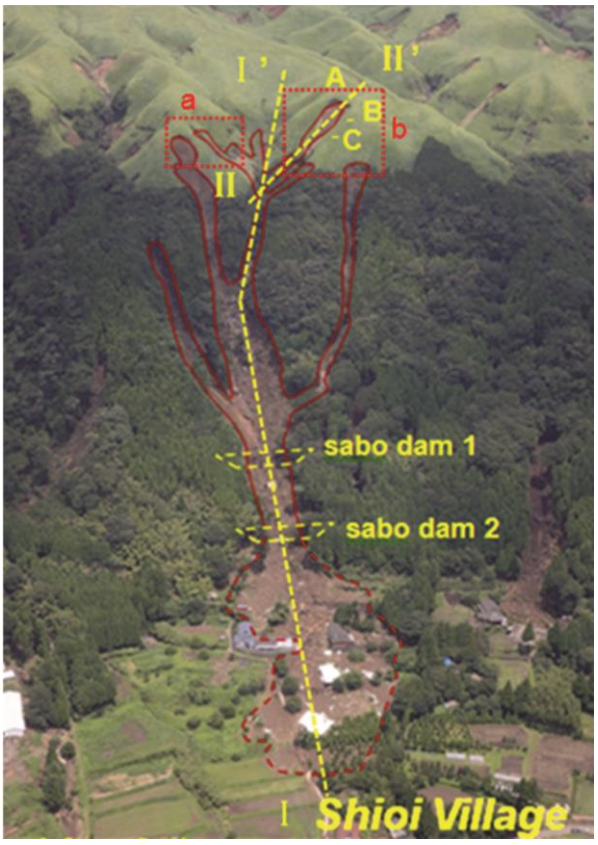

Fig. 4.7 Photograph of the slope at Shioi Village, Ichinomiya, after failure (image courtesy of Kokusai Kogyo Co., Ltd, Japan)

4.4.1 Portable dynamic cone penetration tests

The test locations are shown in Fig. 4.8 (b). During the dynamic cone penetration tests, a 5 kg hammer was dropped (free fall) from a height of 50 cm. The number of drops (N_d) was recorded for each 10 cm penetration depth of the cone tip (Qureshi et al., 2009). The thickness of the soil layer and its boundaries could thus be determined, due to the differing strength of the potential sliding bed.

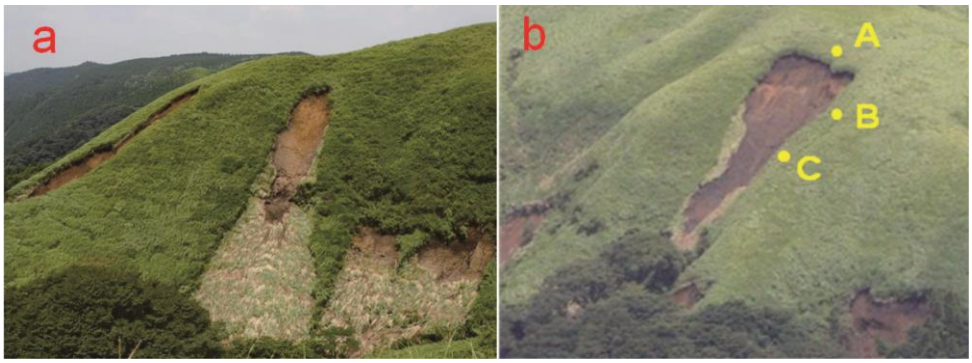

Fig. 4.8 Shallow landslides in the grassland (locations are shown in Fig. 4.7; Points A, B and C in Fig. 4.8(b) show the locations of portable dynamic cone penetration tests)

4.4.2 In-situ borehole infiltration tests

The test locations were located above the main scarp of the shallow landslide, near point A in Fig. 4.8(b). A portable twist drill was used to drill a 0.25 m deep borehole. A PVC tube was then inserted into the borehole until the bottom was reached. The tube was then filled with water, and the initial water level and start time of water infiltration were noted. The final depth of the water level was measured after a given time interval. A second borehole with a depth of 0.75 m was drilled near the first borehole (Fig. 4.9) to determine the variation of soil permeability with increased depth. The same test process was used for the second borehole. Tests were carried out twice in each borehole to obtain an average value. The hydraulic coefficient (k) was calculated using Eq. (4.1) (Lambe and Whitman, 1969);

$$k = \frac{\pi D}{1\,1\Delta t} \cdot \ln \frac{h_1}{h_2} \tag{4.1}$$

where, h_1 and h_2 are the two consecutive depths of water in meters; h_1 is the initial depth and h_2 is the final depth; D is the diameter of pipe, D = 0.1 m; and Δt expresses the time interval (in seconds) between the two successive measurements.

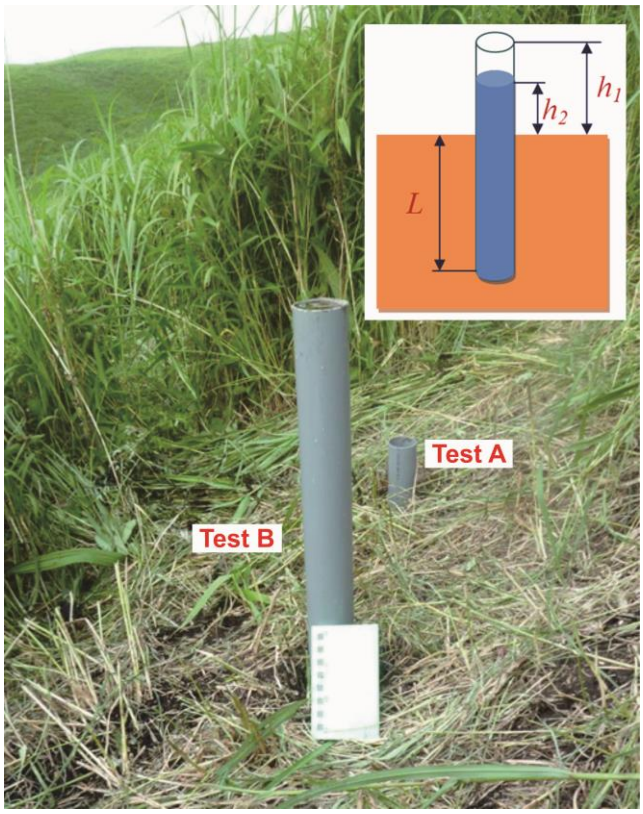

Fig. 4.9 In-situ infiltration tests

4.5 Results and discussion

4.5.1 Characteristics of slope and debris flow

The slopes at the rims of caldera are usually formed by the subsidence of land following volcanic eruptions. Steep gradients are a typical feature of these slopes. According to GIS analysis of the distribution of shallow landslides formed in Ichinomiya during the July 2012 heavy rainfall event, landslide frequency is greatest at slope angles between 30 and 40° (Geographical Survey and Photography, Japan, 2012). As shown in the longitudinal profiles of the investigated area, the angle of the slope on which shallow landslide occurred is 38° (I-I' in Fig. 4.10). A steep slope (II-II' in Fig. 4.10) is also present behind the sabo dams. The steep terrain will affect both the slope

stability and hydrological conditions, such as surface runoff on the slope and seepage in the soil layer. In addition, the steep slope enhances the rapid down-slope movement of debris. Erosion from the debris flows removed the thin soil layer in the gully, leaving bedrock exposed (Fig. 4.11). The speed of the debris flows increased rapidly as they traveled down the steep slope. The debris flows contained blocks of rock, and destroyed two sabo dams (Fig. 4.12) and several houses. Finally, debris was deposited on the flat land and paddy fields at the base of the slope.

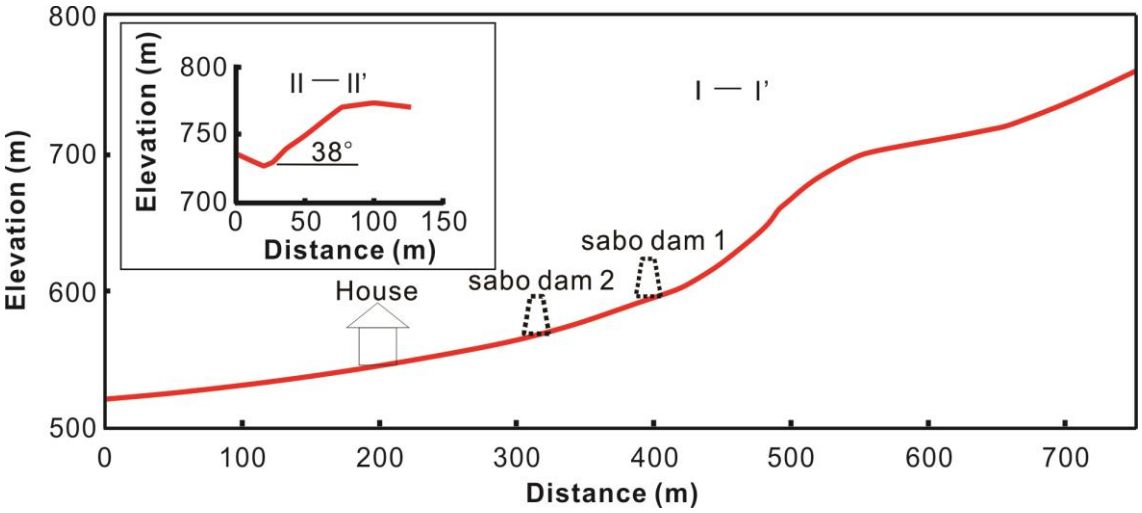

Fig. 4.10 Longitudinal profiles of the gully and slope

Fig. 4.11 Exposed bedrock in gullies

Fig. 4.12 Sabo dams destroyed by debris flow

The results of the portable dynamic cone penetration tests show that the soil layer is about 3.5 m thick at the upper slope (Fig. 4.13). The soil layers gradually become thinner (about 1 m) from the upper to the lower slope. In general, soils in the lower parts of hillsides are thicker than in their upper part, due to soil erosion in the upper parts, and deposition in the lower parts. Consequently, the characteristics of the slope at the rim of Aso caldera differ from the general condition. This may be because that erosion on the lower slope is more severe than on the upper slope due to surface run-off during heavy rainfall. Moreover, the slope is quite steep (about 38°). Soil eroded from the upper slope will not be deposited in the lower part. Instead, fine soil particles will be deposited in the gully, and this material will be transformed into debris flows during heavy rainfall.

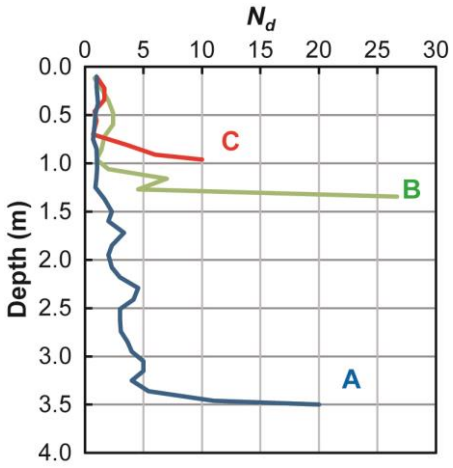

Fig. 4.13 Result of three portable dynamic cone penetration tests

4.5.2 Physical properties of soils

The soil in the main scarp of the shallow landslide can be divided into two layers based on the appearance features (Fig. 4.14). Layer 1, the black uppermost layer, is composed of volcanic ash, humus and plant roots. Coarse sand and gravels occur in the underlying layer 2. Particle size gradually increases downward, reaching maximum particle diameter of about 20 mm. The sliding zone of the shallow landslide is located at the base of layer 2, which is underlain by a basal gravel layer. Sliding surfaces were observed on the surface of basal gravel layer. Grain size analysis (sieve and hydrometer analysis) of soil samples from each layer was conducted to determine their grain size distribution (Fig. 4.15). Fine particles (grain size less than 0.075 mm) form around 45% of the soils in layers 1 and 2. After the occurrence of shallow landslides, on steep slopes these fine materials can easily transform into debris flows during heavy rainfall. According to the Unified Soil Classification System (USCS), layer 1 is composed of poorly graded tephra clay. Layer 2 is composed of clay with coarse sand gravels.

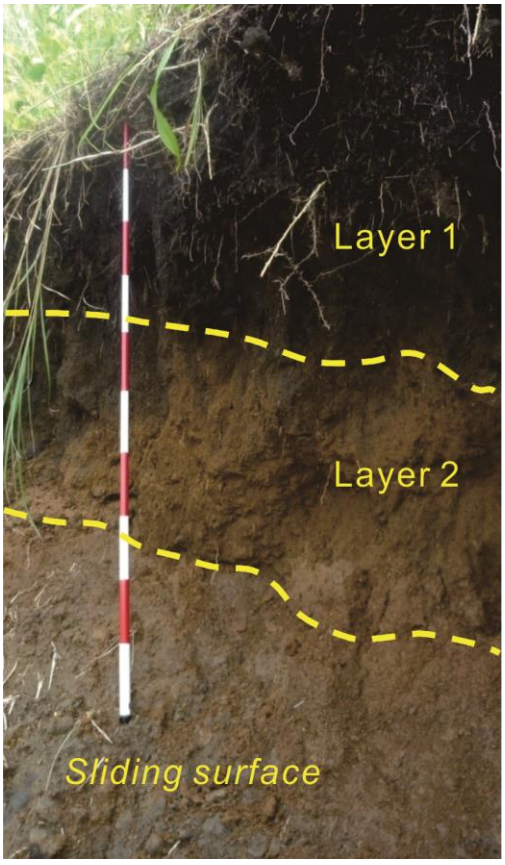

Fig. 4.14 Main scarp of the shallow landslide

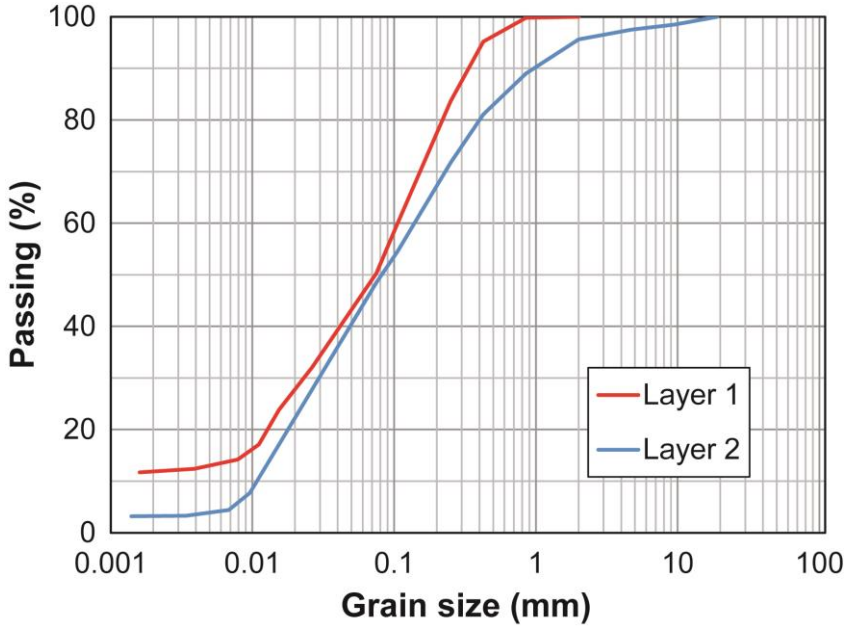

Fig. 4.15 Grain size distributions of soil samples from different layers

The soil properties of the different layers are shown in Table 4.3, which summarizes specific gravity, natural water content, void ratio, degree of saturation, total and saturated unit weight. Although, there had been no rainfall for several days before sampling, soil layer 1 maintained a high water content and degree of saturation. This indicates that soil layer 1 has high water retention capability. The unit weight of the topsoil increased about 20% from natural to saturated condition. These phenomena are related to the properties of soil, such as higher void ratio. High void ratio (5.452) means that soil layer 1 has a loose structure. Internal erosion could easily occur in such a loose soil layer, with high pore-water pressure or seepage.

Table 4.3 Physical properties of different layers of soil

Physical properties	**Layer 1**	**Layer 2**
Specific gravity, G_S	2.271	2.734
Water content, w (%)	187.0	72.0
Void ratio, e	5.452	2.191
Degree of saturation, S (%)	78	90
Total unit weight, γ (kN/m^3)	10.1	14.7
Saturated unit weight, γ_{sat} (kN/m^3)	12.0	15.4

4.5.3 Rainfall infiltration

As noted above, heavy rainfall is the main triggering factor for the shallow landslide occurrences at the study site. The results of in-situ infiltration tests are shown in Table 4.4. Hydraulic conductivity (k) is 1.28×10^{-6} m/s at the shallow depth of 0.25 m, compared to 1.90×10^{-7} m/s at 0.75 m depth. The soil at the bottom of the hand-drilled boreholes should be compressed and disturbed, and hence the actual hydraulic conductivity should be higher than the experimental value. Nevertheless, these results show that permeability decreases with increase in depth. Paudel et al. (2008) measured the hydraulic conductivity of soils on slope surfaces at ten sites in Aso caldera. They also found that the hydraulic conductivity of soil layer was low, ranging from 1.0×10^{-6} to 5.0×10^{-6} m/s. With the low hydraulic conductivity of the soil layer, during heavy rainfall events most rainfall will transform into surface runoff.

Table 4.4 Results of the in-situ permeability tests

Parameters	**Test A**		**Test B**	
	1	**2**	**1**	**2**
h_1 (m)	0.15	0.15	0.60	0.60
h_2 (m)	0.14	0.12	0.59	0.58
L (m)	0.25	0.25	0.75	0.75
Δt (s)	1500	5100	2700	4800
k (m/s)	1.31×10^{-6}	1.25×10^{-6}	1.78×10^{-7}	2.02×10^{-7}
Average k (m/s)	1.28×10^{-6}		1.90×10^{-7}	

4.5.4 Shear strength of soil

The stress-strain relationship of the consolidated-undrained tests on the saturated specimens (Fig. 4.16a) shows that the deviatoric stress increases with the axial strain. The stress-strain curves provide evidence for stress hardening. When the shear strain is over about 13%, the deviatoric stress begins to flatten. For the specimen with high confining pressure (100 kPa), stress softening was observed at the end of the test. Critical state was reached for all three tests with a high axial strain (Fig. 4.16a).

The relationship between excess pore-water pressure and the axial strain of consolidated-undrained tests on the saturated specimens is shown in Fig. 4.16b. Positive pore-water pressure was recorded in all three undrained tests. In all soil specimens, pore-water pressure increased to a peak at low strain (about 3%), declines from its

maximum value as the strain increases continuously, and finally reached a minimum value at the end of the tests. The initial buildup of the pore-water pressure suggests that the specimens exhibit contractive behavior. The reduction in the pore-water pressure after the peak indicates that the specimens change from contractive to dilative behavior during shear, as illustrated by the effective stress paths shown in Fig. 4.17.

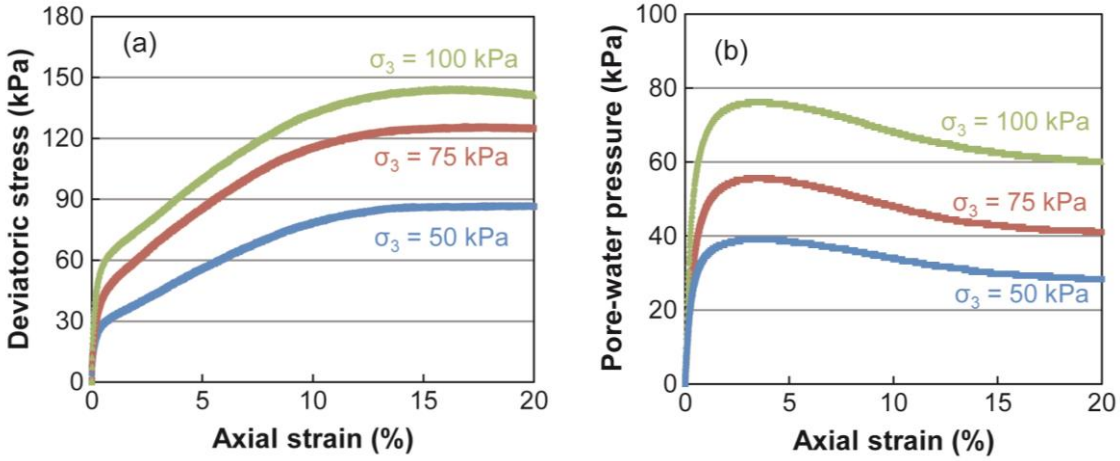

Fig. 4.16 (a) stress-strain relationship; (b) relationship between pore-water pressure and axial strain for the consolidated-undrained triaxial compression tests

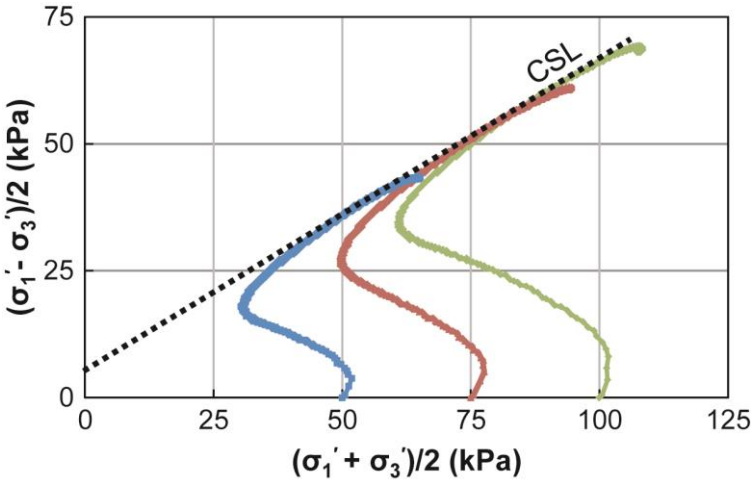

Fig. 4.17 Effective stress paths under different confining pressures (50, 75 and 100 kPa). The dotted line indicates the critical state line (CLS).

All the effective stress paths show a similar trend. Each path moves toward the right initially (increasing $(\sigma_1' + \sigma_3')/2$), and then moves to the left (decreasing $(\sigma_1' + \sigma_3')/2$) until reaching a turning point, after which they turn right, before reaching the critical state line (CSL) at the end of the test. The critical states of saturated specimens can be represented by the CSL in the stress plane. The gradient of the critical state line is 0.6, which corresponds to a critical state angle of effective friction of 36.9° and cohesion of 6.3 kPa. In published results of soil shear strength, it was observed that the effective friction angle was about 35°, and cohesion varied between different soil layers (Paudel et al., 2008). The high shear strength of these soils explains why the steep slopes on the northeastern rim of Aso caldera are usually stable under normal rainfall during the rainy season.

4.5.5 Soil behavior with the increase in pore-water pressure

The relationships between deviatoric stress, axial strain and pore-water pressure were obtained through the pore-water pressure controlled triaxial test (Fig. 4.18). The results show that when the pore-water pressure increased to about 12 kPa, the deviatoric stress started to decrease, while the axial strain increased. With the continuous increase in pore-water pressure, the major failure of the soil occurred when the pore-water pressure increased to near 15 kPa. At this time, high excess pore-water pressure was generated in the soil, causing the obvious decrease of effective stress. In a short time, the axial strain increased rapidly, and exceeded 20%. This soil behavior in response to the increase in pore-water pressure can explain the initiation mechanism of the shallow landslides on the slopes. During heavy rainfall, continuous rainfall infiltration can generate a wet front in the soil layer, and in turn forms a saturated zone above the potential sliding surface. The saturated zone will move gradually upwards in relation to the slope surface, and the pore-water pressure acting on the potential sliding surface will increase. Based on our results, it is evident that failure in the soil specimen will not occur, even with high pore-water pressure (less than 12 kPa). It also means that the slope can maintain stability when the rainfall is not so heavy. However, if the pore-water pressure exceeds the critical value as a result of heavy rainfall, a shallow landslide will be triggered.

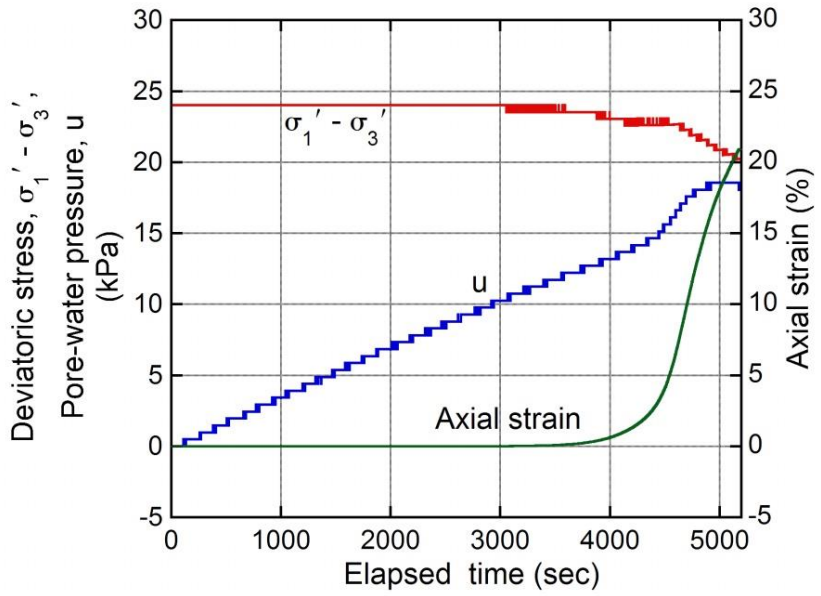

Fig. 4.18 Relationships between deviatoric stress, axial strain and pore-water pressure for the pore-water pressure controlled triaxial test

4.5.6 Probable triggering mechanism

Based on the above discussion of the characteristics of the slope, physical properties of the soil, rainfall infiltration, shear strength of the soil, and soil behavior with the increase in pore-water pressure, a probable triggering mechanism for shallow landslides on steep slopes was developed, as shown in Fig. 4.19.

(1) During heavy rainfall, surface water infiltrates into the soil layer and generates water level in the slope. The soil layer in the lower part will become fully saturated first because the thickness of the soil layer at the toe of slope is very low.

(2) Due to the limitation imposed by the hydraulic conductivity (*k*) of the soil, infiltration rate of rainfall is far less than the rainfall intensity. Most of the rainfall transforms into surface runoff. On the steep slope, high-speed surface runoff will remove the toe of the slope.

(3) Gradual headward erosion may occur, and remove the soil layer in the lower part that provides the resistance for slope stability. Meanwhile, the groundwater level in the slope keeps increasing due the continuous rainfall infiltration, i.e., the pore-water pressure in the soil builds up at the potential sliding surface. When the pore-water pressure exceeds the critical value, a shallow landslide will be triggered, as a result of heavy rainfall.

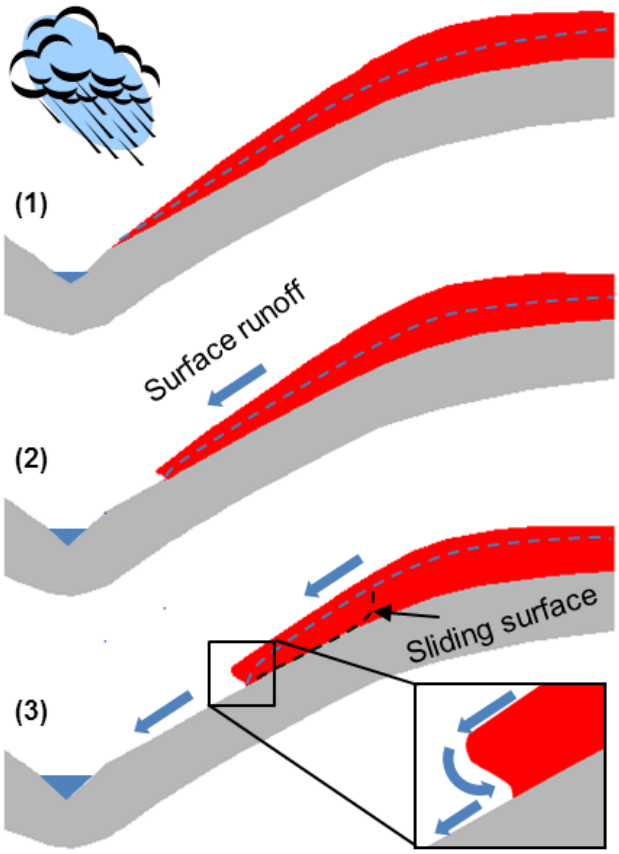

Fig. 4.19 Probable triggering mechanism of shallow landslides on the northeastern rim of Aso caldera

4.6 Conclusions

1. High-intensity rainfall is the main triggering factor for shallow landslides on the northeastern rim of Aso caldera. On these steep slopes, the sliding mass created after the occurrence of shallow landslides is transformed into debris flows during heavy rainfall.
2. The soil on the slopes on the northeastern rim of Aso caldera has high shear strength. The soil behavior in response to increased pore-water pressure shows that failure of the soil will not occur until the pore-water pressure exceeds a relatively high value. This explains why such steep slopes can be stable under normal rainfall during the rainy season. However, if the pore-water pressure exceeds the critical value as a result of heavy rainfall, shallow landslides will be triggered.

3. The probable triggering mechanism indicates that the initial failure process of the shallow landslides on the northeastern rim of Aso caldera begins with toe erosion caused by surface runoff. The combination of this loss of resistance force at the toe of the slope and increase in pore-water pressure in the slope during heavy rainfall will finally bring the slope to a critical condition.

CHAPTER 5

RAINFALL-INDUCED SHALLOW LANDSLIDES IN IZU OSHIMA ISLAND, JAPAN, IN 2013

5.1 Introduction

Typhoon Wipha passed the Izu Islands on 16 October 2013. These islands are located at the southeast of the Izu Peninsula, Japan (Fig. 5.1). Most regions on the typhoon track, especially the Izu Oshima Island, suffered heavy rainfall. It triggered widespread shallow landslides on the western slopes of Izu Oshima Island (Fig. 5.2). Pyroclastic-fall deposits mixed with branches and trunks flowed downslope along gullies and drainage channels. High speed debris flows flooded the settlement of Motomachi, which is situated at the toe of the slopes. This disaster caused serious loss of life and property damage. According to the damage report, 35 people were killed, four people remain missing, 73 houses were completely destroyed, and 129 houses were damaged (Ministry of Land Infrastructure and Transport and Japan, 2013).

Several researchers and organizations carried out field investigations after this geo-disaster event (Sakurai and Disaster Research Team of Kanto Branch, 2014; Ikeya, 2014; Disaster Prevention Division of Tokyo Metropolitan Government (TMG), 2014). Their investigation reports describe the occurrences of the landslides, and the damage caused by the debris flows. These studies provide key background information for further research. Authors had conducted both field investigations and laboratory

experiments in an effort to understand the initiation mechanism of shallow landslides triggered by heavy rainfall during Typhoon Wipha. Consolidated-undrained triaxial tests were conducted to determine the effective soil strength. This paper also presents the results of triaxial tests with pore-water pressure control, which were conducted to simulate the initiation mechanism of the shallow landslides on the upper slopes due to rainfall infiltration.

Fig. 5.1 Location of Izu Oshima Island. Inset is the track of Typhoon Wipha.

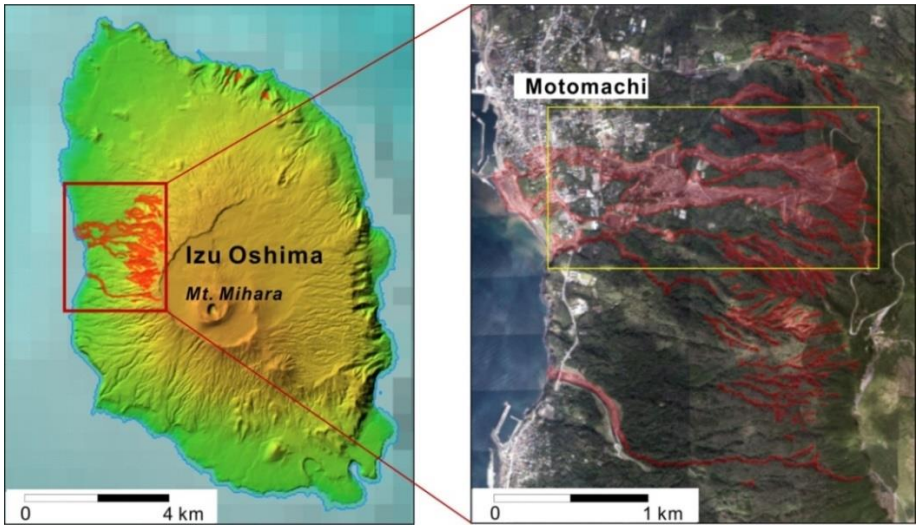

Fig. 5.2 Landslides in the west of Izu Oshima Island (red areas indicate the landslide distribution, modified from Geospatial Information Authority of Japan, 2013)

5.2 Geological condition

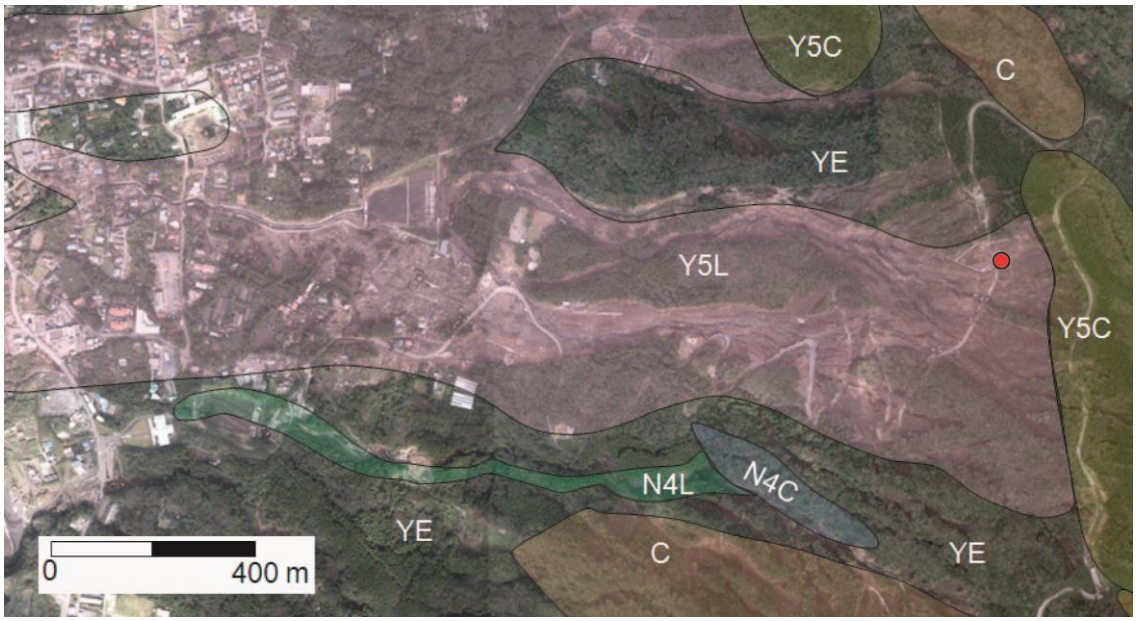

Fig. 5.3 Geological map of main landslide area (modified from Kawanabe, 1998; photograph from the Geospatial Information Authority of Japan)
Y5L: Basalt (Syn- and post-caldera volcano, 1338?);
Y5C: Basalt scoria and spatter (Syn- and post-caldera volcano, 1338?);
N4L: Basalt (Syn- and post-caldera volcano, 8th Century);
N4C: Basalt scoria (Syn- and post-caldera volcano, 8th Century);
C: Basalt scoria (Pre-caldera volcano);
YE: Pyroclastic-fall deposits (Pre-caldera volcano).

Izu Oshima Island is a volcanic island. This active volcano consists of pre-caldera, syn-caldera and post-caldera volcanoes (Kawanabe, 1998). Many hazardous eruptions have occurred in the past. The ejecta in each stage were mostly coarse-grained pyroclastic materials, with basaltic lava flows and pyroclastic-fall deposits. Younger deposits and lava flows covered the deposits and lava flows from the older volcano stage. This type of volcanic activity led to the formation of resistant lava flows interbedded with poorly consolidated pyroclastic-fall deposits. Fig. 5.3 shows the geological map of the main landslide area, which is outlined in Fig. 5.2 (right) with a yellow frame. Most of the shallow landslides which were the source of the debris flows

occurred within the distribution of basalt (Y5L). Pyroclastic-fall deposits overlie the basalt (Y5L) in the section which is exposed in the upper slope along the road (Fig. 5.4). This type of structure with interbedded resistant basalt and weak pyroclastic deposits can easily cause landslides. Moreover, the interface between these two layers tends to be a confining boundary for groundwater passing through the upper soft and porous pyroclastic-fall deposits.

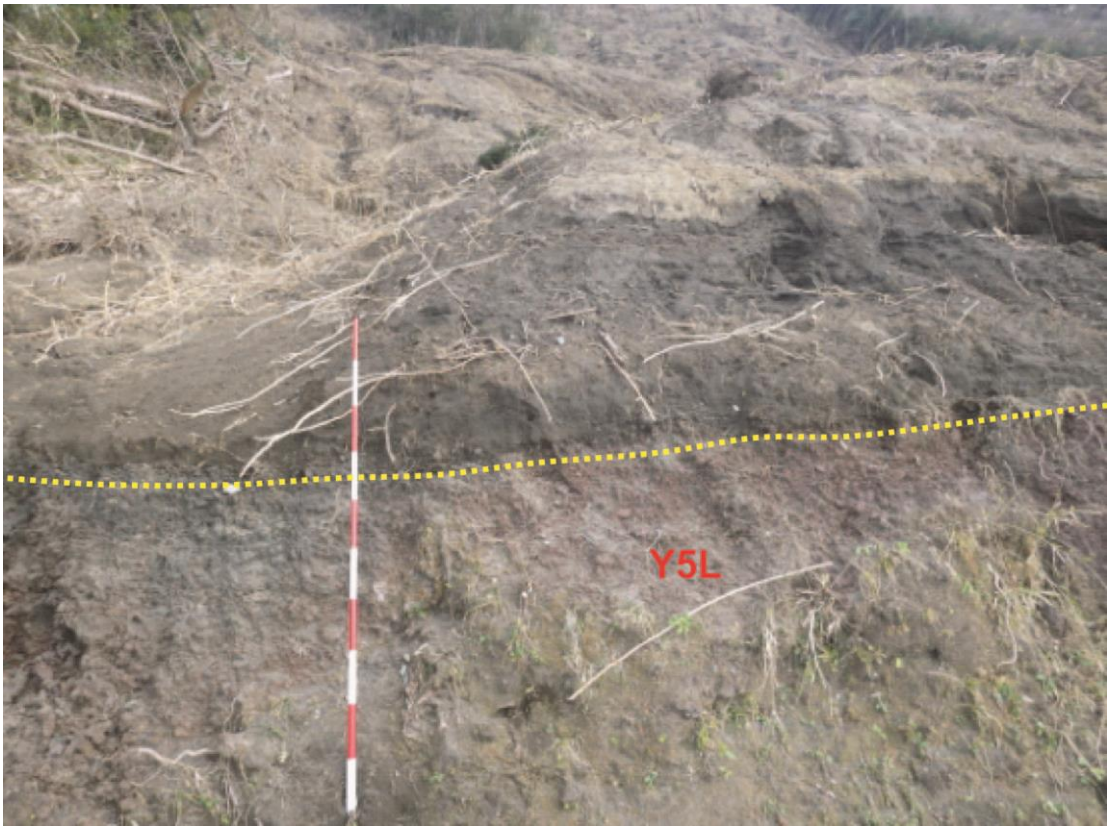

Fig. 5.4 Basalt (Y5L) overlain by pyroclastic-fall deposits (at red spot in Fig. 5.3)

The topography of Izu Oshima Island is typical of a volcanic island. The outline of the island is oval, elongated in the NNW-SSE direction, with a length of about 15 km, and width of about 9 km (Kawanabe, 1998). The central part of the island has the highest elevation due to volcano eruption. The highest point is Mt. Mihara (764 m a.s.l.), and the terrain becomes gentler towards the coast. Sea cliffs up to 350 m high are developed from the north to the east, and in the southwest of the island, due to wave

erosion. The highest cliff is found on the east coast. Relatively flat land in the northwest of the island was planned as a residential area. A caldera with a diameter of about 4 km is present at the summit of the volcano, but in the east its wall is buried by younger lava. On the west side, the caldera wall is clearly defined. In addition, the slopes of the outer rim of the western caldera wall are quite steep (Fig. 5.5). Most of the shallow landsides occurred on the steep slopes.

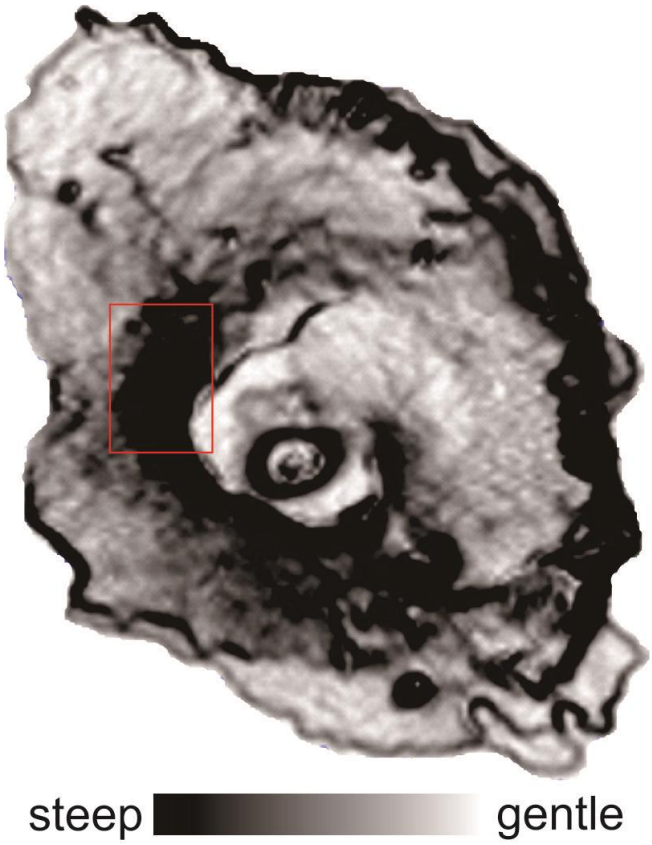

Fig. 5.5 Slope terrains on Izu Oshima. Red frame shows the main landslide area.

5.3 Heavy rainfall

The main triggering factor of these shallow landslides was the short-period downpour of heavy rainfall. On the early morning of October 16, Typhoon Wipha was close to the Izu Islands (Fig. 5.1). As Typhoon Wipha approached, the northern Izu Islands suffered heavy rainfall, especially Izu Oshima Island. Records from the

meteorological station at Motomachi in the Izu Oshima show the maximum one-hour rainfall was about 118.5 mm. The maximum 24-hour cumulative rainfall was more than 824 mm (Fig. 5.6). This was 2.5 times the average monthly rainfall for October in Izu Oshima (Tokyo District Meteorological Observatory (TDMO), 2013).

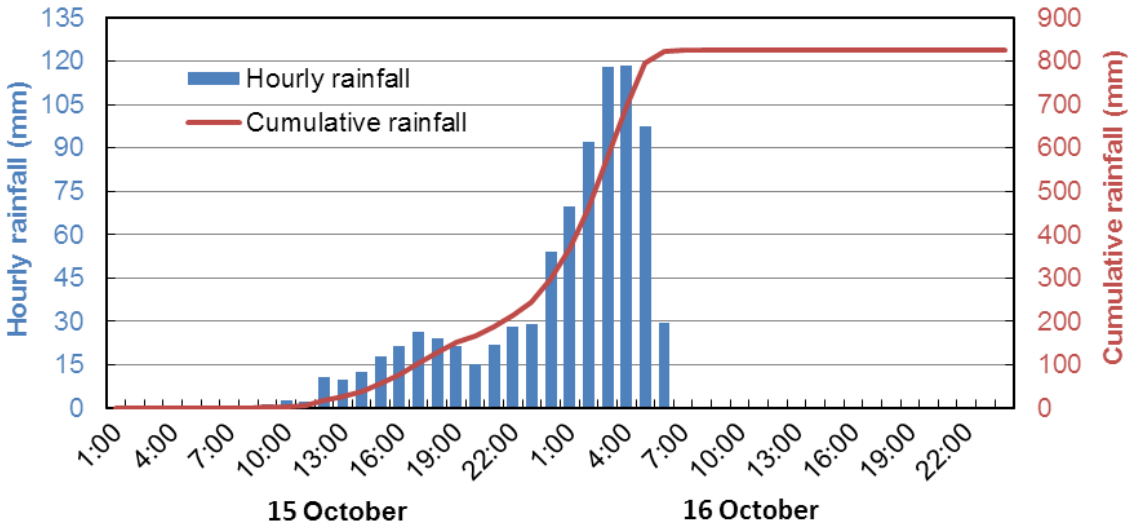

Fig. 5.6 Hourly and cumulative rainfall in Izu Oshima on 15 and 16 October 2013

5.4 Field investigation

Fig. 5.7 shows a plan view of the areas that were impacted by debris flows. According to the information from local residents and seismic data, shallow landslides (light blue area) occurred on the upper slopes in the early morning (Ikeya, 2014). Pyroclastic-fall deposits mixed with branches and trunks flowed downslope along the gullies (beige arrows). Debris flow flushed away the surface soil and vegetation along the gullies (gullies A and B in Fig. 5.7). Because no drainage channels were present, the debris flow flooded the houses situated on the down slopes area (light red area), and caused serious loss of lives and properties. The sabo dam 1, which is located at the mouth of gully A, played an important role in protecting this area. It effectively reduced the speed of the debris flow, and captured branches and trunks. Furthermore,

fine-grained particles were easily drained out through the drainage channel (brown arrow) (P2 in Fig. 5.8). Finally, this fine material flowed into the ocean and was deposited at the coast (P3 in Fig. 5.8). Sabo dam 2, situated just behind the Volcano Museum, stopped the debris from damaging the museum and nearby residential houses.

Shallow landslides on the upper slopes which were the source of debris flows were examined in the main investigation area (Fig. 5.9). Slope angle is one of the most important factors on slope instability. In the field, Laser Range Finder (LRF) was used to survey the longitudinal profile (A-A' in Fig. 5.9) of the shallow landslide selected for study. The measuring result shows that slope is with steep terrain, and slope angle is over 30 degrees (Fig. 5.10). Fig. 5.11 shows the exposed slope after the vegetation and pyroclastic-fall deposits had slide downslope. The underlying basalt lava (Y5L) was exposed in places, as shown by the arrows in Fig. 5.11.

Disturbed soil samples were collected from the pyroclastic-fall deposits layer above the basalt lava (Fig. 5.12) at location S1 to study soil properties. Sample location is shown in Fig. 5.9. Conventional laboratory experiments on the soil sample were conducted to obtain the basic parameters (grain size distribution, specific gravity, in-situ dry density and void ratio) which will be used to control the parameters of specimens for triaxial tests.

Fig. 5.7 Plan view of the main landslide area (photograph from the Geospatial Information Authority of Japan)

Fig. 5.8 Photographs after debris flows. The locations are marked on Fig. 5.7.

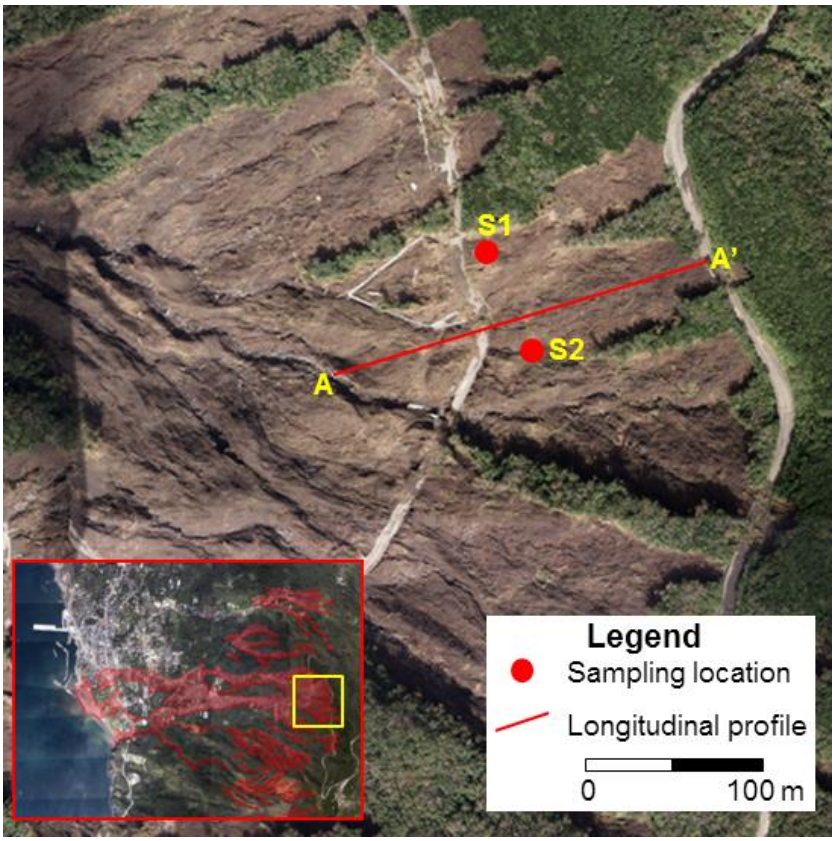

Fig. 5.9 Main investigation area of the shallow landslide on the upper slope (photographs from the Geospatial Information Authority of Japan)

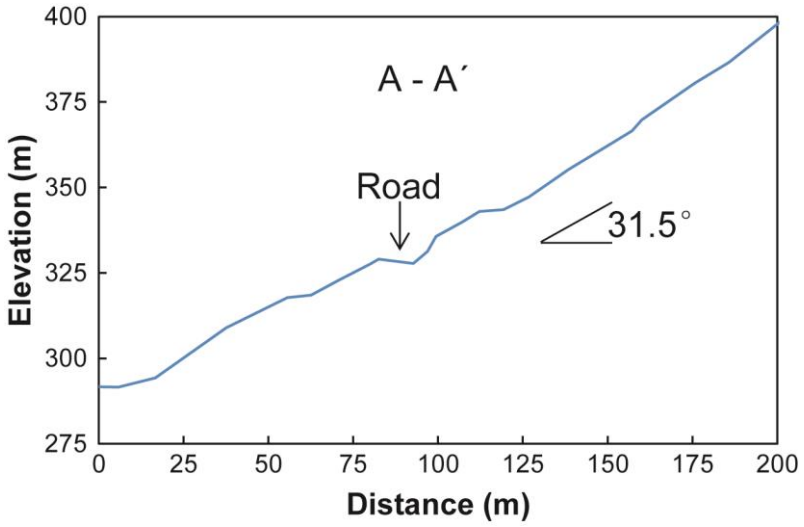

Fig. 5.10 Longitudinal profile of the selected shallow landslide

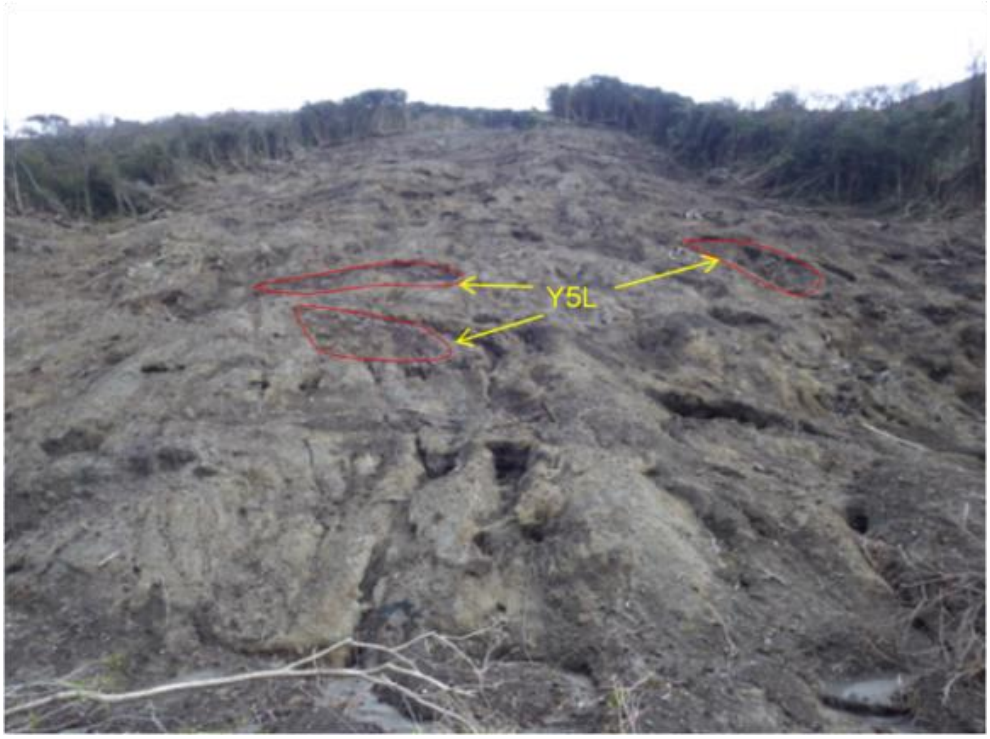

Fig. 5.11 Exposed slope after shallow landslide. Basalt (Y5L) is exposed in places.

Fig. 5.12 Sampling in the pyroclastic deposit layer (S1 in Fig. 5.9)

5.5 Results and discussion

5.5.1 Soil properties and behaviors

In the Table 5.1, it can be observed that the specific gravity and void ratio of the pyroclastic-fall deposits are 2.903 and 1.183, respectively. That shows the typical property of pyroclastic-fall deposits. These soil properties will affect the mechanical and hydraulic characteristics of soil. Grain size distribution of sample shows that the soil is well-graded fine sand with silt (ASTM D2487-06, 2006) (Fig. 5.13). After the occurrence of shallow landslides, these fine materials on steep slope can easily transform into debris flow during heavy rainfall.

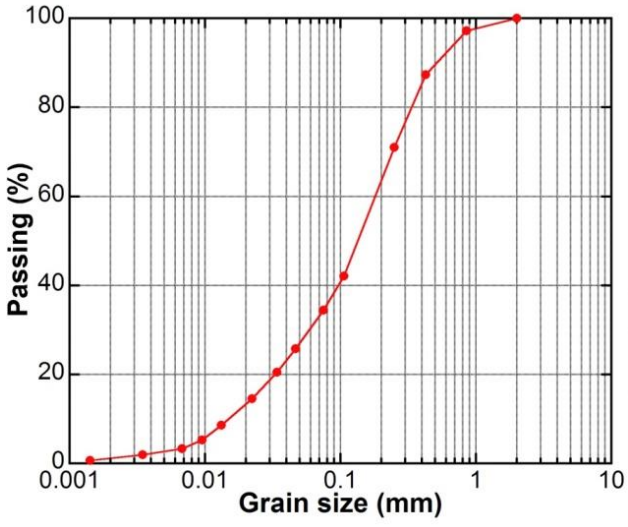

Fig. 5.13 Grain size distribution of soil sample

Table 5.1 Soil parameters

Parameters	**Value**
Specific gravity, G_S	2.903
Coefficient of uniformity, C_u	12.188
Coefficient of curvature, C_c	1.154
Mean grain size, D_{50} (mm)	0.143
Dry density, ρ_d (kg/m^3)	1,330
Void ratio, e	1.183

The stress-strain relationship of the consolidated-undrained tests on the saturated specimens (Fig. 5.14a) shows that the deviatoric stress increases with the axial strain. The stress-strain curves indicate the evidence of strain hardening. When the shear strain is over about 15%, the deviatoric stress begins to steady state. Critical state was reached for all four tests with a high axial strain. The relationship between the excess pore-water pressure and the axial strain of the consolidated undrained tests on the saturated specimens is shown in Fig. 5.14b. Positive excess pore-water pressure was recorded in all four tests. In all soil specimens, the positive excess pore-water pressure increases to a peak at low strain (about 5%), and reduces from its maximum value as the strain increases continuously, and finally reaches a plateau at the end of the tests. The initial buildup of the positive excess pore-water pressure suggests that the specimens exhibit contractive behavior. The reduction in the positive excess pore-water pressure after the peak indicates that the specimens change from contractive to dilative behavior during shear, as illustrated by the effective stress paths shown in Fig. 5.15. Ng and Chiu (2001) described the similar shear behaver of loosely compacted saturated volcanic soil under undrained conditions in their paper. All the effective stress paths show a similar trend. Each path moves toward the right-hand side initially, and then moves toward the left-hand until reaching a turning point, after which they turn right, before reaching the critical state line CSL at the end of the test. The critical states of saturated specimens can be represented by the CSL in the stress plane, as shown in Fig. 5.15. The gradient of

the critical state line is 0.625. This corresponds to a critical state angle of internal friction angle of 38.7 degrees.

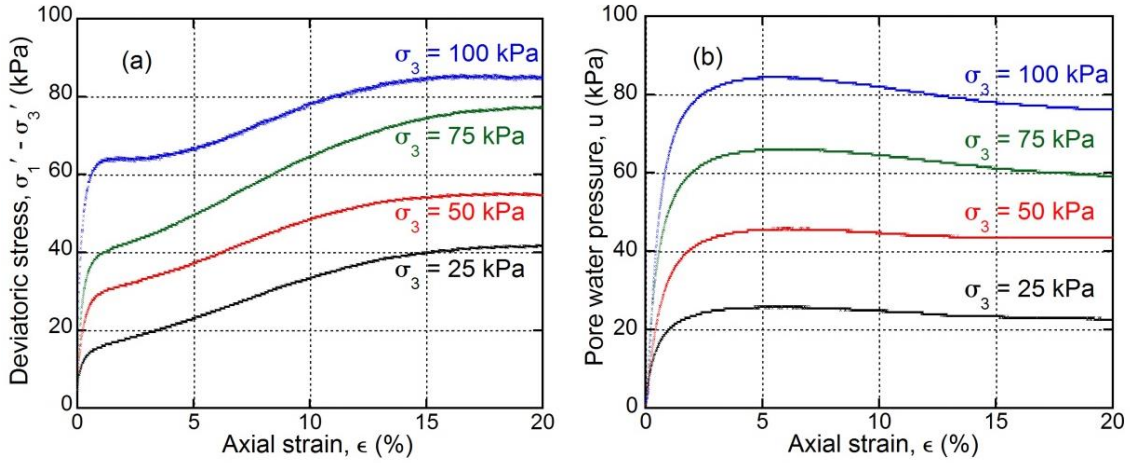

Fig. 5.14 (a) stress-strain relationship; (b) relationship between pore-water pressure and axial strain for the consolidated-undrained triaxial compression tests

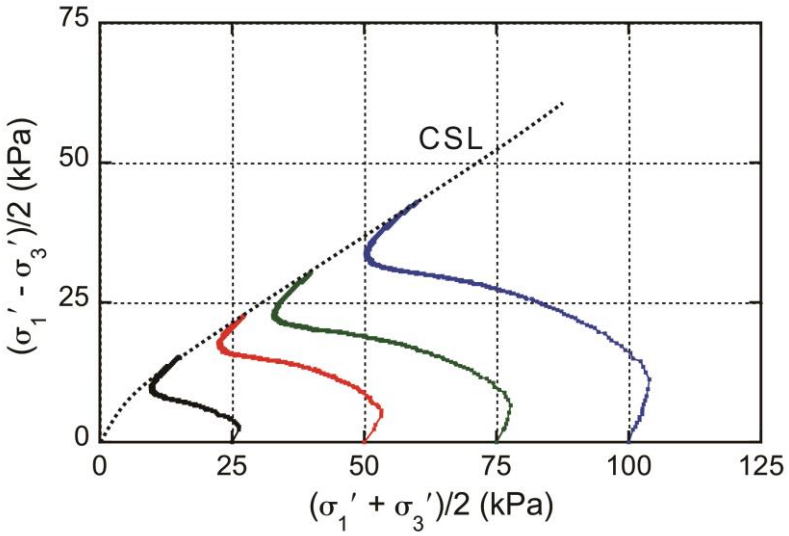

Fig. 5.15 Effective stress paths under different confining pressures (25, 50, 75 and 100 kPa); CSL – critical state line

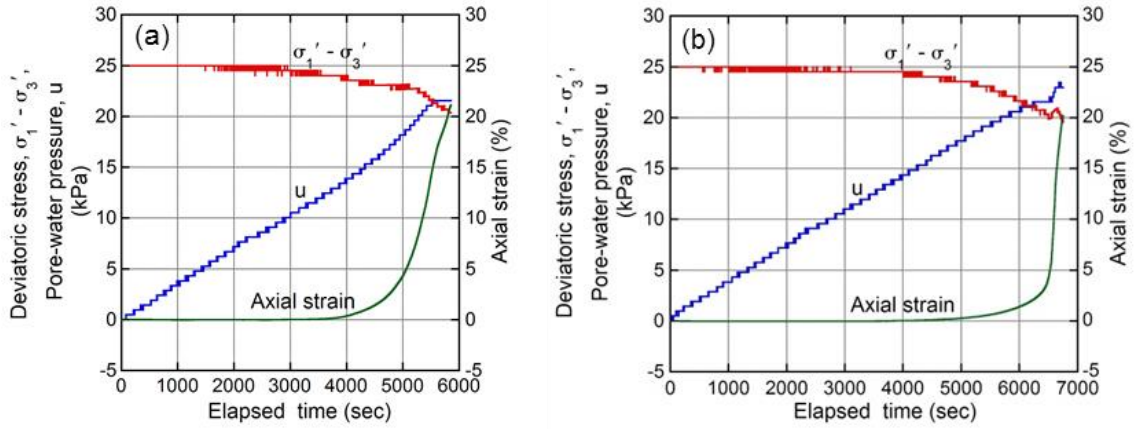

Fig. 5.16 Relationship between deviatoric stress, axial strain and pore-water pressure under (a) loose condition and (b) dense condition

The relationships between deviatoric stress, axial strain and pore-water pressure under loose and dense conditions are shown in Figs. 5.16a and b, respectively. For the soil with loose condition (initial void ratio of 1.079), effective stress starts to decrease when the pore-water pressure increases to about 8 kPa. Obvious decrease of effective stress is generated when the pore-water pressure reaches about 12 kPa. Excess pore-water pressure builds up with rapid increase of axial strain. For the dense condition (initial void ratio of 0.808), effective stress starts to decrease when pore-water pressure increases to about 13 kPa. Obvious decrease of effective stress is generated when the pore-water pressure reaches about 17 kPa. In contrast to the loose condition, the rate of increase in pore-water pressure slows with the rapid increase in axial strain. From these results, it is evident that obvious decrease of effective stress occurs in a shorter time in the soil in loose condition than it is in dense condition.

5.5.2 Two types of failure mode

Two types of failure mode can be proposed, based on the pattern of shallow landslides on the steep slopes along the road (Fig. 5.17). The first type of failure mode shows that pyroclastic-fall deposits partially mantling the upper most slopes slid first, during heavy rainfall. The soil mass then crossed the road, and drove the pyroclastic-fall

deposits lying below the subgrade, to slide downslope together. For this type of failure mode, slope cutting during road construction affects the stability of the pyroclastic-fall deposits on the upper slopes. Slope cutting without any preventive construction will result in a free boundary, and remove the resistance at the toe of slope. Therefore, the slope can easily become unstable under trigger factors such as rainfall and dynamic load.

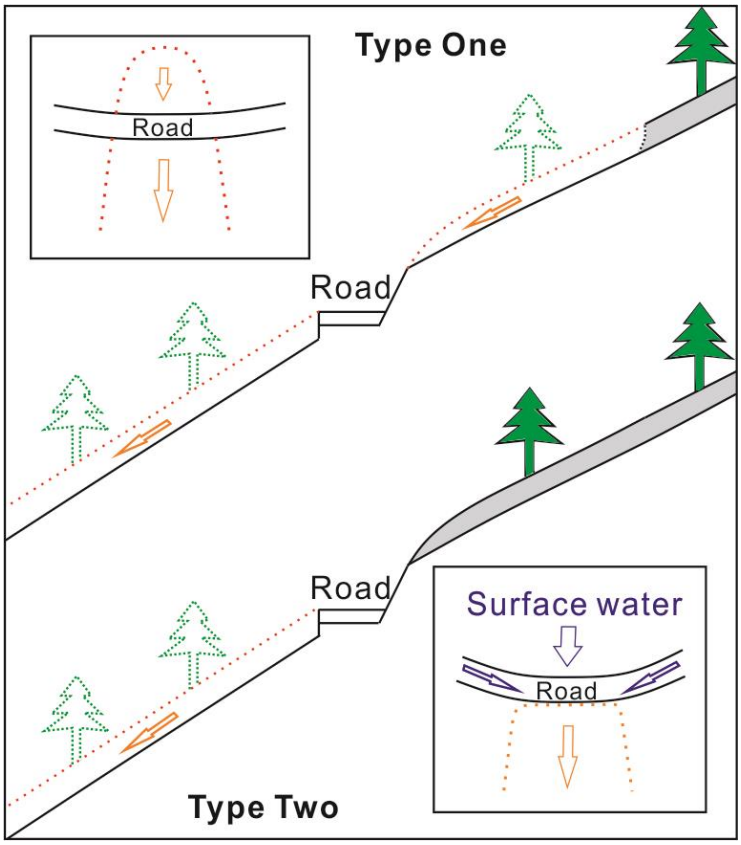

Fig. 5.17 Two types of failure mode of shallow landslides

The second type of failure mode shows that the entire pyroclastic-fall deposits below the road started to slid during heavy rainfall. The main scarp of this shallow landslide was located at the subgrade of the upper part of the road. The topographic map shows that the section of subgrade of the upper road near the main scarp was of relatively low elevation (Fig. 5.18). The lower-lying and winding road surface will

collect surface water during heavy rainfall. Subsequently, runoff water will continuously infiltrate the pyroclastic-fall deposit layer on the slope below the road subgrade. Finally, groundwater increase in the slope will lead to the pyroclastic-fall deposits sliding along a potential sliding surface.

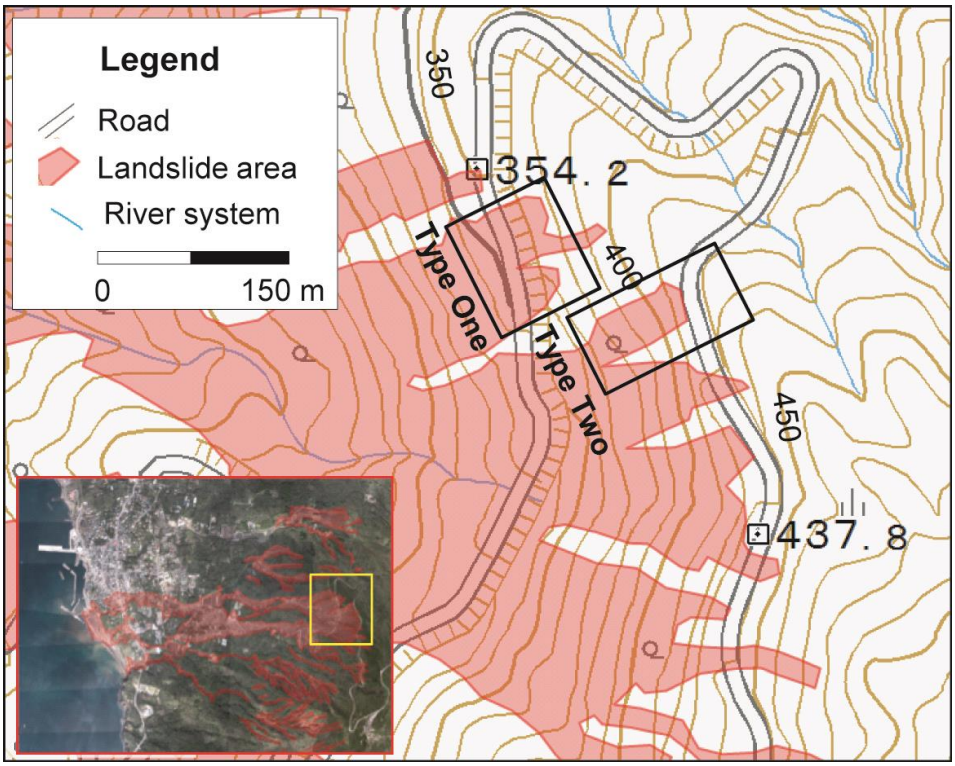

Fig. 5.18 Topographic map of the upper slopes (modified from Geospatial Information Authority of Japan)

5.5.3 Slope angle

According to historical literature, landslide disasters caused by heavy rainfall have occurred several times on the slopes near Motomachi (NIED, 2013; Sakurai, 2014). From the slope angle distribution of the Izu Oshima Island (Fig. 5.5), it is evident that the slopes where landslides have often occurred are quite steep. According to the result of soil property, the pyroclastic-fall deposits can be considered as a cohesionless soil. Therefore, the Eq. (3.4) can be used to discuss the effect of slope angle on the slope stability.

$$F_S = \left(1 - \frac{\gamma_w}{\gamma} \cdot \frac{h}{H}\right) \frac{\tan \phi'}{\tan \alpha} \quad \text{(see 3.4)}$$

where,

H is the thickness of the pyroclastic-fall deposit layer;

h is the height of groundwater level;

α is the slope angle;

γ is the average unit weight of soil, 17 kN/ m^3;

γ_w is the unit weight of water, 9.8 kN/m^3;

ϕ' is the effective friction angle of soil, 38.7 degrees.

For the slope without rainfall infiltration, and in which there is no obvious groundwater level, h in Eq. (3.4) can be assumed to be 0. Therefore, the relationship between factor of safety and slope angle can be plotted as in Fig. 5.19. This results shows that slope will remain stable, even if the slope angle is 38 degrees. Moreover, the slope should be more stable if the matric suction and root resistance are considered into the stability calculation.

Due to rainfall infiltration during heavy rainfall, the groundwater level in the slope will increase gradually, and this will affect the slope stability. Here, m can be used to indicate the relative groundwater level, which is defined as the height of the water level (h) above the slide plane as a fraction of the regolith thickness (H) above the shear plane. Therefore, the Eq. (3.4) can also be expressed as Eq. (5.1):

$$F_S = \left(1 - \frac{\gamma_w}{\gamma} \cdot m\right) \frac{\tan \phi'}{\tan \alpha} \quad (5.1)$$

The relationship of factor of safety (F_S) with the height of the groundwater level and slope angle can be plot as Fig. 5.20. From this figure, it is apparent that relatively

gentle slopes (such as 20 degrees) can remain stable even when the height of groundwater level nearly reaches the ground surface. However, relatively steep slopes (such as 30 degrees) will reach a critical situation when the groundwater level reaches half the thickness of the pyroclastic-fall deposit layer.

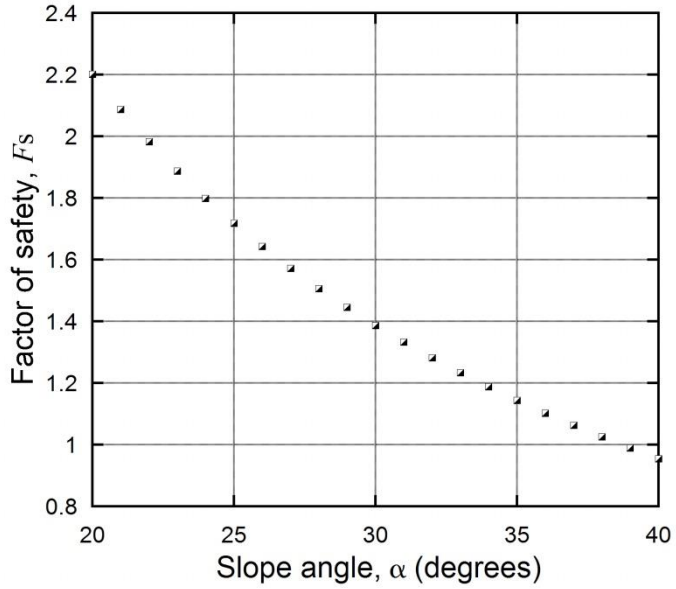

Fig. 5.19 The relationship between factor of safety (F_S) and slope angle

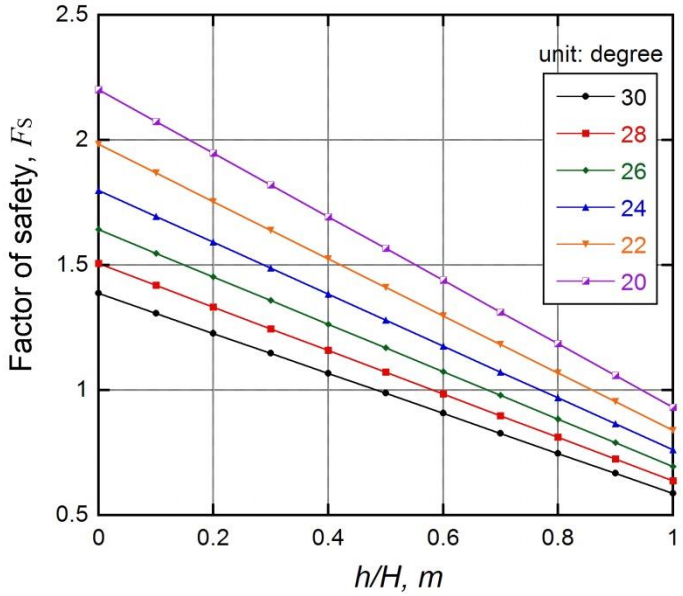

Fig. 5.20 The relationship of factor of safety (F_S) with the height of the groundwater level and slope angle

5.5.4 Static liquefaction

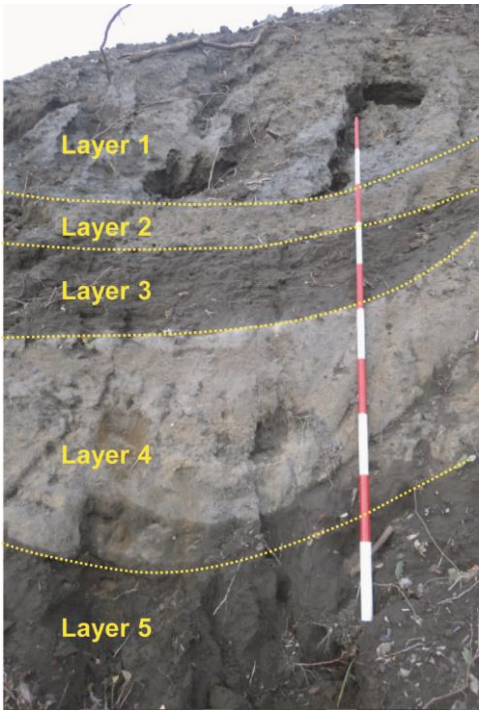

Fig. 5.21 Profile of pyroclastic-fall deposits (S2 in Fig. 5.9)

The profile of the pyroclastic-fall deposits on the slope (Fig. 5.21) shows that several obvious layers are present. Layer 1 is surface soil, mixed with plant roots. Layer 2 and Layer 4 are both yellowish-brown deposits with a tough and cemented structure. Their yellow color originates from abundance of fine clay particles. Therefore, the permeability of these layers is quite low. In contrast to Layers 2 and 4, Layer 3 and Layer 5 are fresh, dark gray pyroclastic-fall deposits with porous structure. Consequently, their permeability and water retention capability are quite high. With this sandwich panel structure, confined groundwater will be generated during continuous groundwater infiltration from the upper slopes. The results of triaxial tests using pore-water pressure control show that static liquefaction can occur in these porous pyroclastic-fall deposits layers. Piping holes were observed on the main scarp in the field, confirming the phenomenon of static liquefaction in porous pyroclastic-fall deposits layers (Wakai, 2014; Inagaki et al., 2014; Daimaru and Sakurai, 2014).

5.6 Conclusions

1. The effective strength of pyroclastic-fall deposits on the upper slope is quite high, and the effective internal friction angle is 38.7 degrees. Consequently, even though the slope is very steep (over 30 degrees), it can remain stable while in an unsaturated condition. Due to heavy rainfall and the porosity of the pyroclastic-fall deposits, rainfall can quickly infiltrate into soil layer. Moreover, the interface above the underlying basalt will stop groundwater infiltration, acting as an impervious boundary. With increase of groundwater level, the effective strength of the porous soil will decrease. Finally, static liquefaction can be triggered, leading to the generation of shallow landslides on the upper slopes.
2. Slope cutting for road construction on the soft-hard slope structure (porous and shallow soil layer mantling the hard basalt layer) should be considered very carefully. Without any preventive measures, the upper layer soil can easily slide along the interface between the soft and hard layers.
3. The drainage system along the road, especially in areas of low terrain, provides an environment which easily gathered runoff water. An amount of water will continuously infiltrate into the slope below the road, leading to shallow landslides.

CHAPTER 6

RAINFALL-INDUCED SHALLOW LANDSLIDES IN HIROSHIMA, JAPAN, IN 2014

6.1 Introduction

In the early morning of 20 August 2014, a high-intensity/short-duration, localized rainfall event triggered many shallow slides and debris flows in the Asakita and Asaminami Wards in the northern part of Hiroshima City, Japan. In all, there were 166 slope failures triggered by the heavy rainfall event, including 107 debris flows and 59 shallow slides, which caused 44 injuries and 74 deaths. In addition, 133 houses were destroyed and 296 houses were severely damaged (Ministry of Land, Infrastructure, Transport and Tourism, 2014; Yamamoto and Kobayashi, 2014). Shallow slides were designated as those that moved for a limited distance from the source area. Most of the loss of life and property was caused by debris flows. In this paper, all of the slope failures are called debris flows for simplification. Fig. 6.1 illustrates the distribution of debris flows and fatalities. As indicated, the debris flows were distributed in an elongated area extending northeast to southwest and covering the Asaminami Ward and Asakita Ward. Most of the fatalities were concentrated in the Asaminami Ward (Asa is the name of the region; Asaminami means Southern Asa, while Asakita means Northern Asa, in Japanese).

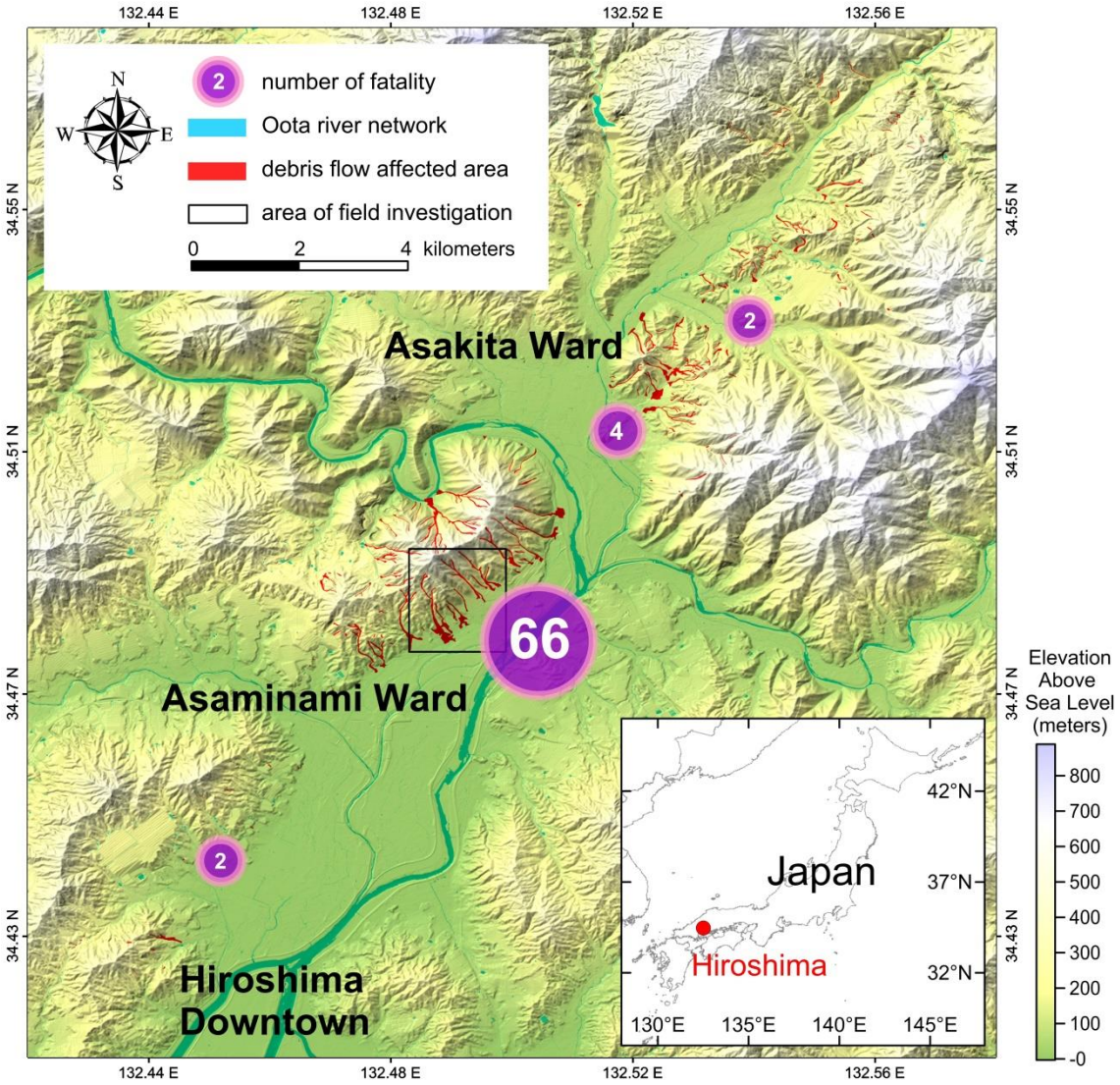

Fig. 6.1 Distribution of debris flows and landslide-affected area and number of fatalities. The longitude and latitude is in the decimal format in the all figures hereafter. The debris-flow distribution and fatality number are obtained from Ministry of Land, Infrastructure, Transport and Tourism. DEM data is from Geospatial Information Authority of Japan (GSI). The black rectangle indicates the study area.

In past decades, many landslide and debris flow events have been triggered by high intensity, short-duration rainstorms, and caused loss of life and infrastructure damage worldwide (Sassa et al., 1997a, 1997b, 1998; García-Martínez and López, 2005; Casagli et al., 2006; Tang et al., 2012; Cevaso et al., 2014; Chen et al., 2014; Ni et al., 2014). For example, in December 1999, extreme rainfall on the northern Venezuelan coast

triggered a disastrous debris flow, which caused about 1,500 fatalities and the destruction of 23,000 houses (García-Martínez and López, 2005). Recently, Japan also suffered from many disasters triggered by extreme rainfall. In September 2011, Typhoon 12 (Talas) attacked the Kii peninsula of central Japan and triggered many landslides and floods, causing 97 casualties (Saito and Matsuyama, 2012). Then in July 2012, an unprecedented four-day heavy rainfall hit Kyushu in Southwest Japan and formed devastating floods and mudslides, and was associated with 32 people who were reported either dead or missing; 400,000 people were evacuated from their homes (Duan et al., 2014). Disasters triggered by extreme-rainfall have become a critical and urgent issue for society.

In the Hiroshima area, the 2014 events were preceded by other catastrophic sediment disasters in recent years. At the end of June 1999, 139 debris flows and 186 shallow slides were triggered by rainfall, and caused 32 deaths in a nearby area (The Chugoku Shimbun Online, 1999; Wang et al., 2003). Mainly because of this disaster, a law referred to as the "Sediment Disaster Countermeasures for Sediment Disaster Prone Areas Act" was enacted in 2000 to prevent sediment problems caused by debris flows and other causes. Despite the protection of the law for the previous 14 years, the loss of life caused by debris-flow sediment disasters triggered by one heavy rainfall event was not prevented; indeed the loss of life in the 2014 events was almost three times that in 1999. These events brought a huge amount of distress, and severely impacted the local community. The public as well as the academic community are extremely interested in the causes of the disaster and desire to know the triggering factors and field conditions. Many methodologies have been developed and applied to this topic. To reveal the disaster impact in a larger area, statistical analysis is applied to analyze landslide susceptibility in terms of slope inclination, land use, and other factors (Lepore et al., 2012; Tang et al., 2012; Winter et al., 2013; Cevaso et al., 2014; Chen et al., 2014; Dijkstra et al., 2014). On the other hand, for a localized catchment, the physically-based models, e.g., slope stability analysis and hydrological models, (Casagli et al., 2006;

Tsuchida et al., 2014) or field monitoring and laboratory tests (Montgomery et al., 2009; Okada and Kurokawa, 2015) are used to analyze the initiation mechanism of shallow landslides or mudslides under different rainfall conditions. In order to assess the future risks in the disaster area, field survey and laboratory tests for the analyses of geological and geomorphological conditions, and soil properties are considered in this paper. Therefore, we shall report the hazard background briefly as well as the results of the field survey and laboratory analysis of soil mechanical and geochemical properties. As shown with a black rectangle in Fig. 6.1, our investigation focuses on two debris flows in the Asaminami Ward, which suffered major life loss due to its higher population density on the narrow alluvial plain, compared to the Asakita Ward.

6.2 Geological condition

Fig. 6.2 illustrates the geology of the affected area. Debris flows were distributed in an area 10 km by 2 km, extending in a NE-SW direction. The elevation in this area reaches 700 m. A valley, which is controlled by a NE-SW fault, trends through this area. Late Cretaceous granite, also called Hiroshima granite, is the main bedrock in this mountainous region. In the valley and lower slopes, deposits of weathered granite are encountered. In the area of Hiroshima granite, coarse granite is mainly distributed in the middle and lower slopes of the mountain, and fine granite overlies the coarse granite. Generally, the grain size in fine granite is around 1 mm, and in coarse granite is several mm (Takahashi, 2014). In some places, hornfels overlays the coarse granite. Hornfels is a contact metamorphic rock. It is formed when sandstone and shale are indurated and transformed by the heat of intrusive granite. Relatively, the fine granite and hornfels are much more resistant to weathering than coarse granite. As a result, the slopes in fine granite and hornfels are generally steeper than those in coarse granite. The coarse Hiroshima granite is very easily weathered. The granitic soil (i.e. the residual soil) is locally called Masa-do, which means “real sand” in Japanese. Because of the intense wreathing, the Masa-do can easily lose its structure and collapse during heavy rainfall.

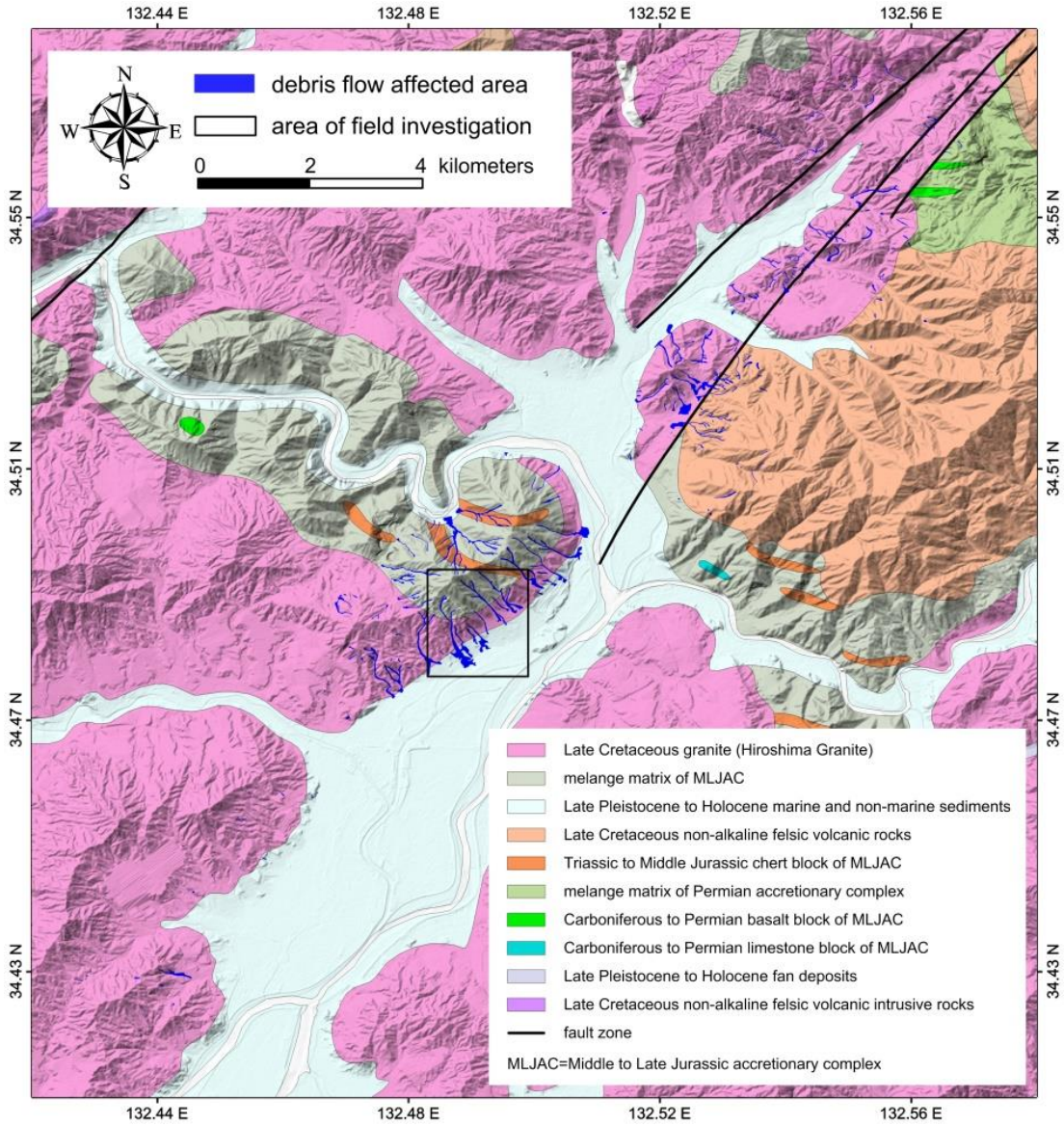

Fig. 6.2 Geological map (1:200,000) and debris flow and landslide distribution. The data are extracted from Geological Survey of Japan, National Institute of Advanced Industrial Science and Technology. The main types of rock in the target area, indicated by a black rectangle, are Hiroshima granite and Hornfels.

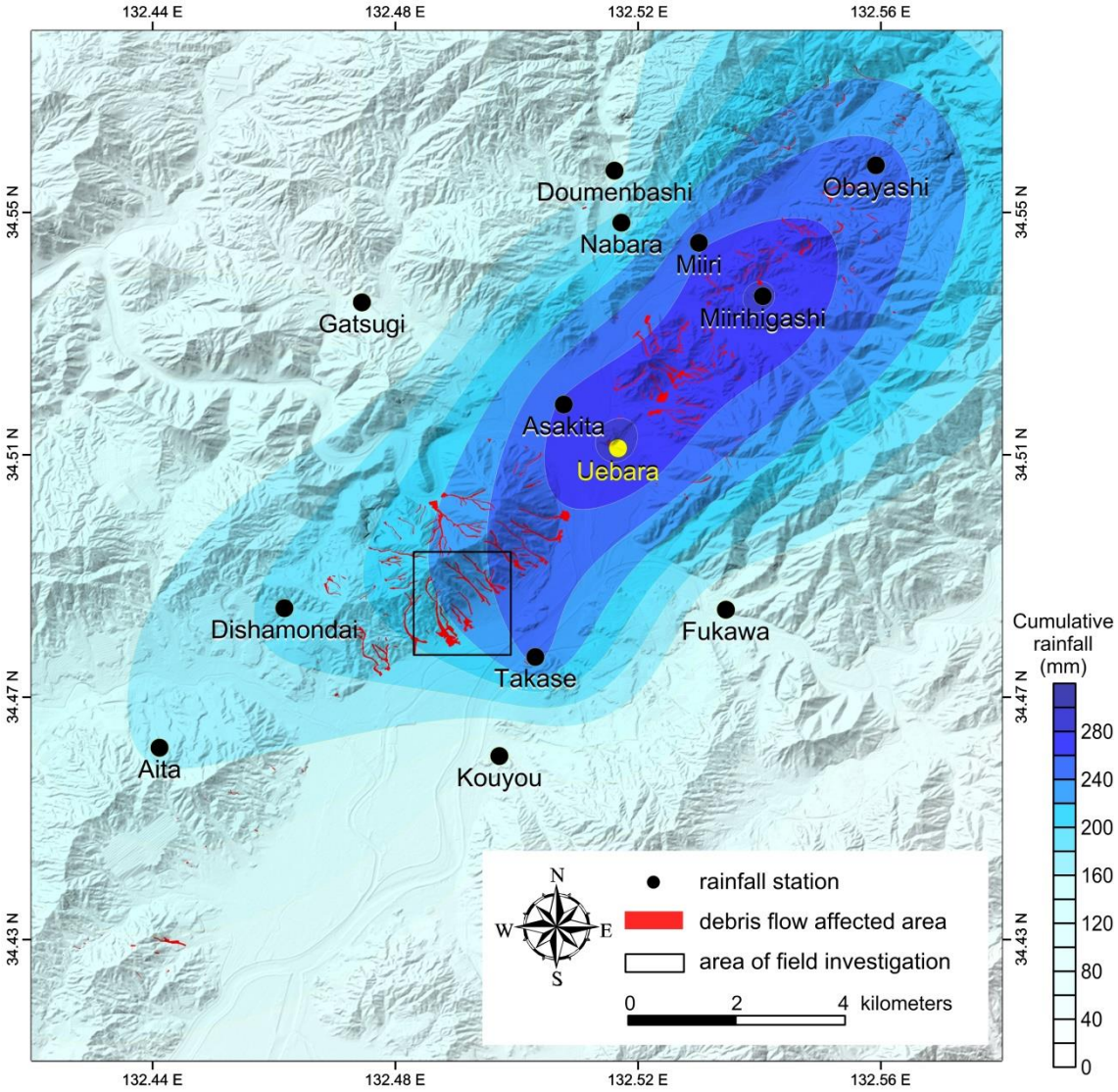

Fig. 6.3 Isohyetal map of cumulative rainfall on 19 and 20 August 2014. The data found in the isohyetal lines are interpolated using the data from 13 stations (marked by solid black circles) of the Japan Meteorological Agency, Hiroshima Prefecture Government, and Ministry of Land, Infrastructure, Transport and Tourism. The maximum rainfall occurred at the Uebara meteorological station, with an amount of 287 mm. The debris flows and landslides occurred along the area with intense rainfall. The hourly rainfall hydrograph at the Uebara meteorological station, which is located at the center of the area affected by debris flows.

6.3 Heavy rainfall

The main triggering factor of the debris flows was the high intensity and short duration rainstorm. Fig. 6.3 illustrates the isohyetal map of the cumulative rainfall for 48 hours on 19 and 20 August 2014. It shows that most of debris flows occurred in the area of intense rainfall, of which the cumulative rainfall is greater than 200 mm. The maximum rainfall was recorded at the Uebara meteorological station, with an amount of 287 mm, and the recorded maximum in three days during the disaster is almost 2.6 times the August monthly-average value of 110.8 mm in Hiroshima (Japan Meteorological Agency, 2015). Fig. 6.4 shows the hourly rainfall hydrograph at the Uebara meteorological station. The maximum three-hour rainfall is 236 mm from 2:00 to 5:00 a.m. (local time) on 20 August. In particular, the maximum hourly rainfall is 115 mm at 4:00 a.m. on the same day. Witnesses verified that the debris flows occurred around 4:00 a.m. on the same day (The Japan Times, 2014). We conclude that this unusual and extreme rainfall is the main triggering factor of these events.

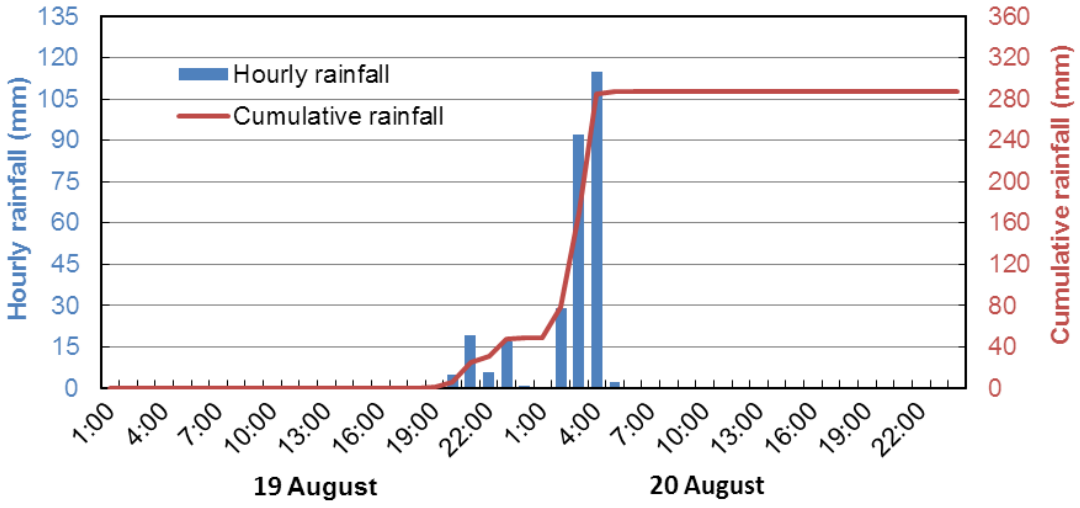

Fig. 6.4 Hourly rainfall at the Uebara meteorological station on 19 and 20 August in 2014. The cumulative rainfall is 287.0 mm. The maximum hourly rainfall is 115.0 mm at 4:00 a.m. (local time) on 20 August 2014. The maximum three-hour rainfall is 236.0 mm from 2:00 to 5:00 a.m. on 20 August 2014. (Data source: Hiroshima Prefecture, 2014)

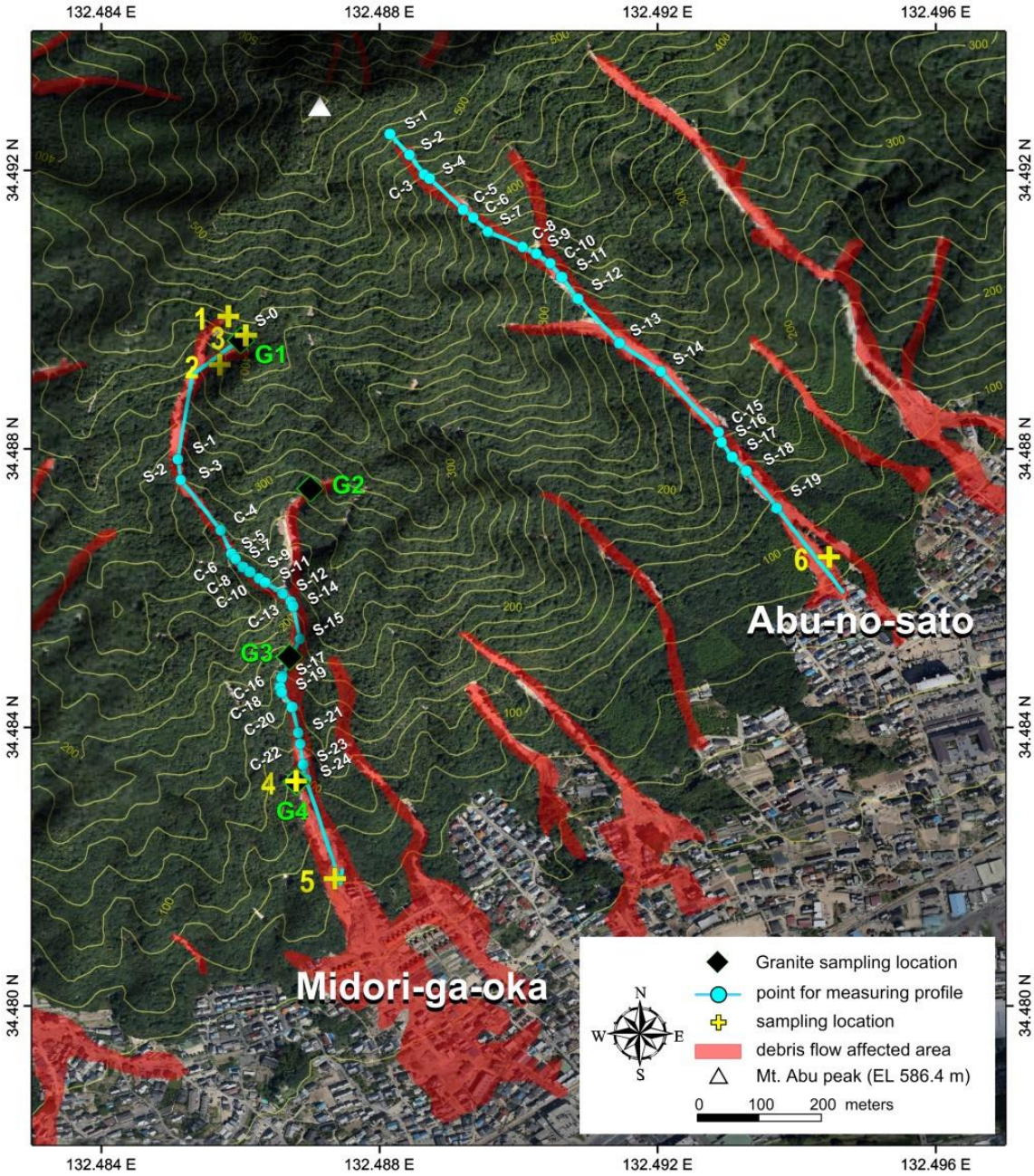

Fig. 6.5 Aerial photograph and locations for soil sampling (solid yellow crosses) and granite (black diamonds), and locations for measuring longitudinal profile and cross sections (solid cyan circles). The aerial photograph (extracted from Google Earth) was captured on 13 September 2014.

6.4 Field investigation

The field investigation was conducted on two gullies in which the greatest number of fatalities occurred, called Midori-ga-oka and Abu-no-sato, respectively (Fig. 6.5). Both of the debris flows originated from similar elevations and can be categorized as channelized, but their affected areas are quite different. The Midori-ga-oka debris flow entered the residential area and persisted over a long distance while also spreading to cover a wide area. This phenomenon can also be observed in Fig. 6.6 (a). However, the Abu-no-sato debris flow stopped behind the residential area (Fig. 6.6b). The different travel distances may imply different mobility rates of the debris flows. Understanding the factors causing the different mobility may be helpful for disaster reduction. For this reason, we selected these two debris flows for detailed study.

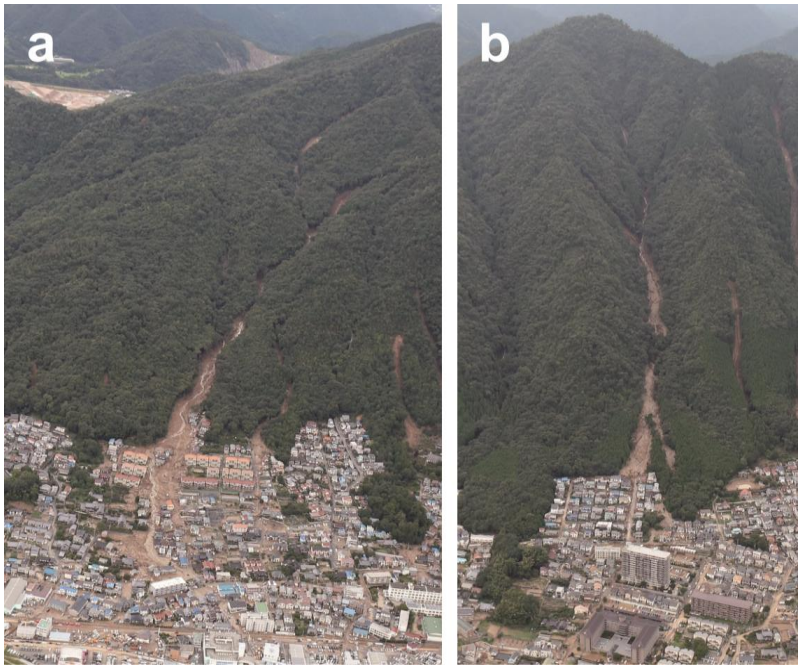

Fig. 6.6 Photographs of the Midori-ga-oka debris flow (a) and Abu-no-sato debris flow (b) taken on 20 August 2014 (courtesy of Geospatial Information Authority of Japan)

In the field investigation, observation of the geological conditions, measurement of the longitudinal and cross-sectional profiles, and the collection of soil samples in source

and deposition areas were the main objectives. Along the whole gully, the longitudinal and cross-sectional profiles at every cliff and slope were measured using laser rangers, ranging rods, inclinometers and GPS trackers. The locations for measurement are marked by solid cyan circles in Fig. 6.5. At each point, the label was assigned an “S” for a slope or “C” for a cliff, and followed by a sequential number from upstream to downstream in ascending order. The source areas were investigated in more detail. The deposit profile is also shown in the longitudinal sections. Undisturbed and disturbed soil samples were collected in both gullies (see Fig. 6.5 for sampling locations). In the Midori-ga-oka debris flow, three undisturbed samples (Nos. 1 and 2 in the left source area, and No. 3 in the right source area) were collected for the analysis of physical parameters and the mechanical properties of the soil. At the location of sample No. 3, a disturbed soil sample (labeled as No. 3-DIS) was also collected for the analysis of the initiation mechanism, for use with triaxial tests. In the deposition area of the two gullies, three samples (Nos. 4, 5, and 6) were collected for grain size analysis and permeability characterization.

6.5 Results and discussion

6.5.1 Characteristics of gullies and debris flow

Based on the field investigation, the geological conditions were found to be different in the source areas of the two debris flows. The source area of the debris flow in Midori-ga-oka is composed of coarse granite, with intrusive fine granite. In the coarse granite, sheeting joints and micro-sheeting joints are well developed. The average thickness of the granitic soil is about 1 m. In the main channel of the debris flow, all of the granitic soil was removed, and only the gully bed consisting of fresh granite was left. The situation along the gully will be introduced in details later. For the debris flow in Abu-no-sato, the source area is located in hornfels. In this gully source area (where the debris flow originated), the weathered soil layer is thin, with an average

thickness of 0.7 m. The bedrock in the channel is stiff hornfels.

Fig. 6.7 shows photographs taken along the gully of the Midori-ga-oka debris flow, from the source area to the bottom. Fig. 6.8 shows the muddy trace of the debris flow on buildings in one of the prefectural housing areas. In the source area, two shallow slides occurred in the granitic soil. In Fig. 6.7a, the left-hand shallow slide (source area) has, in the upper part, a slope angle of 37.7 degrees, a width of 7.9 m and a horizontal distance of 7.4 m, and, in the lower part, a slope angle of 33.9 degrees, similar width, and a horizontal distance of 64.5 m. The right-hand shallow slide has, in the upper part, a slope angle of 37.4 degrees, width of 14.4 m, and horizontal distance of 19 m, and, in the lower part, a slope angle of 32.4 degrees, a similar width and horizontal distance of 47.0 m. In the travel path of the debris flow, the gully is V-shaped (Fig. 6.7b) in the upper part near the source area, and becomes a U-shape in the middle and lower part (Fig. 6.7c, e, f). There are almost no deposits in the flow channel (Fig. 6.7c, f). All of the debris coming from the weathered granite has been transported out of the terminal area of the debris flow channel (Fig. 6.7g), and deposited on the slope where a residential area is located (Fig. 6.7h). Forty-one lives were lost in this area, including those living in the prefectural housing and private houses. Among them, Midori-ga-oka prefectural housing that consisted of 21 three-floor reinforced concrete residential buildings, were directly hit by the debris flow (Fig. 6.8). It was found that in the middle and lower part of the gully, the sheeting joints were well developed (Fig. 6.7d). This caused the weathered granite above the major sheeting joint to easily erode away, and the volume of the debris flow became larger and the debris flow increased in magnitude and kinetic energy as it flowed down the steep gully. The material in the debris flow deposits is rich in fine soil particles, being granitic soil, or Masa-do. The fine soil particles may decrease the permeability of the debris flow, and cause greater mobility, in turn contributing to the longer travel distance and greater lateral spread. To confirm this inference, soil samples were taken from the deposition area and the grain size distribution was analyzed in the laboratory.

Fig. 6.9 illustrates the longitudinal profile as well as the cross-sectional profiles at all measurement locations (see Fig. 6.5) in the gully of the Midori-ga-oka debris flow. From these measurements, the following aspects were evident:

1) The longitudinal profile consisted of gentle slopes (slope angle < 30°, indicated as S) and steep cliffs (slope angle > 40°, indicated as C);
2) Most of the cliffs were located at the middle and lower part of the gully;
3) The cross sections were in a V-shape from S-1 to S-3, and became U-shaped from S-5 to the end (S-21). The section became narrow in the area between S-3 and S-17. Notably, the width change from S-15 to S-17 is very sudden. This could have caused a debris dam between S-15 and S-17, and a later collapse of the dam may have caused a debris flow of greater magnitude. This sudden narrowing in the cross section has a significant effect on the motion of the debris flow as it flowed to the residential area, because of the constricted flow channel.
4) Nearly all of the debris deposited on the riverbed of gentle slope in the gully.

Fig. 6.10 shows the Abu-no-sato debris flow gully from the source area to the deposition area. The source area is located in hard hornfels rock (Fig. 6.10a). The sliding direction is S20°E. The slope angle is 40 degrees. The width is about 5 m, the length about 30 m, and the depth to the sliding surface, which is the outcropped bedrock, is about 0.7 m. The bedrock is fractured with joints, and two nearly vertical faults with a width of 0.15 m passed through the source area. After a short flow in a wide gully slope, the debris flow was limited to a narrow gully at a cliff C-3 (Fig. 6.10b), and dropped down, nearly vertically for about 5 m. Lower down, it passed several slopes and cliffs, and left the hornfels area. The gully in that upper part was V-shaped, and the gully bed consisted of fractured hornfels (Fig. 6.10c). In some part, colluvium deposits existed in the gully (Fig. 6.10d). Because of the large boulder size, compared with the smaller grain size debris flow material, these would be a higher permeability, and thus transportation would be less likely in this area. After flowing out of the hornfels bedrock

area, and into the coarse granite bedrock area, the slope angle became gentle (17.7 degrees), and most of the boulders deposited at the bottom of the gully (Fig. 6.10e). Because the content of the debris flow is composed of boulders, most of the boulders were deposited in the gentle and wide slope before they reached the residential area as pore water pressure reduced rapidly. However, an old debris flow deposit terrace caused a dam of the debris flow. Collapse occurred at both sides of the terrace, and deep erosion developed (Fig. 6.10f shows the right side narrow channel). Through the narrow channels, part of the debris flow including boulders and fallen trees were deposited on a wide gentle slope (Fig. 6.10g). A small amount of debris-flow material flowed beyond the boundary between the natural slope and the residential area (a local road), destroyed two houses and caused 4 deaths. Some houses along the slope road (see Fig. 6.6b) were damaged to different extents, mainly by rolling boulders and rapid water flow.

Fig. 6.11 illustrates the longitudinal section and cross sections at all measurement locations (see Fig. 6.5) in the gully of Abu-no-sato debris flow. From the information in the figure, the following effects can be observed.

1) The slope was steep in the hornfels area, and became gentle in the coarse-grained granite area.
2) Most of the cliffs were distributed in the middle and upper parts of the gully.
3) The gully was V-shaped in most of the hornfels area, and gradually became wider.
4) From C-15 to S-17, the cross sections narrowed rapidly. This change may have caused a dam in the debris flow, and the later outburst may be a direct cause of the disaster.

Compared with the Midori-ga-oka debris flow, the distance between the residential area and the starting point of the deposition area is much larger in Abu-no-sato debris flow. It may mean that keeping enough space between the deposition start point and the residential area is very important for disaster reduction.

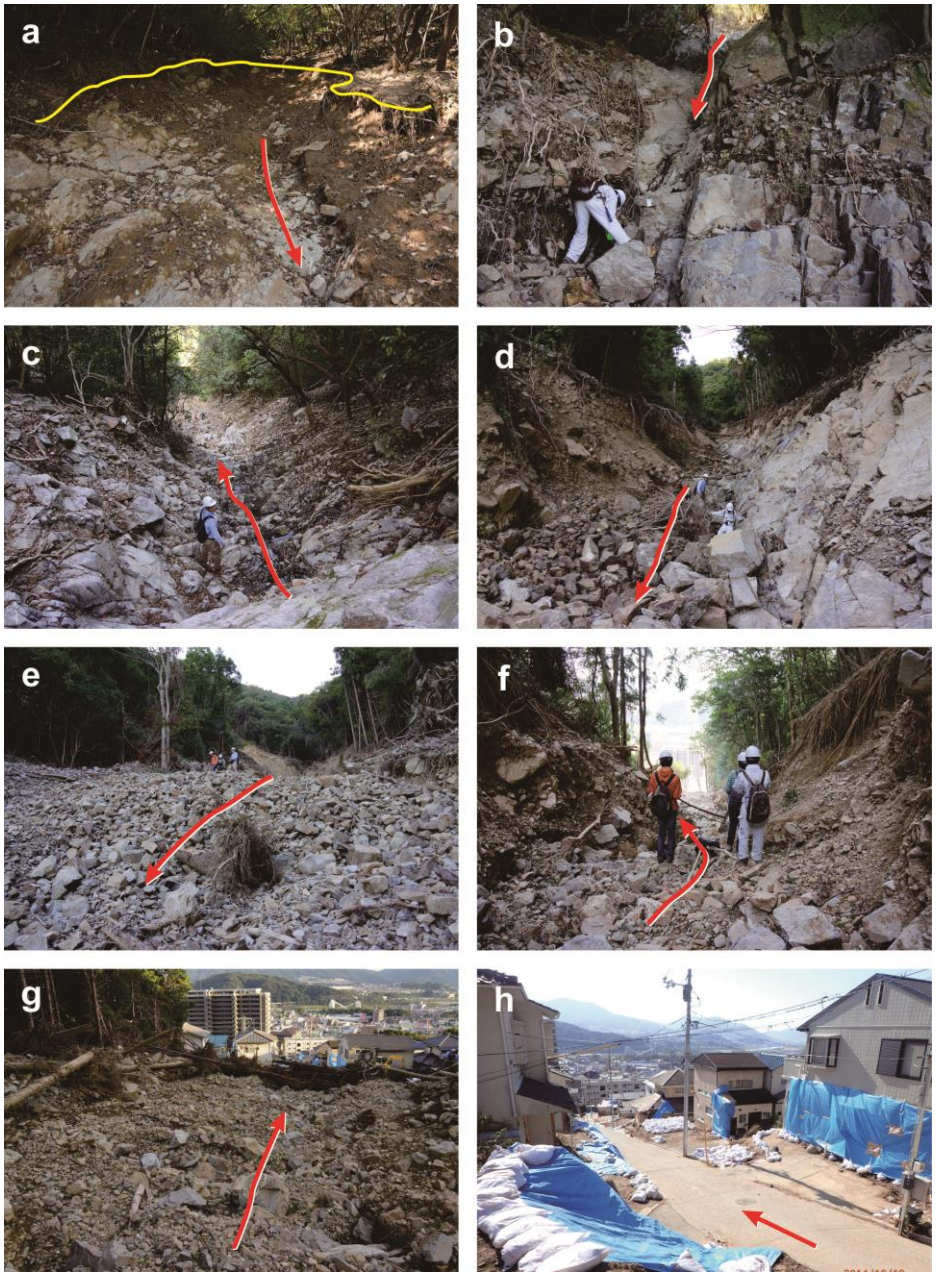

Fig. 6.7 Photographs showing the gully of the Midori-ga-oka debris flow. Arrows point in the downstream direction. a) three branches in the source area (at cross section S-0 in Figure 5); b) strongly weathered granite bedrock exposed by the erosion of debris flow (S-1); c) shallow bedrock gully after erosion by the debris flow (S-2); d) erosion along the sheeting joints in granite (C-4); e) bedrock gully with few debris flow deposits (C-6); f) granite bedrock gully after extreme erosion, near the bottom of the gully (S-19); g) the bottom of the debris flow gully, where deposits of different grain size appeared and a temporary ring net countermeasure (at S-23) was finished in December 2014; h) severely damaged residences beside the pathway of the debris flow, these houses were built on previous debris flow deposits.

Fig. 6.8 The damaged prefectural housing at the pathway of the Midori-ga-oka debris flow. From the muddy trace on the wall, the flow depth of debris flow was about two-floors high.

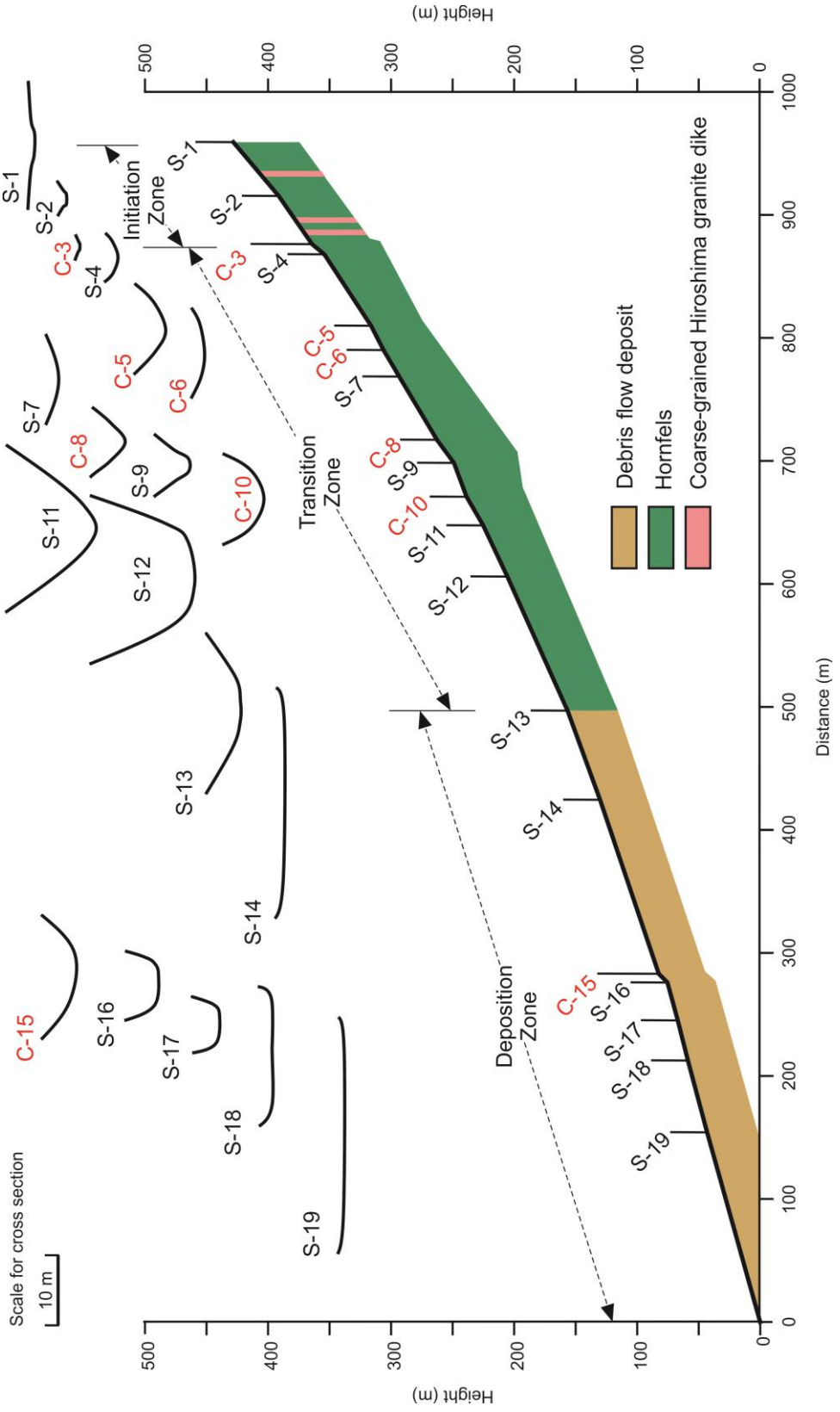

Fig. 6.9 Longitudinal section and cross sections of the Midori-ga-oka debris flow gully

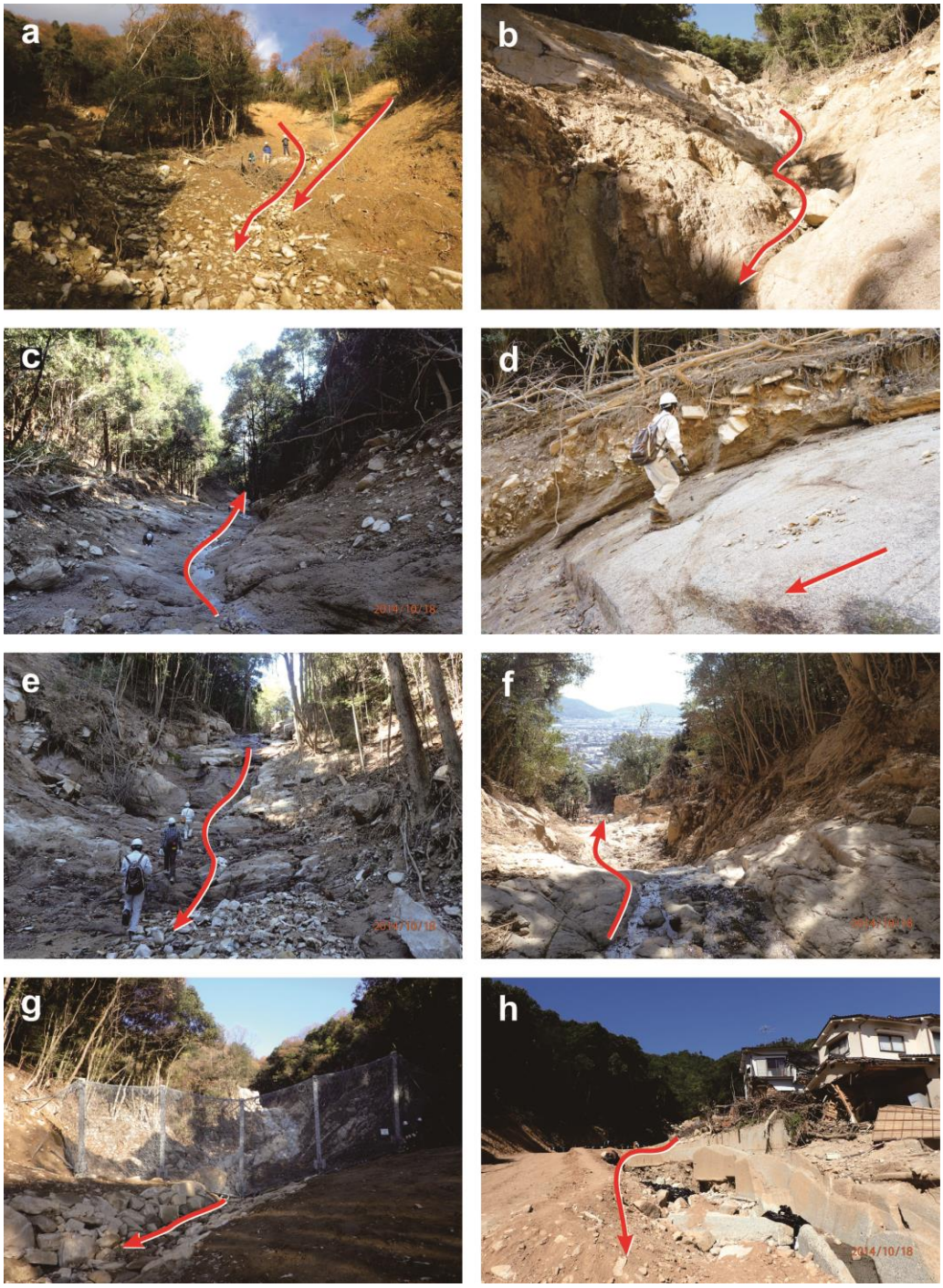

Fig. 6.10 Photographs in the gully of Abu-no-sato. Arrows point in the downstream direction. a) source area, the scarp is marked by a yellow line (at cross section S-0); b) cliff with a joint (C-3); c) gully-bed with fractured rock, no deposits (S-4); d) V-shaped gully, with colluvium from one side (S-7); e) bottom of the gully, coarse-grained deposits of 30 cm average diameter was widely distributed (S-14); f) narrow neck of the gully (S-16); g) downstream deposit area with shallow coarse-grained layer (S-19); h) the houses along a road damaged by the debris flow in the Abu-no-sato community

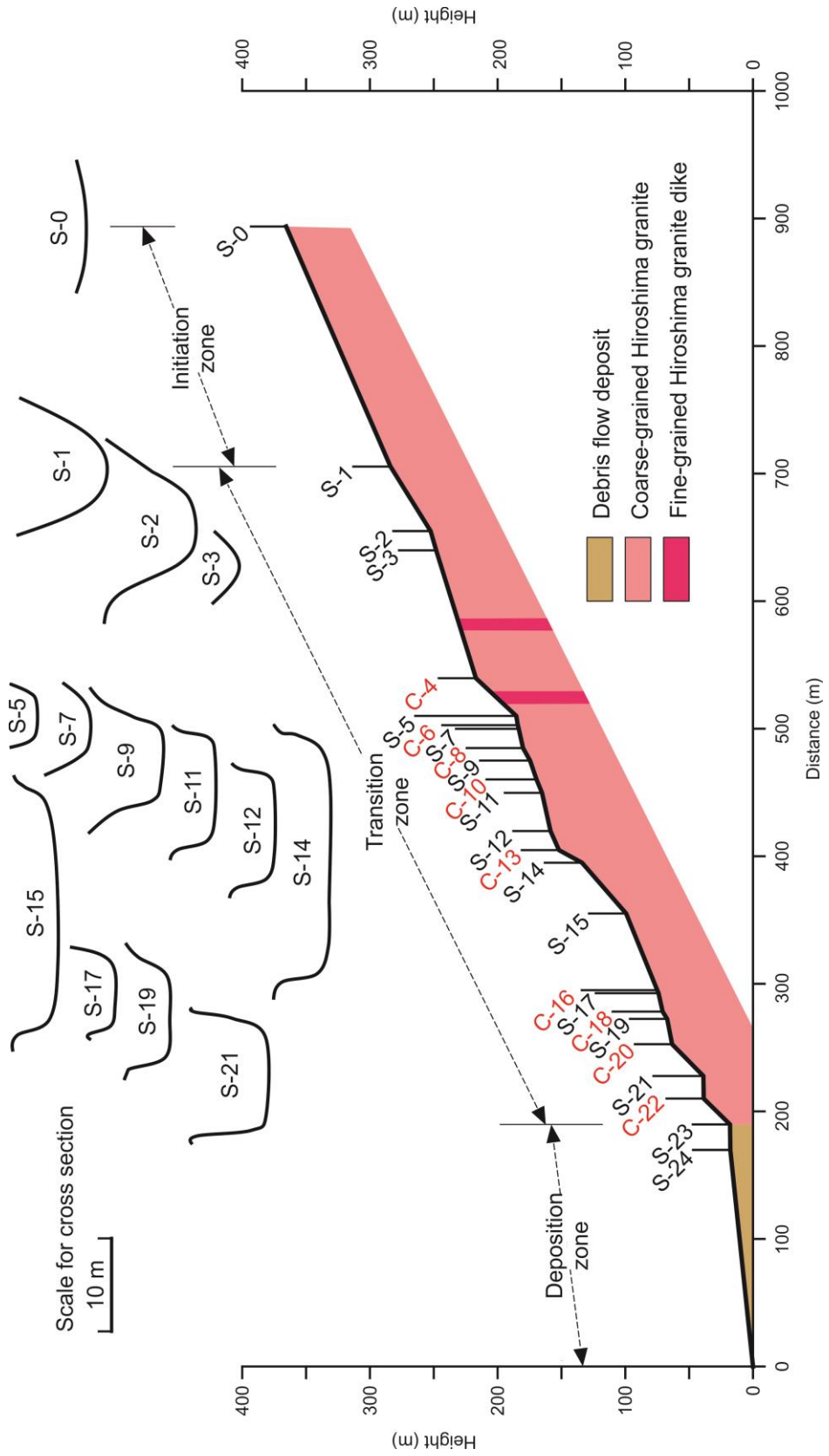

Fig. 6.11 Longitudinal section and cross sections of the Abu-no-sato debris flow gully

6.5.2 Soil properties

Table 6.1 shows the physical parameters of undisturbed sample Nos. 1, 2 and 3. The value of specific gravity for all samples is around 2.640. Samples Nos. 1 and 2 are from the same landslide, and have similar properties. The dry densities of sample Nos. 1 and 2 are higher than that of sample No. 3.

Table 6.1 Parameters of soil samples in the source area of the Midori-ga-oka gully

Sample No.	**1**	**2**	**3**
Specific gravity, G_S	2.640	2.643	2.638
Dry density, ρ_d (kg/m^3)	1,370	1,390	1,190
Water content, *w* (%)	15.2	19.5	31.5
Liquid limit, *LL* (%)	—	—	32.1
Plastic limit, *PL* (%)	—	—	23.4
Plastic Index, *PI* (%)	—	—	8.7

Fig. 6.12 illustrates the grain size distribution of all samples (Nos. 1 to 6). Sample Nos. 1 to No. 5 are from the Midori-ga-oka debris flow gully. Nos. 1, 2, and 3 are from the source area, and Nos. 4 and 5 are from the exit of the gully, the first deposit of the debris flow. Sample No. 3 comprises much finer particles than the other samples, and the mean grain size D_{50} is 0.035 mm. While the mean grain sizes of samples Nos. 1, 2, 4 and 5 are close to 1 mm, their distributions are also similar. Comparing the sample from the deposition area with that from the source area, the grain size is not much different. The amount of fine particles is slightly less in the deposition area. This may mean that the finer particles are transported for a longer distance. Sample No. 6 is from the lower part of the deposition area of the Abu-no-sato debris flow, which has the smallest grain size in the debris flow deposit. In the upstream part, the deposit generally consists of boulders with a mean size of 0.3-0.5 m, and a maximum size up to 1.5-2.0 m. From the grain size distribution, it can be seen that the particles in the Midori-ga-oka debris and the Abu-no-sato debris flows are different in grain size and, in turn, we can infer that

they have different permeability and drainage characteristics. At a given travel velocity, the low permeability, which is associated with a slower rate of drainage of the debris at Midori-ga-oka (mainly consisting of granitic soil), may mean that the flow has greater mobility and may travel for a longer distance because it remains in the saturated condition for longer. The boulders in the Abu-no-sato debris flow mean that deposition occurs much earlier as the debris drains rapidly and changes to the unsaturated condition. The critical velocity of a debris flow transformed from saturated to unsaturated condition will be of significance in predicting the run-out mobility of debris flow.

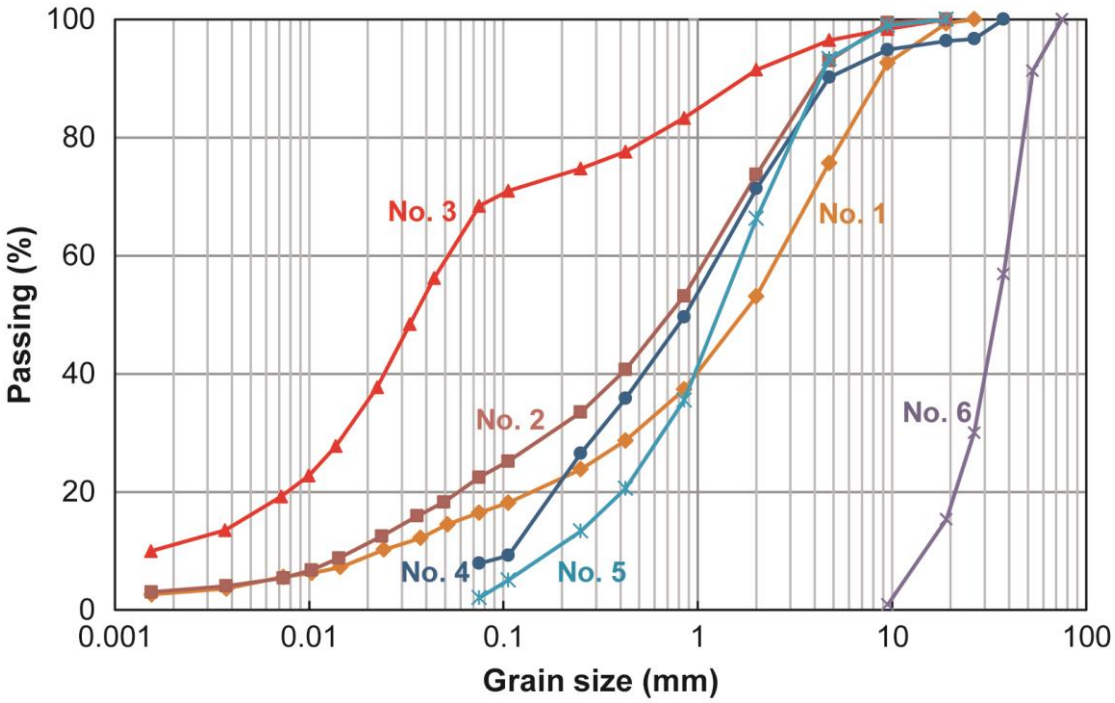

Fig. 6.12 Grain size distribution of samples Nos. 1 to 6

Composed of 70% of particles finer than 0.1 mm, sample No. 3 was used to conduct the Atterberg limit tests. The results are shown in Table 6.1. In addition, Fig. 6.13 shows that the soil classification of the sample No. 3 is between Silt (ML) and Low plasticity Clay (CL) with a low liquid limit (ASTM D2487-06, 2006).

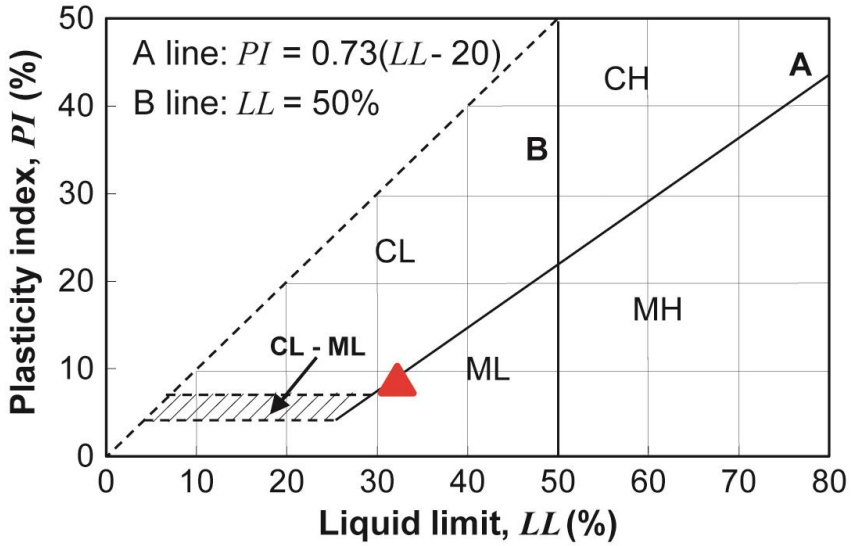

Fig. 6.13 Plasticity chart of sample No. 3 (red solid triangular). Modified from ASTM D2487-06 (2006). CL=Lean clay; ML=silt

6.5.3 Shear strength of soil

The stress-strain relation of the consolidated-undrained tests on the saturated specimen (Fig. 6.14a) shows that the deviatoric stress increases in the beginning. When the axial strain is about 2%, the deviatoric stress reaches the peak value. After that, the deviatoric stress turns to decrease with the axial strain. Bulging failure was observed for all specimens at the end of the tests. The stress-strain curves indicate that the critical state of the soil will be reached at low strains value.

The relation between excess pore-water pressure and the axial strain in the consolidated-undrained tests on saturated specimens is shown in Fig. 6.14b. Positive excess pore-water pressure was generated in all three undrained tests. In all soil specimens, the positive excess pore-water pressure increases to a high value with minor strain, and increases slowly as the strain increases continuously. Finally, the value of pore water pressure is close to the confining pressure, indicating that the soil would liquefy if the strain continued to increase.

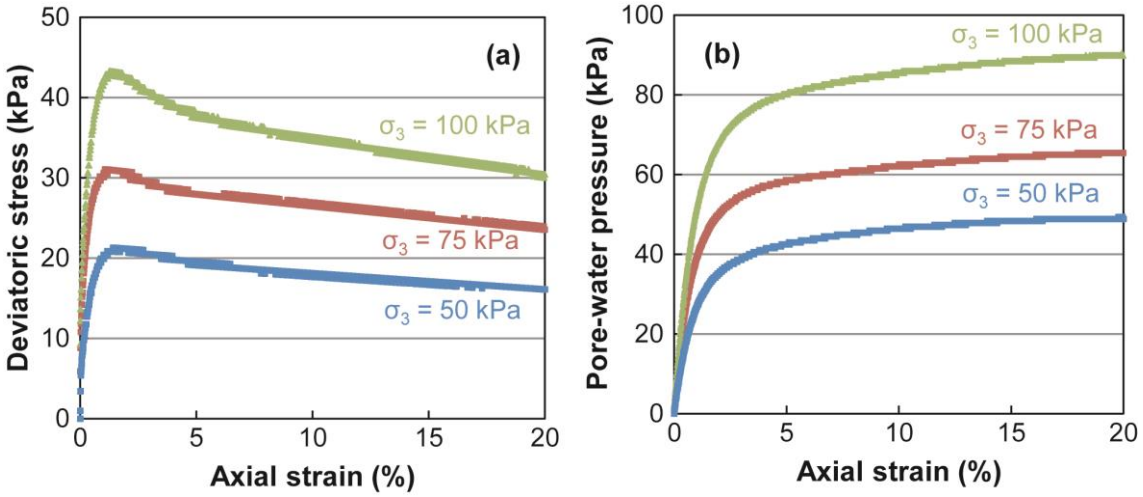

Fig. 6.14 Results of the consolidated-undrained tests: (a) stress-strain relationship; (b) relationship between pore-water pressure and axial strain

All of the effective stress paths show a similar trend. Each path moves to the right initially, and then moves toward the left until reaching the critical state line (CSL) at the end of the test. The critical states of the saturated specimens can be represented by the CSL in the stress plane, as shown in Fig. 6.15. The gradient of the critical state line is 0.404. This corresponds to an internal effective friction angle of 23.8 degrees and cohesion of 5.5 kPa of the granitic soil.

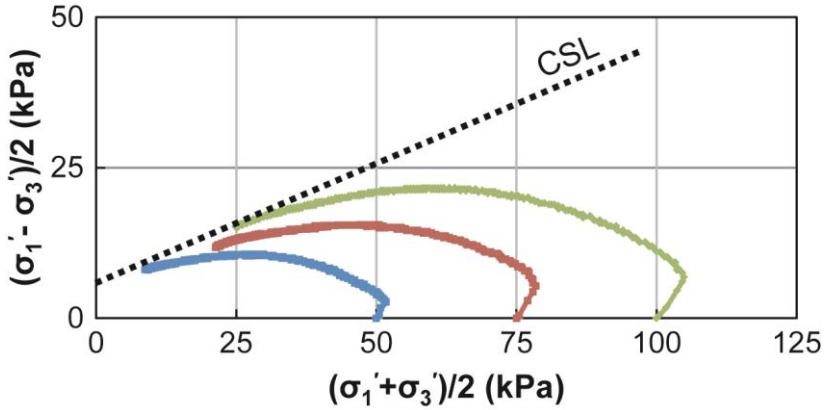

Fig. 6.15 Effective stress paths under different confining pressures (50, 75 and 100 kPa); the dotted line is the critical state line (CSL).

6.5.4 Soil behavior with the increase in pore-water pressure

To determine the initial stress condition of soil sample No. 3-DIS, the thickness (H) of the soil layer and slope angle (α) are assumed as 1 m and 35 degrees, respectively, based on the field measurement results in the source area of the debris flow. As shown in Table 6.1, the unit weight (γ) of the natural soil is 15.6 kN/m^3. From consolidated-undrained triaxial tests, the internal effective friction angle (ϕ') of the soil is 23.8 degrees. The initial maximum principal stress (σ_1) and minimum principal stress (σ_3) are 21.7 and 5.7 kPa, respectively. Through the pore-water pressure controlled triaxial test, the relations between deviatoric stress, axial strain and pore-water pressure were obtained (Fig. 6.16).

Fig. 6.16 shows that, when the pore-water pressure increased to about 4.0 kPa, the deviatoric stress started to decrease, while the axial strain increased. The same soil behavior also can be found in Fig. 6.17. The effective stress path begins to go down when pore-water pressure increases to about 4.0 kPa (point B). After this point, yielding occurs, and the effective stress path moves downward and to the left, and then reaches the critical state line (point C, where pore-water pressure is 6.5 kPa). This shows the major failure of the soil. With the continuous supply of pore-water pressure, the stress path moves down and left along the critical state line, and ends at point D, where the pore-water pressure is 8.3 kPa. This simulation test can explain the initiation mechanism of the shallow landslide that occurred on a steep slope. During heavy rainfall, continuous rainfall infiltration can generate a wet front in the soil slope and in turn form a saturated zone above the potential sliding surface. Gradually, the saturated zone will move upwards in relation to the slope surface, and the pore-water pressure acting on the potential sliding surface will increase. Finally, it will cause shallow landslide. Because this phenomenon occurs in steep slopes, it will create a debris flow moving downward for a long distance. From the test, we can see that, with low pore-water pressures (i.e., when the rainfall is not so heavy), the slope can maintain stability. However, if the pore-water pressure exceeds the critical value, as a result of heavy rainfall, for example,

shallow landslide will be triggered. In this simulation test, the critical value of the pore water pressure is about 4.0 kPa. Considering the slope angle of the source area is 35 degrees, and the thickness of the initial sliding mass is 1 m, the pore-water pressure of 4.0 kPa and 6.5 kPa mean that the groundwater levels are about 0.60 m and 0.97 m high, respectively, above the sliding surface. So when the groundwater level rises to 0.6 m above the potential sliding surface, instability may occur in the slope, and deformation may develop. When the groundwater level rises to 0.97 m, the slope will completely fail. For a slope with depth of 1 m, the groundwater level of 0.97 m almost means the existence of surface flow along the slope. These two values of the groundwater level may be used as a reference for the prediction of shallow landslide initiation under similar condition. Since the soil sample used for triaxial tests is disturbed soil, the in-situ critical value of the pore-water pressure may be slightly higher than experimental value. However, using a smaller value is conservative, erring on the side of community safety.

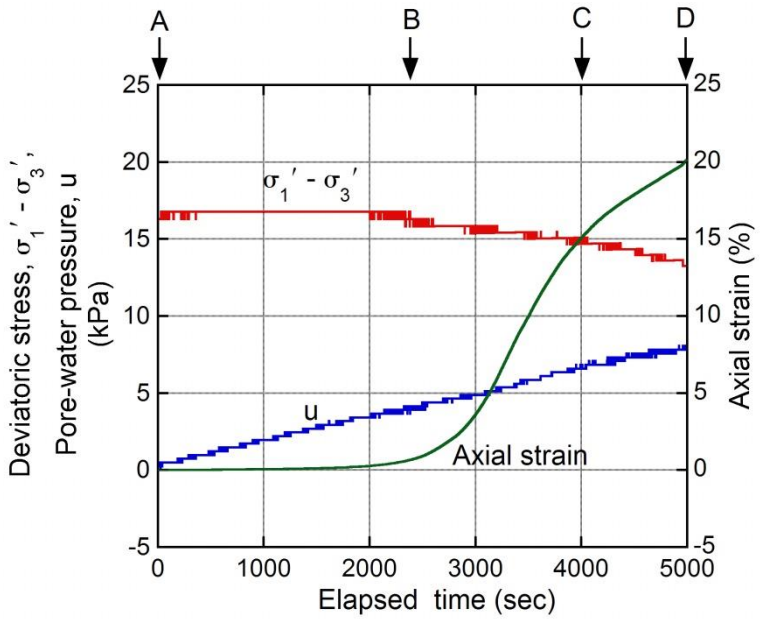

Fig. 6.16 Relationship between deviatoric stress, axial strain and pore-water pressure of the pore-water pressure controlled triaxial test on sample No. 3-DIS

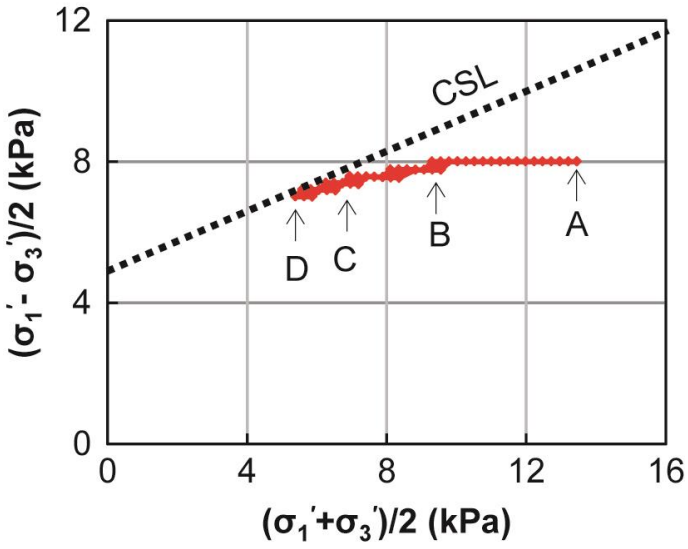

Fig. 6.17 Effective stress paths of pore-water pressure controlled triaxial test. The dotted line is the critical state line (CSL) obtained in undrained tests.

6.5.5 Groundwater simulation

Because the duration of rainfall is short, the hourly rainfall data is too rough for groundwater simulation. For the accurate analysis, the rainfall data per 10 mm as the input data was used for groundwater simulation. The result of groundwater simulation shows that the obvious groundwater generated in the slope after rainfall started for 7.8 hours (Fig. 6.18). After about 9 hours, the groundwater level reached to the maximum level, i.e., the slope was fully saturated. At this time, the pore-water pressure at the bottom of soil layer is 6.7 kPa. The critical value of pore-water pressure is about 6.5 kPa according to the result of stability analysis and pore-water pressure controlled triaxial test. Therefore, it can be obtained that the slope was in critical state when the groundwater level reached to the slope surface.

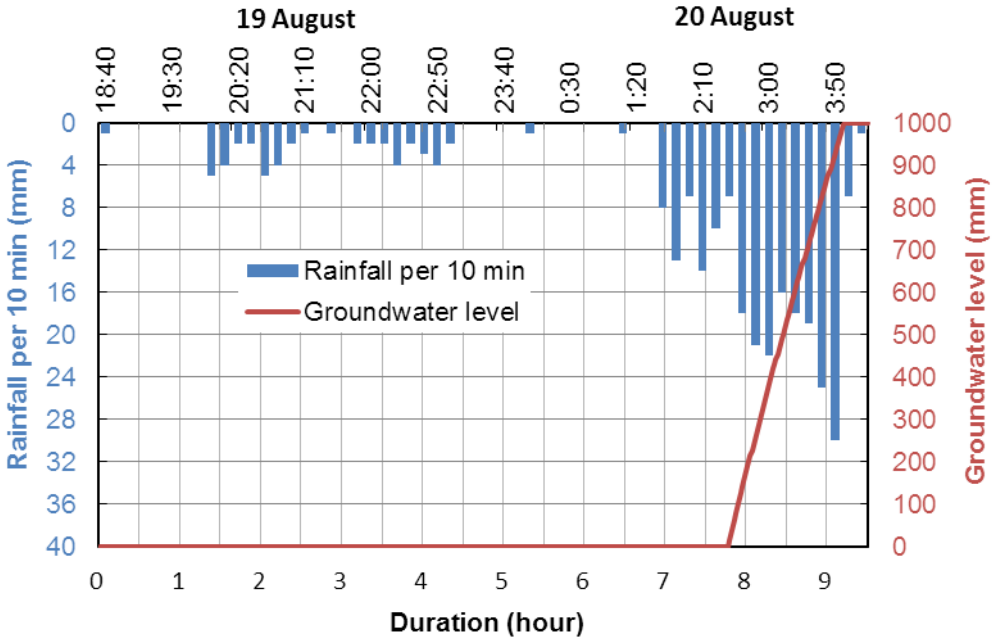

Fig. 6.18 The result of groundwater simulation

6.6 Conclusions

1. Under extreme high intensity and short duration rainstorm, debris flows occurred on very steep slopes with a thin initiating sliding mass in weathered coarse-grained granite and hornfels.
2. Cross sectional properties of the debris flow gully, especially gully shape and changes in width, have important implications for debris flow damming, travel distance, and deposition.
3. During travel, the debris flow may erode the valley and carry the colluvium and valley deposits downslope. Shallow slides in high mountains can cause large-scale debris flow.
4. Debris flows that are rich in fine particles like granitic soil tend to travel long distances until they flow onto very gentle slopes, while those with boulders as components started to deposit as soon as the valley became wide and gently-sloped. The permeability and drainage characteristics of the debris flow controlled the travel distance of the debris flow.

5. Simulation test with pore-water pressure controlled triaxial test shows reasonable response of soil behavior under different water pressure conditions, which corresponds to groundwater level in a real slope. It is hoped that the groundwater level in a real slope can be used for failure prediction.

CHAPTER 7

TIME PREDICTION OF RAINFALL-INDUCED SHALLOW LANDSLIDE DURING HEAVY RAINFALL

7.1 Time prediction of rainfall-induced shallow landslide

A new time prediction of rainfall-induced shallow landslide is developed based on the study on the initiation mechanism of heavy rainfall-induced shallow landslide. The flow chart of this time prediction is shown as Fig. 7.1.

For the target area, field investigation is conducted on the slopes to identify the slope features such as slope angle (α) and thickness of soil layer (H). The laser ranging device and portable dynamic cone penetration tests are convenient and practical tools for field investigation, especially on the steep slope. Undisturbed and disturbed soil samples are collected for laboratory experiments to evaluate the soil properties such as unit weigh (γ), permeability (k), effective friction angle (ϕ') and cohesion (c'). During the field investigation, if it is possible, the in-situ infiltration tests can be conducted on the slope surface to compare with the results obtained by laboratory experiments. Based on the field investigation and laboratory experiments, a database can be built for the target area. The relationship between slope stability and pore-water pressure can be obtained through slope stability analysis according to the slope features and soil properties. The simulation tests also can be used to understand how subsurface-water dynamics influence the landslide initiation. Pore-water pressure controlled triaxial test is

a recommended method for this simulation test. Because the pore-water pressure controlled triaxial test can simulate the field condition to determine the soil behavior response to the increase in pore-water pressure. The critical pore-water pressure (u_c) can be obtained based on the analysis of the effect of pore-water pressure on slope stability. During the heavy rainfall, the realtime data is inputted into the groundwater model to simulate the generation of groundwater level in the soil layer. For the special area, the piezometer can be installed in the soil layer to monitor the pore-water pressure during heavy rainfall. If the pore-water pressure (u), which is obtained by groundwater simulation or field monitoring, is higher than the critical pore-water pressure, the slope will be in critical state and shallow landslide would probably occur.

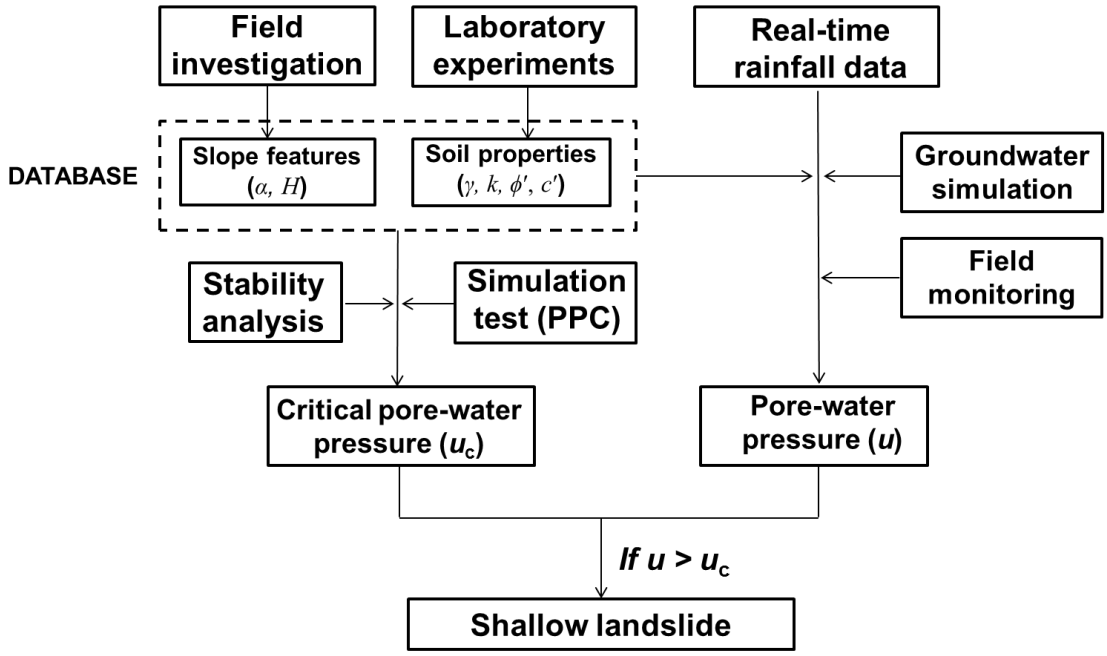

Fig. 7.1 Flow chart for time prediction of rainfall-induced shallow landslide during heavy rainfall

7.2 Method application

The rainfall-induced shallow landslide in northeastern Shikoku, Japan, during typhoon Tokage in 2004 is used to evaluate the feasibility of this method for time prediction of rainfall-induced shallow landslides.

7.2.1 Introduction

Shikoku is located at the south of the island of Honshu and east of the island of Kyushu, between Seto Inland Sea and the Pacific Ocean (Fig. 7.2). The mean annual precipitation of Shikoku ranges from 1,000 to 3,500 mm (Dahal et al., 2009). In 2004, Kagawa Prefecture at the northeastern Shikoku experienced heavy rainfall and faced huge losses of life and property. On 19 and 20 October 2004, typhoon Tokage produced 674 and 495 mm of rainfall in 48-hour on Moriyuki and Monnyu which are located in the eastern part of the Kagawa Prefecture (Fig. 7.2). This heavy rainfall triggered more than 300 landslides in Moriyuki and Monnyu catchment area. In this section, the analysis is based on the investigation works on shallow landsides in Moriyuki, which was conducted by Dahal et al. (2009).

7.2.2 Parameters for analysis

In order to understand the characteristics of slope and soil, Dahal et al., (2009) selected seven shallow landslide sites for detail field and laboratory investigations. Field investigation indicated the slope angle in selected sites ranged from 32 to 44°, the depth of soil layer on each selected slide ranged from 0.7 to 1.1 m, and the horizontal distance of slope ranged from 13.8 to 47.4 m. Most of shallow landslides occurred within masa soil (weathered granite). According the laboratory investigation on the soil samples from shallow landslides, average friction angle values for the study sites ranged from 27.3 to 35.3° and value of cohesion ranged from 2.9 to 6.5 kPa. Based on the investigation results of shallow landslides, the parameters for analysis are shown in Table 7.1.

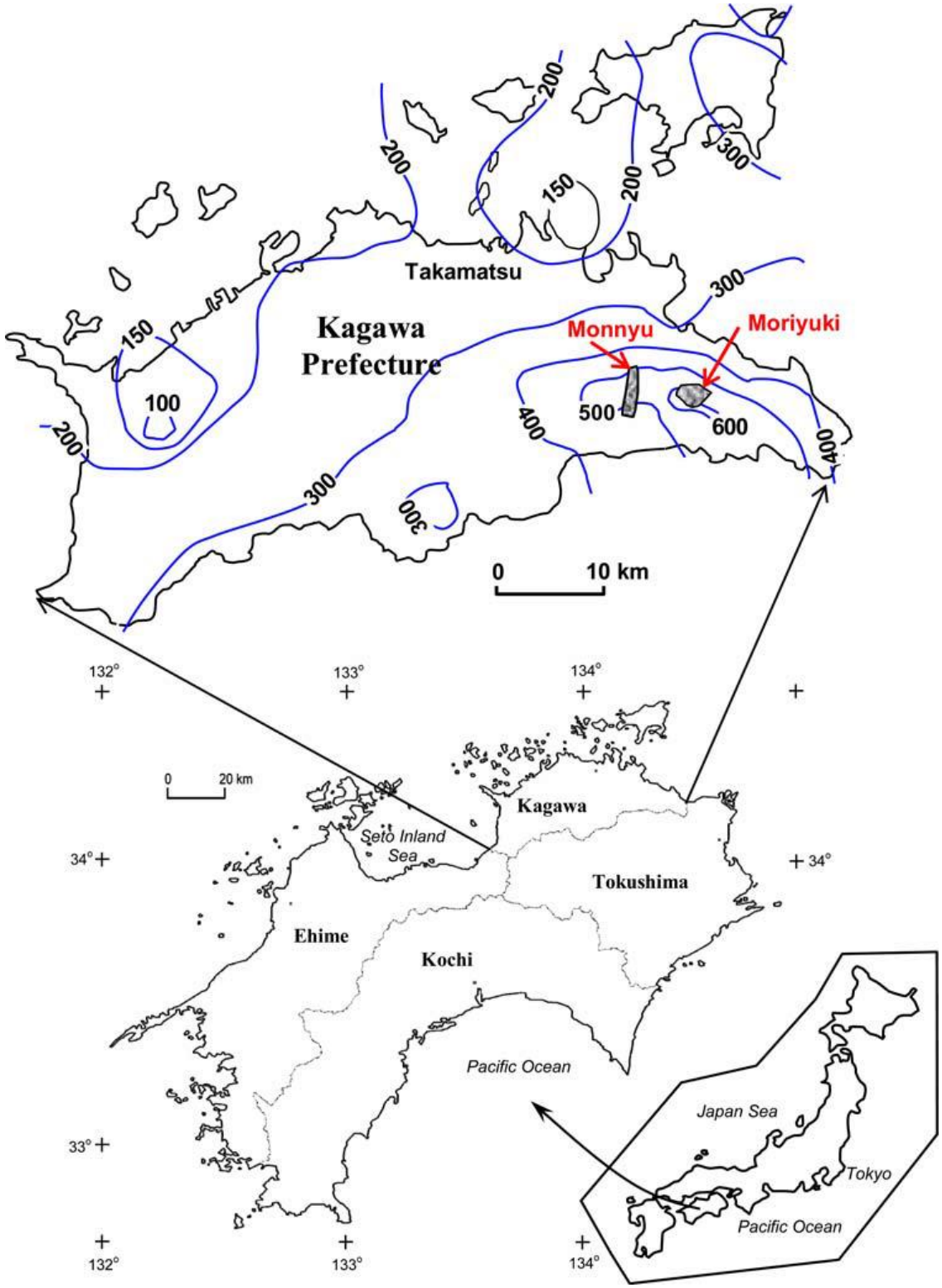

Fig. 7.2 Location of Moriyuki in northeastern Shikoku, Japan and rainfall isohyetal map during typhoon Tokage in 2004 (Dahal et al., 2009)

Table 7.1 Characteristics of slope and soil (referring to Dahal et al., 2009)

Parameters	**Value**
Slope angle, α (°)	34
Vertical depth of soil layer, H (m)	1.0
Horizontal distance of slope, L (m)	35
Porosity, n	0.6
Hydraulic conductivity, k (m/s)	1.10×10^{-5}
Depth-average soil unit weight, γ (kN/m^3)	18.2
Effective friction angle, ϕ' (°)	31.5
Effective cohesion, c' (kPa)	4.9

7.2.3 Critical pore-water pressure and groundwater simulation

The critical pore-water pressure (i.e., when F_S = 1) can be obtained as 6.7 kPa based on the slope stability analysis using Eq. (3.2).

$$F_S = \frac{c' + (\gamma H \cos^2\alpha - u)\tan\phi'}{\gamma H \sin\alpha \cos\alpha} \quad \text{(see 3.2)}$$

$$u = \gamma_w h \cos^2\alpha \quad \text{(see 3.3)}$$

where,

H is the vertical depth of soil layer;

h is the height of groundwater level;

α is the slope angle;

γ is the unit weight of soil;

γ_w is the unit weight of water;

c' is the effective cohesion of soil;

ϕ' is the effective friction angle soil;

u is the pore-water pressure on the potential sliding surface.

The result of groundwater simulation shows that the obvious groundwater generated in the slope after rainfall started for 31 hours (Fig. 7.3). After one hour, the

groundwater level reached to the maximum level (h = 1 m), i.e., the slope was fully saturated. At this time, the pore-water pressure at the bottom of soil layer was 6.7 kPa which is calculated using Eq. (3.3). The critical value of pore-water pressure is 6.7 kPa according to the result of stability analysis. As the description in publication, soil slips occurred in Moriyuki area around the 10:00 a.m. on 20 October 2004 (Dahal et al., 2009).

Through the method application, it can be observed that this method is feasible for time prediction of rainfall-induced shallow landslides during heavy rainfall.

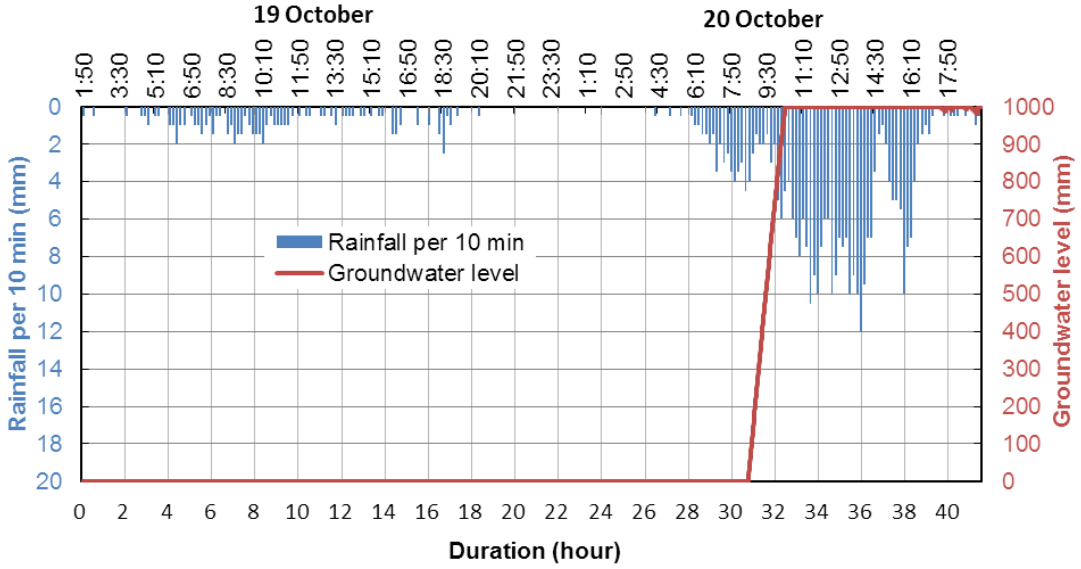

Fig. 7.3 The result of groundwater simulation

CHAPTER 8

CONCLUSIONS

Based on the landslide-forming materials, these three shallow landslides present two kinds of widespread shallow landslides in Japan. One kind of shallow landslides is formed with pyroclastic-fall deposits (shallow landslides in Aso caldera and Izu Oshima Island). The other kind of shallow landslides is formed with residual soil from weathered granite (shallow landslides in Hiroshima). The results of consolidated-undrained triaxial compression tests on these two kinds of soil materials show the different soil behavior. For the pyroclastic-fall deposits, the deviatoric stress increases with the axial strain. The stress-strain curves indicate the evidence of strain hardening. When the shear strain is over about 13%, the deviatoric stress begins to be steady state. The results of triaxial tests show the effective shear strength of pyroclastic-fall deposits are quite high. This explains why the slope can keep stable during normal rainy season. However, for the residual soil from weathered granite, the deviatoric stress reaches the peak value when the axial strain is about 2%. After that, the deviatoric stress turns to decrease with the increase in axial strain.

The pore-water pressure controlled triaxial tests simulate the soil behavior with the increase in pore-water pressure in slope due to rainfall infiltration during heavy rainfall. Meanwhile, the results describe the initiation mechanism of these two kinds of heavy rainfall induced-shallow landslides on the steep slopes with impermeable bedrock. For the pyroclastic-fall deposits, the axial strain starts to increase rapidly when the

pore-water pressure reach to relatively high value. Then, excess pore-water pressure builds up with the rapid increase of axial strain. This will result in the obvious decrease of effective stress of soil. Finally, static liquefaction will occur, leading to the generation of shallow landslides on the steep slopes. For the residual soil from weathered granite, the increase of axial strain starts at low pore-water pressure. With the increase in pore-water pressure, the axial strain increase gradually. Different with the pyroclastic-fall deposits, there is no pore-water pressure buildup. The soil behavior with the increase in pore-water pressure provides the possibility of failure prediction through the monitoring or simulation of groundwater level in slopes during heavy rainfall.

A method for time prediction of rainfall-induced shallow landslides on steep slopes with impermeable bedrock is developed based on the study on the initiation mechanism of heavy rainfall-induced shallow landslide. Based on the field investigations on slopes and laboratory experiments on soil samples, a database can be built for the target area. The relationship between slope stability and pore-water pressure can be obtained through slope stability analysis according to the slope features and soil properties. The simulation tests also can be used to understand how subsurface-water dynamics influence the landslide initiation. Pore-water pressure controlled (PPC) triaxial test is a recommended method for this simulation test. Because the PPC triaxial test can simulate the field condition to determine the soil behavior response to the increase in pore-water pressure, the critical pore-water pressure (u_c) can be obtained based on the analysis the effect of pore-water pressure on slope stability. During heavy rainfall, realtime data is inputted into the groundwater model to simulate the generation of groundwater level in the soil layer. For a special area, piezometers can be installed in the soil layer to monitor the pore-water pressure during heavy rainfall. If the pore-water pressure (u), which is obtained by groundwater simulation or field monitoring, is higher than the critical pore-water pressure (u_c), the slope will be in critical state and shallow landslide could probably occur.

The constructions on the slopes will change the slope feature, adversely affect

slope stability. Slope cutting for road construction on the soft-hard slope structure (porous and shallow soil layer mantling the hard basalt layer) should be considered very carefully. Without any preventive measures, the upper layer soil can easily slide along the interface between the soft and hard layers. The drainage system along the road, especially in areas of low terrain, provides an environment which easily gathered runoff water. An amount of water will continuously infiltrate into the slope below the road, leading to shallow landslides.

Under the extreme high intensity and short duration rainstorm, debris flows may occur on very steep slopes with a thin initiating sliding mass. Cross sectional properties of the debris flow gully, especially the gully shape and width changes, have important implications for debris flow damming, travel distance, and deposition. During travel, the debris flow may erode the valley and carry the colluvium and valley deposits downslope. Shallow slides in high mountains can cause large-scale debris flow. Debris flows that are rich in fine particles tend to travel long distances until they flow onto very gentle slopes, while those with boulders as components started to deposit as soon as the valley became wide and gently-sloped.

REFERENCES

Affendi AA, Faisal A (1994) Field measurement of soil suction. Proceedings, 13th International Conference on Soil Mechanics and Foundation Engineering, New Delhi, India. 1013–1016

Anderson SA and Riemer MF (1995) Collapse of saturated soil due to reduction in confinement. Journal of Geotechnical Engineering 121 (2):216–220

Anderson SA and Sitar N (1995) Analysis of rainfall-induced debris flows. ASCE Journal of Geotechnical Engineering 121 (7):544–552

Aramaki S (1984) Formation of the Aira caldera, southern Kyushu, ~22 000 years ago. Journal of Geophysical Research 89:8485–8501

ASTM D2487-06 (2006) Standard Practice for Classification of Soils for Engineering Purposes (Unified Soil Classification System), ASTM International, West Conshohocken, PA. DOI: 10.1520/D2487-06

Au SWC (1998) Rain-induced slope instability in Hong Kong. Engineering Geology 51: 1–36

Bansal RK (2014) Modelling of groundwater flow over sloping beds in response to constant recharge and stream of varying water level. International Journal of Mathematical Modelling & Computations 4(3):189–200

Bansal RK and Das SK (2010) An analytical study of water table fluctuations in unconfined aquifers due to varying bed slopes and spatial location of the recharge basin. J Hydrol Eng 15(11):909–917

Bishop AW (1959) The principle of effective stress. Teknisk Ukeblad 39:859–863

Bishop AW and Henkel DJ (1962) The Measurement of Soil Properties in the Triaxial Test. Edward Arnold, London, 228 pp

Borga M, Fontana GD, De Ros D, Marchi L (1998) Shallow landslide hazard assessment using a physically based model and digital elevation data. Environ Geol 35:81–88

Brand EW (1981) Some thoughts on rain-induced slope failures. Proceedings of the 1st International Conference on Soil Mechanics and Foundation Engineering, Stockholm, 15–19 June, pp. 373–376

Brenner RP, Tam HK, Brand EW (1985) Field stress path simulation of rain-induced slope failure. Proceedings of the 11th International Conference on Soil Mechanics and Foundation Engineering, pp. 991–996

Calcaterra D, Parise M, Dattola L (1996) Debris flows in deeply weathered granitoids (Serre Massif-Calabria, Southern Italy). In: Senneset, K. (ed.) Proceedings, 7th International Symposium on Landslides. Trondheim, Balkema, pp. 171–176

Capra L, Lugo-Hubp J, Borselli L (2003) Mass movements in tropical volcanic terrains: the case of Teziutlan (Mexico). Engineering Geology 69(3–4):359–379

Casagli N, Dapporto S, Ibsen ML, Tofani V, Vannocci P (2006) Analysis of the landslide triggering mechanism during the storm of 20th–21st November 2000, in Northern Tuscany. Landslides 3(1):13–21

Cevaso A, Pepe G, Brandolini P (2014) The influence of geological and land use settings on shallow landslides triggered by an intense rainfall event in a coastal terraced environment, Bull Eng Geol Environ 73:859–875

Chang M, Chiu Y, Lin S, Ke TC (2005) Preliminary study on the 2003 slope failure in Woo-wan-chai Area, Mt. Ali Road, Taiwan. Engineering Geology 80(1–2):93–114

Chen H, Lee CF, Law KT (2004) Causative mechanisms of rainfall-induced fill slope failures. Journal of Geotechnical and Geoenvironmental Engineering 130(6):593–602

Chen H, Lee CF, Shen JM (2000) Mechanisms of rainfall-induced landslides in Hong Kong. In: G. F. Wieczorek and N.D. Naeser (Editors), Debris-flow Hazards Mitigation : Mechanics, Prediction, and Assessment: Proceedings of the 2nd

International Conference on Debris Flows, Taipei. Rotterdam: Balkema, Taipei, pp. 53–60

Chen SC, Chou HT, Chen SC, Wu CH, Lin BS (2014) Characteristics of rainfall-induced landslides in Miocene formations: A case study of the Shenmu watershed, Central Taiwan, Engineering Geology 169:133–146

Chigira M (2001) Micro-sheeting of granite and its relationship with landsliding specifically after the heavy rainstorm in June 1999. Hiroshima Prefecture, Japan. Engineering Geology 59:219–231

Chigira M and Ito E (1999) Characteristic weathering profiles as basic causes of shallow landslides. In: Yagi N, Yamagam T, Jiang J-C (Eds) Slope stability engineering, vol 2, Balkema, Rotterdam, pp. 1145–1150

Chigira M, Mohamad Z, Sian LC, Komoo I (2011) Landslides in weathered granitic rocks in Japan and Malaysia. Bulletin of the Geological Society of Malaysia 57:1–6

Chipp PN, Henkel DJ, Clare DG, Pope RG (1982) Field measurement of suction in colluvium covered slopes in Hong Kong. Proceedings, 7th Southeast Asian Geotechnical Conference, Hong Kong. 1:49–61

Chu J, Leroueil S, Leong WK (2003) Unstable behaviour of sand and its implication for slope instability. Canadian Geotechnical Journal 40(5): 873–885

Collins BD and Znidarcic D (2004) Stability analyses of rainfall induced landslides. J Geotech Geoenviron Eng 130(4):362–372

Crosta GB and Frattini P (2003) Distributed modeling of shallow landslides triggered by intense rainfall. Nat Hazard Earth Syst Sci 3:81–93

Cruden DM and Varnes DJ (1996) Landslide types and processes. In: Turner AK, Schuster RL (eds) Landslides investigation and mitigation. Transportation research board, US National Research Council. Special Report 247, Washington, DC, Chapter 3, pp. 36–75

Dahal R, Hasegawa S, Nonomura A, Yamanaka M, Masuda T, Nishino K (2009) Failure characteristics of rainfall-induced shallow landslides in granitic terrains of Shikoku Island of Japan. Environmental Geology 56:1295–1310

Dai F and Lee CF (2002) Landslide characteristics and slope instability modeling using GIS, Lantau Island, Hong Kong. Geomorphology 42(3–4):213–228

Dai F, Lee CF, Tham LG, Ng KC, Shum WL (2004) Logistic regression modelling of storm-induced shallow landsliding in time and space on natural terrain of Lantau Island, Hong Kong. Bulletin of Engineering Geology and the Environment 63(4):315–327

Dai F, Lee CF, Wang S (1999a) Analysis of rainstorm-induced slide-debris flows on natural terrain of Lantau Island, Hong Kong. Engineering Geology 51(4):279–290

Dai F, Lee CF, Wang S, Feng Y (1999b) Stree-strain behavior of a loosely compacted volcanic-derived soil and its significance of rainfall-induced fill slope failures. Engineering Geology 53:359–370

Dijkstra TA, Wasowski J, Winter MG, Meng XM (2014) Introduction to geohazards of Central China. Quarterly Journal of Engineering Geology & Hydrogeology 47(3):195–199

Disaster Prevention Division of Tokyo Metropolitan Government (TMG) (2014) Investigation report of Izu Oshima landslide triggered by Typhoon No. 26 in 2013. Sabo 115:7–11 (In Japanese)

Duan W, He B, Takara K, Luo P, Nover D, Yamashiki Y, Huang W (2014) Anomalous atmospheric events leading to Kyushu's flash floods, July 11–14, 2012. Nat Hazards 73:1255–1267

Duncan JM and Wright SG (2005) Soil strength and slope stability. Wiley. pp. 312

Durgin PB (1977) Landslides and the weathering of granitic rocks. Geol Soc Am Rev Eng Geol 3:127–131

Eckis R (1934) South coastal-basin investigation geology and ground-water storage capacity of valley fill. California Department of Public Works, Water Resources Division, Bulletin 45:279

Escario V and Sáez J (1986) The shear strength of partly saturated soils. Géotechnique 36:453–456

Escario V, Juca J, Coppe MS (1989) Strength and deformation of partly saturated soils. In: Proceeding of 12th international conference on soil mechanics and foundation engineering, vol 3. Rio de Janeiro, pp 43–46

Faris F and Wang F (2014) Investigation of the initiation mechanism of an earthquake-induced landslide during rainfall: a case study of the Tandikat landslide, West Sumatra, Indonesia. Geoenvironmental Disasters, 1:4. DOI:10.1186/s40677-014-0004-3

Farooq K, Orense R, Towhata I (2004) Response of unsaturated sandy soilsunder constant shear stress drained condition. Soils and Foundations 44(2):1–13

Fedo CM, Nesbitt HW, Young GM (1995) Unraveling the effects of potassium metasomatism in sedimentary rocks and paleosols, with implications for paleoweathering conditions and provenance. Geology 23:921–924

Fire and Disaster Management Agency, Japan (2012) Report of heavy rainfall from 11 July 2012. (No. 20). http://www.fdma.go.jp/bn/2012/detail/766.html. Accessed 20 January 2015

Fredlund DG, Morgenstern NR, Widger RA (1978) The shear strength of unsaturated soils. Canadian Geotechnical Journal 15:313–321

Gan JKM and Fredlund DG (1996) Shear strength characteristics of two saprolitic soils. Canadian Geotechnical Journal 33:595–609

Gan JKM, Fredlund DG, Rahardjo H (1988) Determination of the shear strength parameters of an unsaturated soil using the direct shear test. Canadian Geotechnical Journal 25:500–510

García-Martínez R and López JL (2005) Debris flows of December 1999 in Venezuela. In: Jakob M, Hungr O (eds) Debris-flow Hazards and Related Phenomena, pp. 519–538

Gasmo JM, Rahardjo H, Leong EC (2000) Infiltration effects on stability of a residual soil slope. Computers and Geotechnics 26:145–165.

Geographical Survey and Photography, Japan (2012) Investigation of debris flows at Mt. Aso caldera triggered by Northern Kyushu heavy rainfall in 2012 using GIS. http://gpi-net.jp/study/aso/aso.html. Accessed 20 January 2015

Giannecchini R, Galanti Y, Avanzi G (2012) Critical rainfall thresholds for triggering shallow landslides in the Serchio River Valley (Tuscany, Italy) Natural Hazards and Earth System Sciences 12:829–842

Guadagno FM, Forte R, Revellino P, Fiorillo F, Focareta M (2005) Some aspects of the initiation of debris avalanches in the Campania Region: the role of morphological slope discontinuities and the development of failure. Geomorphology 66:237–254

Harnois L (1988) The CIW index: A new chemical index of weathering. Sedimentary Geology 55:319–322

Hasegawa S and Saito M (1991) Natural environment, topography and geology of Shikoku, Tsushi-to-Kiso (in Japanese). Jpn Geotech Soc 39–9(404):19–24

Head KH (1998) Manual of soil laboratory testing (Vol. 3). John Wiley & Sons, New York

Hiroshima Prefecture (2014) Monitoring information in Hiroshima Prefecture, http://www.bousai.pref.hiroshima.jp/info/disp?disp=R60100&fmode=1&year=2014&month=8, Accessed 20 Dec 2014 (In Japanese)

Ho DYP and Fredlund DG (1982) Increase in strength due to suction for two Hong Kong soils, Proceedings of the Conference on Engineering and Construction in Tropical and Residual Soils, ASCE, Honolulu, Hawaii, January, pp.11–15

Ho JY, Lee KT, Chang TC, Wang ZY, Liao YH (2012) Influences of spatial distribution of soil thickness on shallow landslide prediction. Engineering Geology 124: 38–46

Hungr O, Leroueil S, Picarelli L (2014) The Varnes classification of landslide types, an update. Landslides 11(2):167–194

Hunter AG (1998) Intracrustal Controls on the coexistence of tholeiitic and calc-alkaline magma series at Aso Volcano, SW Japan. Journal of Petrology 39(7):1255–1284

Ikeya H (2014) Debris flow in Izu Oshima Island on October 16, 2013. Sabo 115:2–6 (In Japanese)

Inagaki H (2014) Investigation report of Izu Oshima landslide caused by Typhoon No. 26 in October 2013. pp. 74–77 (In Japanese)

IPCC (Intergovernmental Panel on Climate Change) (2013) Climate Change 2013: The Physical Science Basis: Contribution of Working Group I to the 5th Assessment Report of the Intergovernmental Panel on Climate Change: Cambridge, UK, Cambridge University Press, 1552 p.

Irfan TV (1994) Mechanism of creep in a volcanic saprolite. Quarterly Journal of Engineering Geology 27:211–230

Irfan TY (1998) Structurally controlled landslides in saprolitic soils in Hong Kong. Geotechnical Geology Engineering 16:215–238

Iverson RM (2000) Landslide triggering by rain infiltration. Water Resources Research. 36(7):1897–1910

Japan Meteorological Agency (2015) The query of past meteorological data. http://www.data.jma.go.jp/obd/stats/etrn/index.php. Accessed 5 Jan 2015 (In Japanese)

Japan Sabo Association (2001) Sabo in Japan—creating safe and rich green communities. Japan Sabo Association, Erosion and Sediment Control Department, River Bureau, Ministry of Land, Infrastructure, Transport and Tourism, Tokyo

Japan Society of Civil Engineering (JSCE) (2013) Investigation report of the disaster caused by Northern Kyushu heavy rainfall in July 2012. http://committees.jsce.or.jp/report/system/files/1-1-6.pdf. Accessed 20 January 2015

Jiao JJ, Wang XS, Nandy S (2005) Confined groundwater zone and slope instability in weathered igneous rocks in Hong Kong. Engineering Geology 80(1-2):71–92

Kamei A, Fukushi K, Takagi T, Tsukamoto H (2012) Chemical overprinting of magmatism by weathering: A practical method for evaluating the degree of chemical weathering of granitoids. Applied Geochemistry 27:796–805

Kasama K, Jiang Y, Hiro-oka A, Yasufuku N, Sato H (2011) Geo-and hydro-mechanical evaluation of slope failure induced by torrential rains in northern-Kyushu area, July 2009. Soils and Foundations 51(4):575–589

Katsube K and Oguchi T (1999) Altitudinal changes in slope angle and profile curvature in the Japan Alps: a hypothesis regarding a characteristic slope angle. Geographical Review of Japan 72(B):63–72

Kawabata D, Oguchi T, Katsube K (2001) Effects on geology on slope angles in the Southern Japanese Alps-a GIS approach. Transactions, Japanese Geomorphological Union 22:827–836

Kawanabe Y (1998) Geological map of Izu Oshima volcano. Geological Map of Volcanoes 10, scale 1:25000. Geological Survey of Japan

Kim J, Jeong S, Park S, Sharma J (2004) Influence of rainfall-induced wetting on the stability of weathered soils slopes. Environmental Geology 75:251–262

Krahn J, Fredlund DG, Klassen MJ (1989) Effect of soil suction on slope stability at Notch Hill. Canadian Geotechnical Journal 26:269–278

Kwong J, Spengler S, Wong N, Wan A (1999) Some important engineering geological and hydrogeological factors influencing slope stability in Hong Kong and Hawaii. In: B. Clarke (Editor), Urban Ground Engineering: Proceedings of the International Conference organized by the Institution of Civil Engineers and held in Hong Kong, China, on 11–12 November 1998. Thomas Telford, London, pp. 235–252.

Lambe WT, Whitman RV (1969) Soil Mechanics. John Wiley, New York

Lan HX, Lee CF, Zhou CH, Martin CD (2005) Dynamic characteristics analysis of shallow landslides in response to rainfall event using GIS. Environmental Geology 47(2):254–267

Lee SJ, Lee SR, Kim YS (2003) An approach to estimate unsaturated shear strength using artificial neural network and hyperbolic formulation. Computers and Geotechnics 30:489–503

Lepore C, Kamal SA, Shanahan P, Bras RL (2012) Rainfall-induced landslide susceptibility zonation of Puerto Rico, Environ Earth Science 66:1667–1681

Lim TT, Rahardjo H, Chang MF, Fredlund DG (1996) Effect of rainfall on matric suctions in a residual soil slope. Canadian Geotechnical Journal 33:618–628

Lourenço SDN, Sassa K, Fukuoka H (2006) Failure process and hydrologic response of a two layer physical model: Implications for rainfall-induced landslides. Geomorphology 73(1–2):115–130

Lu N and Likos W (2013) Origin of Cohesion and Its Dependence on Saturation for Granular Media. Poromechanics V: pp. 1669–1675. DOI: 10.1061/9780784412992.197

Lu N and Likos WJ (2004) Unsaturated soil mechanics. Wiley. pp. 584

Macari EJ, Laymon CA, Costes NC (1992) Hydrologic field instrumentation for a small-scale experiment with implication for rain-induced slope stability analysis. In Proceedings, U.S.-Brazil Geotechnical Workshop: Application of Classical Soil Mechanics Principles to Structured Soils, Belo Horizonte, Brazil. 79–88

Maharaj R (1993) Landslide processes and landslide susceptibility analysis from an upland watershed: a case study from St. Andrew, Jamaica, West Indies. Engineering Geology 34:53–79

Matsueshi Y and Matsukura Y (2006) Cohesion of unsaturated residual soils as a function of volumetric water content. Bull Eng Geol Env (2006) 65: 449–455. DOI 10.1007/s10064-005-0035-9

Matsumoto J (1989) Heavy rainfalls over east Asia. International Journal of Climatology 9:407–423

Matsumoto J (1993) Global distribution of daily maximum precipitation. Bulletin of the Department of Geography, University of Tokyo 25:43–48

Matsumoto J and Takahashi K (1999) Regional differences of daily rainfall characteristics in East Asian summer monsoon season. Geographical Review of Japan 72(B):193–201

Matsushi Y, Saito H, Fukuoka H, Furuya G (2013) Landslides of tephra deposits on hillslope of the Aso caldera wall and volcanic central cones by the North-Kyushu heavy rainfall at July 2012. Annuals of Disaster Prevention Research Institute, Kyoto University (No. 56). http://repository.kulib.kyoto-u.ac.jp/dspace/bitstream/2433/181543/1/a56b0p28.pdf. Accessed 20 January 2015

Miao L, Liu S, Lai Y (2002) Research of soil-water characteristics and shear strength features of Nanyang expansive soil. Engineering Geology 65:261–267

Milledge DG (2008) Modelling shallow landslides: the importance of hydrological controls and lateral reinforcement, Durham theses, Durham University. Available at Durham E-Theses Online: http://etheses.dur.ac.uk/2904/

Ministry of Land Infrastructure and Transport, Japan (2013) Report of the damage caused by heavy rainfall during the typhoon No. 26 (No. 16). http://www.bousai.go.jp/updates/h25typhoon26/pdf/h25typhoon26_16.pdf. Accessed 4 February 2014

Ministry of Land, Infrastructure, Transport and Tourism (2014) Report of countermeasure of slopeland disasters in Hiroshima triggered by heavy rainfall in August, 2014. http://www.mlit.go.jp/river/sabo/H26_hiroshima/141031_hiroshimadosekiryu.pdf. Accessed 5 Jan 2015 (in Japanese)

Miyabuchi Y, Daimaru H, Komatsu Y (2004) Landslides and lahars triggered by the rainstorm of June 29, 2001, at Aso Volcano, Southwestern Japan. Transactions, Japanese Geomorphological Union 25(1):23–43

Miyabuchi Y, Koji T, Ogawa Y, Shimizu T (2007) Runoff and sediment discharge triggered by the Typhnoon 200514 (Nabi) in forested watersheds, Southern Kyushu, Japan. Transactions, Japanese Geomorphological Union 28(2):127–142

Miyabuchi Y, Sugiyama S (2011) 90,000–year phytolith record from tephra section at the northeastern rim of Aso caldera, Japan. Quaternary International 246(1–2):239–246

Miyase M (2012) Investigation report of the debris flow caused by heavy rainfall in July 2012. Sabo 112:7–11

Montgomery DR and Dietrich WE (1994) A physically based model for the topographic control on shallow landsliding. Water Resources Research 30(4):1153–1171

Montgomery DR, Schmidt KM, Dietrich WE, McKean J (2009) Instrumental record of debris flow initiation during natural rainfall: Implications for modeling slope stability. J Geophysics Res-Earth 114, F01031

Morrissey MM, Wieczorek GF, Morgan BA (2001) A comparative analysis of hazard models for predicting debris flows in Madison County, Virginia. US Geological Survey Open file report 1–67

National Research Institute for Earth Science and Disaster Prevention (NIED) (2013) Disaster in the history of Izu Oshima. http://dil.bosai.go.jp/disaster/2013H25T26/pdf/izuoshima_history.pdf. Accessed 22 January 2014

Nesbitt HW and Markovics G (1997) Weathering of granodioritic crust, long-term storage of elements in weathering profiles, and petrogenesis of siliciclastic sediments. Geochimica et Cosmochimica Acta 61:1653–1670

Nesbitt HW and Young GM (1982) Early Proterozoic climates and plate motions inferred from major element chemistry of lutites. Nature 199:715–717

Ng C and Chiu A (2001) Behavior of a loosely compacted unsaturated volcanic soil. Journal of Geotechnical and Geoenvironmental Engineering 127(12):1027–1036

Ng CWW, Wang B, Tung YK (2001) Three-dimensional numerical investigations of groundwater responses in an unsaturated slope subjected to various rainfall patterns. Canadian Geotechnical Journal 38(5):1049–1062

Ng KY (2007) Mechanisms of shallow rainfall-induced landslides in residual soils in humid tropical environments. Ph.D. theses, Durham University.

Ni H, Zheng W, Song Z, Xu W (2014) Catastrophic debris flows triggered by a 4 July 2013 rainfall in Shimian, SW China: formation mechanism, disaster characteristics and the lessons learned, Landslides 11(5):909–921

Nicholson PG, Russell PW, Fujii CF (1996) Soil creep and creep testing of highly weathered tropical soils. In: T.C. Sheahan and V.N. Kaliakin (Editors), Measuring and Modeling Time Dependent Soil Behavior: Proceedings of Sessions. Geo-lnstitute of the American Society of Civil Engineers in conjunction with the ASCE Convention in Washington, D.C., November 10-14, 1996. American Society of Civil Engineers, pp. 195–213

Odong J (2007) Evaluation of empirical formulae for determination of hydraulic conductivity based on grain-size analysis. J Am Sci 3:54–60

Oguchi T, Saito K, Kadomura H, Grossman M (2001) Fluvial geomorphology and paleohydrology in Japan. Geomorphology 39:3–19

Okada Y and Kurokawa U (2015) Examining effects of tree roots on shearing resistance in shallow landslides triggered by heavy rainfall in Shobara in 2010, J For Res 20:230–235

Onda Y (1992) Influence of water storage capacity in the regolith zone on hydrological characteristics, slope processes, and slope form. J Geomorph NF 36:165–178

Oyagi N (1968) Weathering-zone structure and landslides of the area of granitic rocks in Kamo-Daito, Shimane Prefecture. Reports of Cooperative Research for Disaster Prevention, National Research Center for Disaster Prevention (in Japanese with English abstract) 14:113–127

Paudel PP, Moriwaki K, Morita K, Kubota T, Omura H (2003) An assessment of shallow landslides mechanism Induced by rainfall in Hakoishi area. Kyushu Journal of Forest Research 56:122–128

Paudel PP, Omura H, Kubota T, Devkota B (2008) Characterization of terrain surface and mechanisms of shallow landsliding in upper Kurokawa watershed, Mt Aso, western Japan. Bulletin of Engineering Geology and the Environment 67(1):87–95

Paudel PP, Omura H, Kubota T, Inoue T (2007) Spatio-temporal patterns of historical shallow landslides in a volcanic area, Mt. Aso, Japan. Geomorphology 88(1–2):21–33

Petley DN, Higuchi T, Petley DJ, Bulmer MH, Carey J (2005) Development of progressive landslide failure in cohesive materials. Geology, 33(3): 201–204.

Picarelli L, Olivares L, Comegna L, Damiano E (2008) Mechanical aspects of flow-like movements in granular and fine-grained soils. Rock Mech Rock Eng 41(1):179–197

Qureshi MU, Towhata I, Yamada S, Aziz M, Aoyama S (2009) Geotechnical risk assessment of highly weathered slops using seismic refraction technique. In: Oka F, Murakami A, Kimoto S (eds) Prediction and simulation methods for geohazard mitigation. Taylor & Francis Group, London

Robson SG (1993) Techniques for estimating specific yield and specific retention from grain-size data and geophysical logs from clastic bedrock aquifers. In: Water-resources investigation report 93-4198. U.S. Geological Survey, Denver, Colorado, pp. 19

Saito H and Matsuyama H (2012) Catastrophic landslide disasters triggered by record-breaking rainfall in Japan: their accurate detection with normalized soil water index in the Kii peninsula for the year 2011, SOLA 8:81–84

Saito H, Nakayama D, Matsuyama H (2009) Comparison of landslide susceptibility based on a decision-tree model and actual landslide occurrence: the Akaishi Mountains, Japan. Geomorphology 109:108–121

Saito H, Nakayama D, Matsuyama H (2010) Relationship between the initiation of a shallow landslide and rainfall intensity-duration thresholds in Japan. Geomorphology 118:167–175

Sakurai M (2014) The past landslides. In: Investigation report of Izu Oshima landslide caused by Typhoon No. 26 in October 2013. pp. 9–10 (In Japanese)

Sakurai M, Disaster Research Team of Kanto Branch (2014) Landslide disaster of Izu-Oshima Island by typhoon No. 26 in 2013. Journal of the Japan Landslide Society 51(1):25–28 (In Japanese)

Santos OF, Lacerda WA, Ehrlich M (1996) Collapse of saturated soil due to reduction in confinement – Discussion. Journal of Geotechnical Engineering 122(6):505–506

Sassa K, Fukuoka H, Wang F (1998) A rapid landslide-debris flow at Izumi city, Kagoshima, Japan, 1997. Landslide News, 11:2-6

Sassa K, Fukuoka H, Wang F (1997a) Gamahara torrent debris flow on 6 December 1996, Japan -Possible mechanism of the debris flow-. Landslide News, 10:6-9

Sassa K, Fukuoka H, Wang F (1997b) Landslide-triggered stream explosion and debris flow at the Sumikawa Spa, Akita, Northern Japan, May 1997 ----Possible long run-out mechanism of the landslide mass. Landslide News, 11:11-15

Simon A, Larsen MC, Hupp CR (1990) The role of soil processes in determining mechanisms of slope failure and hillslope development in a humid-tropical forest eastern Puerto Rico. Geomorphology 3(3–4):263–286

Skempton AW (1954) The Pore-pressure coefficients A and B. Géotechnique 4(4):143 – 147

Springman SM, Jommi C, Teysseire P (2003) Instabilities on moraine slopes induced by loss of suction: a case study. Geotechnique 53(1):3–10

Sweeney DJ (1982) Some in situ soil suction measurements in Hong Kong's residual soil slopes. Proceedings, 7th Southeast Asian Geotechnical Conference, Hong Kong. 1:91–106

Takahashi Y (2014) The 2014.8.20 sediment disasters in Hiroshima, especially on the geological factors. http://www.geosociety.jp/hazard/content0082.html, Accessed 3 Nov 2014 (In Japanese)

Tang C, van Asch TWJ, Chang M, Chen GQ, Zhao XH, Huang XC (2012) Catastrophic debris flows on 13 August 2010 in the Qingping area, southwestern China: the combined effects of a strong earthquake and subsequent rainstorms, Geomorphology 139–140:559–576

Taylor D W (1948) Fundamentalso f Soil Mechanics, JohnW iley, New York. pp700.

Terlien MTJ (1998) The determination of statistical and deterministic hydrological landslide-triggering thresholds. Environmental Geology, 35(2–3): 124–130.

The Chugoku Shimbun Online (1999) Hazardous area expands while 26 people dead and 9 missing. http://web.archive.org/web/20080316224507/http://www.chugoku-np.co.jp/News/990629_gouu/Tn99070101.html. Accessed 17 Jan 2015 (in Japanese)

The Japan Times (2014) Mudslides kill 36 in Hiroshima. http://www.japantimes.co.jp/news/2014/08/20/national/least-eight-dead-hiroshima-landslides-floods/#.VKpOensXd0Z. Accessed 5 Dec 2014

The Japanese Geotechnical Society (JGS) (2010) Soil test: basic and guidance (The second revision). Maruzen press.

Tokyo District Meteorological Observatory (TDMO) (2013) Quick report about Typhoon No. 26 in 2013. http://www.jma-net.go.jp/tokyo/sub_index/bosai/disaster/ty1326/ty1326_tokyo.pdf. Accessed 4 February 2014

Tsai TL (2008) The influence of rainstorm pattern on shallow landslide. Environmental Geology 53(7):1563–1570

Tsai TL and Wang JK (2011) Examination of influences of rainfall patterns on shallow landslides due to dissipation of matric suction. Environ Earth Sci. 63:65–75

Tsai TL and Yang JC (2006) Modeling of rainfall-triggered shallow landslide. Environmental Geology 50(4):525–534

Tsai TL, Chen HE, Yang JC (2008) Numerical modeling of rainfall-induced shallow landslides in saturated and unsaturated soils. Environmental Geology 55(4):1269–1277

Tsaparas I, Rahardjo H, Toll DG, Leong EC (2002) Controlling parameters for rainfall-induced landslides. Computers and Geotechnics, 29(1):1–27

Tsuchida T, Kano S, Nakagawa S, Kaibori M, Nakai S, Kitayama N (2014) Landslide and mudflow disaster in disposal site of surplus soil at Higashi-Hiroshima due to heavy rainfall in 2009, Soils Found 54(4):621–638

Turner AK and Schuster RL (1996) Landslides: investigation and mitigation. Transportation research board, US National Research Council. Special Report 247, Washington, D. C.

Ueno S (2014) Groundwater. In: Investigation report of Izu Oshima landslide caused by Typhoon No. 26 in October 2013. pp. 19 (In Japanese)

Vanapalli SK and Fredlund DG (2000) Comparison of different procedures to predict unsaturated soil shear strength. Proceedings of the GeoDenver Conference, Denver, Colorado, pp. 195–209

Vanapalli SK, Fredlund DG, Pufahl DE, Clifton AW (1996) Model for the prediction of shear strength with respect to soil suction. Canadian Geotechnical Journal 33:379–392

Varnes DJ (1954) Landslide types and processes. In: Eckel EB (ed) Landslides and engineering practice, special report 28. Highway research board. National Academy of Sciences, Washington, DC, pp. 20–47

Varnes DJ (1978) Slope movement types and processes. In: Schuster RL, Krizek RJ (eds) Landslides, analysis and control, special report 176: Transportation research board,National Academy of Sciences, Washington, DC., pp. 11–33

Wakai A, Uchimura T, Araki K, Inagaki H, Goto S (2014) Geotechnical characters of soil. In: Investigation report of Izu Oshima landslide caused by Typhoon No. 26 in October 2013. pp. 35–39 (In Japanese)

Wang F, Sassa K, Wang G (2002) Mechanism of a long-runout landslide triggered by the August 1998 heavy rainfall in Fukushima Prefecture, Japan. Engineering Geology 63: 169-185

Wang F and Shibata H (2007) Influence of soil permeability on rainfall-induced flowslides in laboratory flume tests. Canadian Geotechnical Journal 44(9):1128–1136

Wang F, Wu YH, Yang H, Tanida Y, Kamei A (2015) Preliminary investigation of the 20 August 2014 debris flows triggered by a severe rainstorm in Hiroshima City, Japan. Geoenvironmental Disasters 2:25. DOI: 10.1186/s40677-015-0025-6

Wang G and Sassa K (2001) Factors affecting rainfall-induced flowslides in laboratory flume tests. Géotechnique 51(7):587 –599

Wang G and Sassa K (2003) Pore-pressure generation and movement of rainfall-induced landslides: effects of grain size and fine-particle content. Engineering Geology 69(1–2):109–125

Wang G, Sassa K, Fukuoka H (2003) Downslope volume enlargement of a debris slide-debris flow in the 1999 Hiroshima, Japan, rainstorm. Engineering Geology 69:309–330

Winter MG, Harrison M, Macgregor, Shackman L (2013) Landslide hazard assessment and ranking on the Scottish road network. Proceedings, Institution of Civil Engineers (Geotechnical Engineering), 166(GE6), 522–539. DOI: 10.1680/geng.12.00063

Wu LZ, Huang RQ, Xu Q, Zhang LM, Li HL (2015) Analysis of physical testing of rainfall-induced soil slope failures. Environmental Earth Sciences. 73(12): 8519–8531

Wu W and Sidle RC (1995) A distributed slope stability model for steep forested basins. Water Resour Res 31:2097–2110

Yamamoto H and Kobayashi H (2014) Characteristics of heavy rainfall and debris flow disaster in Hiroshima City by Akisame-front, 20 August 2014. Journal of Japan

Society for Natural Disaster Science 33(3):293–312 (in Japanese with English Abstract)

Yang H, Wang F, Miyajima M (2015) Investigation of shallow landslides triggered by heavy rainfall during typhoon Wipha (2013), Izu Oshima Island, Japan. Geoenvironmental Disasters 2:15. DOI:10.1186/s40677-015-0023-8

Yu FC, Chen TC, Lin ML, Chen CY, Yu WH (2006) Landslides and rainfall characteristics analysis in Taipei City during the Typhoon Nari event. Natural Hazards 37(1–2):153–167

Zhu JH and Anderson SA (1998) Determination of shear strength of Hawaiian residual soil subjected to rainfall-induced landslides. Geotechnique 48(1):73–82